



저작자표시-비영리-동일조건변경허락 2.0 대한민국

이용자는 아래의 조건을 따르는 경우에 한하여 자유롭게

- 이 저작물을 복제, 배포, 전송, 전시, 공연 및 방송할 수 있습니다.
- 이차적 저작물을 작성할 수 있습니다.

다음과 같은 조건을 따라야 합니다:



저작자표시. 귀하는 원저작자를 표시하여야 합니다.



비영리. 귀하는 이 저작물을 영리 목적으로 이용할 수 없습니다.



동일조건변경허락. 귀하가 이 저작물을 개작, 변형 또는 가공했을 경우에는, 이 저작물과 동일한 이용허락조건하에서만 배포할 수 있습니다.

- 귀하는, 이 저작물의 재이용이나 배포의 경우, 이 저작물에 적용된 이용허락조건을 명확하게 나타내어야 합니다.
- 저작권자로부터 별도의 허가를 받으면 이러한 조건들은 적용되지 않습니다.

저작권법에 따른 이용자의 권리는 위의 내용에 의하여 영향을 받지 않습니다.

이것은 [이용허락규약\(Legal Code\)](#)을 이해하기 쉽게 요약한 것입니다.

[Disclaimer](#)

공학박사 학위논문

Synthesis of Monodispersed and Size-tunable Aluminate Nanospheres by a Forced Hydrolysis Method

강제가수분해법을 이용한 다양한 크기의 단분산된
구형의 알루미네이트 나노분말 합성

2012년 8월

서울대학교 대학원

재료공학부

노 희 석

Synthesis of Monodispersed and Size-tunable Aluminate Nanospheres by a Forced Hydrolysis Method

지도교수 홍 국 선

이 논문을 공학박사 학위논문으로 제출함

2012년 8월

서울대학교 대학원

재료공학부

노 희 석

노희석의 박사 학위논문을 인준함

2012년 6월

| | | |
|-------|-------|-----|
| 위 원 장 | 주 영 창 | (인) |
| 부위원장 | 홍 국 선 | (인) |
| 위 원 | 남 기 태 | (인) |
| 위 원 | 김 동 완 | (인) |
| 위 원 | 정 현 석 | (인) |

Abstract

Synthesis of Monodispersed and Size-tunable Aluminate Nanospheres by a Forced Hydrolysis Method

Hee-Suk Roh

Department of Materials Science & Engineering

College of Engineering

Seoul National University

Phosphors are optical materials applied to the devices such as light-emitting diode (LED), plasma display panel, and cathode ray tube. Recent interests about white LED as a solid state light source stimulate the researches about phosphors as a potential application for white LED. These studies are mainly focused on development of new composition, synthesis of nano-sized phosphor, tailoring of luminescent property, and study on luminescent mechanism. In commercial white LED system combined blue LED and yellow phosphor ($\text{Y}_3\text{Al}_5\text{O}_{12}:\text{Ce}^{3+}$), the overall conversion efficiency of the white LEDs is only 30% due to the backscattering loss of the emission from micrometer-size $\text{Y}_3\text{Al}_5\text{O}_{12}:\text{Ce}^{3+}$ particles. Since the backscattering loss of particle depends on the diameter of particle to the sixth power, it is obvious that using particles

with nanometer-size is an appropriate strategy for suppressing the scattering loss. Therefore, studying about nanometer-size phosphor is emerging as a major issue in luminescent materials for white LEDs. Moreover, phosphors with a perfect spherical shape and narrow size distribution are of great interest, as they enable the optical structure of the phosphor layers to be optimized and offer bright luminescence performance. As a result, synthesis of the monodispersed and spherical nano phosphor is important in luminescent materials for white LEDs.

In this thesis, we synthesized the monodispersed and spherical Al_2O_3 nanoparticles with various compositions by the forced hydrolysis method and subsequent heat-treatment. Then, we synthesized ternary aluminate phosphor, $\text{Y}_3\text{Al}_5\text{O}_{12}:\text{Ce}^{3+}$ and $\text{BaAl}_2\text{O}_4:\text{Eu}^{2+}$, based on the synthesis condition of Al_2O_3 and their structures, morphologies, and luminescent properties were systematically investigated.

First, we demonstrated the formation of monodispersed spherical aluminum hydrous oxide precursors with tunable sizes by controlling the variables of a forced hydrolysis method. The particle sizes of aluminum hydrous oxide precursors were strongly dependent on the molar ratio of the Al^{3+} reactants (sulfates and nitrates). After annealing the amorphous aluminum hydrous oxide in air at 900 and 1100 °C for 1 h, we observed complete conversion to phase-pure γ - and α - Al_2O_3 , respectively, while maintaining monodispersity (125 nm, 195 nm, 320 nm, and 430 nm diameters were observed). Furthermore, both γ - and α - Al_2O_3 were found to be mesoporous in structure, providing enhanced specific surface areas of 102 and 76 m^2/g , respectively, based on the Brunauer-Emmett-Teller (BET) measurement.

Second, monodispersed $\text{Y}_3\text{Al}_5\text{O}_{12}:\text{Ce}^{3+}$ nanospheres were synthesized through forced hydrolysis without a template, followed by thermal calcination processes, and their luminescence properties were examined. Energy dispersive spectroscopy analysis

revealed that the amorphous aluminum oxide layer played an important role in preventing necking between the particles during heat treatment. As a result, stand-alone $\text{Y}_3\text{Al}_5\text{O}_{12}:\text{Ce}^{3+}$ nanospheres with an amorphous aluminum oxide layer shell were synthesized while maintaining monodispersity with an average particle diameter of about 33 nm. These nanospheres had a dense structure and smooth surface with relatively good crystallinity after annealing at 1075 °C. They absorbed light efficiently in the visible region of 400-500 nm, and showed a single broadband emission peak at 536 nm with a luminescence quantum efficiency (QE) of 33% and relatively good photostability.

Third, monodispersed $\text{BaAl}_2\text{O}_4:\text{Eu}^{2+}$ nanospheres were synthesized through forced hydrolysis using $\gamma\text{-Al}_2\text{O}_3$ nanospheres as a template and subsequent heat-treatment. The amount of Ba^{2+} ion coated on the $\gamma\text{-Al}_2\text{O}_3$ template was increased as the reaction time was increased. The sample reacted for 3 h transformed into BaAl_2O_4 after annealing at 900 °C while maintaining monodispersity and morphology. The average size of the synthesized $\text{BaAl}_2\text{O}_4:\text{Eu}^{2+}$ was controlled by changing the size of $\gamma\text{-Al}_2\text{O}_3$ template. As a result, monodispersed $\text{BaAl}_2\text{O}_4:\text{Eu}^{2+}$ nanospheres with the average diameter of 180 nm were synthesized successfully. In addition, the excitation and emission spectra of the synthesized $\text{BaAl}_2\text{O}_4:\text{Eu}^{2+}$ were similar to those of bulk $\text{BaAl}_2\text{O}_4:\text{Eu}^{2+}$, the maximum wavelengths of the excitation and emission were approximately 345 nm and 495 nm, respectively.

This thesis focused on the synthesis of monodispersed and size-tunable secondary and ternary aluminate nanospheres. In addition, we tried to propose a possible synthesis method for synthesis of stand-alone aluminate nanospheres with high luminescence efficiency through the systematic analysis using X-ray powder diffraction (XRD), field-emission scanning electron microscopy (FESEM),

transmission electron microscopy (TEM), and so on.

**Keywords: monodispersed, size-tunable, nanosphere, aluminate, forced hydrolysis,
phosphor**

Student Number: 2006-23046

Table of Contents

| | |
|---|-------------|
| Abstract | i |
| Table of Contents | v |
| List of Tables | viii |
| List of Figures | ix |
| | |
| Chapter 1 Introduction | 1 |
| 1.1 Current issues | 1 |
| 1.1.1 Phosphors for white LEDs..... | 1 |
| 1.1.2 Synthesis of nano-sized phosphor..... | 4 |
| 1.2 Aim and objective | 6 |
| | |
| Chapter 2 Theoretical background..... | 8 |
| 2.1 Application of phosphors for white light-emitting diodes | 8 |
| 2.1.1 Light-emitting diode | 8 |
| 2.1.2 White light using LEDs (white LEDs)..... | 10 |
| 2.1.3 Advantages of spherical and nano-sized phosphors for white LEDs | 15 |
| 2.2 Luminescence | 20 |
| 2.2.1 Definition of phosphor..... | 20 |
| 2.2.2 Various type of luminescence | 21 |
| 2.2.3 Material compositions of phosphor | 24 |

| | | |
|-------|---|----|
| 2.2.4 | Configuration coordinate model | 25 |
| 2.2.5 | Crystal field theory | 27 |
| 2.2.6 | Decay of luminescence | 29 |
| 2.3 | Synthesis of monodispersed and nano-sized particles as building blocks..... | 38 |
| 2.3.1 | Mechanism of formation..... | 38 |
| 2.4 | Materials..... | 43 |
| 2.4.1 | Al_2O_3 | 43 |
| 2.4.2 | $\text{Y}_3\text{Al}_5\text{O}_{12}:\text{Ce}^{3+}$ | 44 |
| 2.4.3 | $\text{BaAl}_2\text{O}_4:\text{Eu}^{2+}$ | 45 |

Chapter 3 Experimental procedure 52

| | | |
|-------|--|----|
| 3.1 | Synthesis..... | 52 |
| 3.1.1 | Size-controlled synthesis of monodispersed mesoporous α -alumina spheres | 52 |
| 3.1.2 | Synthesis of monodispersed $\text{Y}_3\text{Al}_5\text{O}_{12}:\text{Ce}^{3+}$ nanosphere phosphor... 53 | |
| 3.1.3 | Synthesis of monodispersed and size-tunable $\text{BaAl}_2\text{O}_4:\text{Eu}^{2+}$ nanosphere phosphor using $\gamma\text{-Al}_2\text{O}_3$ nanosphere as a template | 54 |
| 3.2 | Characterization..... | 55 |

Chapter 4 Synthesis of monodispersed and size-tunable aluminate by a forced hydrolysis 57

| | | |
|-----|---|--|
| 4.1 | Size-controlled synthesis of monodispersed mesoporous α -alumina | |
|-----|---|--|

| | |
|--|------------|
| spheres | 57 |
| 4.2 Synthesis of monodispersed $\text{Y}_3\text{Al}_5\text{O}_{12}:\text{Ce}^{3+}$ nanosphere phosphor... | 80 |
| 4.3 Synthesis of monodispersed and size-tunable $\text{BaAl}_2\text{O}_4:\text{Eu}^{2+}$ nanosphere phosphor using $\gamma\text{-Al}_2\text{O}_3$ nanosphere as a template..... | 101 |
| Chapter 5 Summary and Conclusion | 113 |
| References..... | 115 |
| Abstract (Korean)..... | 125 |

List of Tables

| | | |
|--------------------|---|----|
| Table 2.1.1 | Packing density of mixed spheres of different size | 19 |
| Table 2.2.1 | Luminescence type, applications and typical efficiencies | 30 |
| Table 2.2.2 | The electronic transitions and examples of impurities ions (activator) .. | 31 |
| Table 4.1.1 | R of reactant solution | 66 |
| Table 4.1.2 | The concentration of counter anion of additional reactant solution | 67 |
| Table 4.2.1 | The result of point- and area-mode EDS analysis of R46-1075 and R50-975 | 87 |
| Table 4.2.2 | The result of ICP-MS analysis of R46-1075 and R50-975 | 88 |
| Table 4.2.3 | QE of the Commercial/R46-1075 YAG excited at 450 nm | 89 |

List of Figures

| | | |
|---------------------|---|----|
| Figure 2.1.1 | The device structure of blue LED and YAG:Ce phosphor combined white LED system..... | 13 |
| Figure 2.1.2 | Emission spectrum of blue LED and YAG:Ce phosphor combined white LED..... | 14 |
| Figure 2.2.1 | Schematic descriptions about the difference between fluorescence and phosphorescence (A = Absorption, F = Fluorescence, P = Phosphorescence, S = Singlet state ($\uparrow\downarrow$), T = Triplet state ($\uparrow\uparrow$))..... | 32 |
| Figure 2.2.2 | Luminescent material containing activator (A) and sensitizer (S)..... | 33 |
| Figure 2.2.3 | Configuration coordinate model with discrete harmonic oscillator energy levels for a localized center..... | 34 |
| Figure 2.2.4 | Simplified configuration coordinate diagram for a two-level system.. | 35 |
| Figure 2.2.5 | Stokes shift in absorption and emission spectra for a two-level system.. | 36 |
| Figure 2.2.6 | Schematic depiction of energy level splitting of the $4f^65d^1$ level in Eu^{2+} by the crystal field..... | 37 |
| Figure 2.3.1 | Stages in the precipitation of colloid particles in homogeneous solutions..... | 42 |
| Figure 2.4.1 | Unit cell structure of $\alpha\text{-Al}_2\text{O}_3$ | 47 |
| Figure 2.4.2 | Schematic diagram of the energy level and band structure of YAG:Ce single crystal | 48 |
| Figure 2.4.3 | Room-temperature excitation and emission spectra of YAG:Ce | 49 |
| Figure 2.4.4 | Emission (a: λ_{exc} 340 nm, c: λ_{exc} 280 nm, d: λ_{exc} 400 nm) and excitation (b: λ_{em} 498 nm) spectra of $\text{BaAl}_2\text{O}_4\text{:Eu}^{2+}$ phosphors | 50 |

| | | |
|---------------------|--|----|
| Figure 2.4.5 | Gaussian fit of the emission spectrum of $\text{BaAl}_2\text{O}_4:\text{Eu}^{2+}$ excited at 340 nm at room temperature into two components. Black line is the experimental results and red line is the fitting results..... | 51 |
| Figure 4.1.1 | FESEM images of the aluminum hydrous oxide precursors prepared with different values of R : (a) 0.33, (b) 0.27, (c) 0.215, and (d) 0.167... .. | 68 |
| Figure 4.1.2 | Magnified FESEM image of the as-prepared aluminum hydrous oxide precursor (R=0.75)..... | 69 |
| Figure 4.1.3 | FESEM images of the aluminum hydrous oxide precursors prepared at 90 °C for 1 h : (a) R = 0.33, (b) R = 0.27, (c) R = 0.215, (d) R = 0.167, (e) R_{Cl} = 0.33, (f) R_{Cl} = 0.27, (g) R_{Cl} = 0.215 and (h) R_{Cl} = 0.167 | 70 |
| Figure 4.1.4 | The average size of the synthesized aluminum hydrous oxide precursors prepared by the different value of R and R_{Cl} | 71 |
| Figure 4.1.5 | FESEM images of the aluminum hydrous oxide precursors prepared at 90 °C for 1 h with different concentration of $[\text{SO}_4^{2-}]$: (a) 0.015 M, (b) 0.0135 M, (c) 0.012 M, (d) 0.0105 M, (e) 0.009 M, (f) 0.0075 M, (g) 0.006 M, (h) 0.00525 M, (i) 0.0045 M, (j) 0.00375 M, and (k) 0.0015 M..... | 72 |
| Figure 4.1.6 | The relation between the morphology and size distribution of the synthesized particles and the concentration of sulfate ions | 73 |
| Figure 4.1.7 | TG/DTA curves of sample a (R=0.33)..... | 74 |
| Figure 4.1.8 | XRD patterns of sample a (R=0.33) annealed at different temperatures for 12 h : (a) as-prepared, (b) 900 °C, (c) 950 °C, (d) 1000 °C, (e) 1050 °C, and (f) 1100 °C..... | 75 |
| Figure 4.1.9 | XRD patterns of the samples prepared with different values of R and | |

| | | |
|----------------------|--|----|
| | subsequently annealed at 1100 °C for 1 h : (a) 0.33, (b) 0.27, (c) 0.215, and (d) 0.167 | 76 |
| Figure 4.1.10 | FESEM images of the samples prepared with different values of R and subsequently annealed at 1100 °C for 1 h : (a) 0.33, (b) 0.27, (c) 0.215, and (d) 0.167 | 77 |
| Figure 4.1.11 | TEM images of sample a (R=0.33) annealed in air at 1100 °C for 1 h. (a) bright-field image, (b) high-resolution image, and (c) the SAED pattern | 78 |
| Figure 4.1.12 | Nitrogen adsorption–desorption isotherms along with the corresponding pore size distributions (inset) of sample a (R=0.33) before and after heat treatment in air | 79 |
| Figure 4.2.1 | SEM images of the precursors prepared with different reaction times: (a) R44, (b) R46, (c) R48, (d) R50 and (e) R52 | 90 |
| Figure 4.2.2 | Phase evolutions of samples after subsequent heat-treatment : (a) R44, (b) R46, (c) R48, (d) R50 and (e) R52 | 91 |
| Figure 4.2.3 | XRD patterns of the samples prepared with different reaction times and subsequently annealed at different temperatures for 6 h: (a) R44-1125, (b) R46-1075, (c) R48-1025, (d) R50-975 and (e) R52-975 | 92 |
| Figure 4.2.4 | SEM images of the samples prepared with different reaction times and subsequently annealed at different temperatures for 6 h: (a) R44-1125, (b) R46-1075, (c) size distribution of R46-1075, (d) R48-1025, (e) R50-975 and (f) R52-975 | 93 |
| Figure 4.2.5 | XRD patterns of the samples prepared with different reaction times and subsequently annealed at 1300 °C for 6 h: (a) R44-1300, (b) R46-1300, (c) R48-1300, (d) R50-1300 and (e) R52-1300 | 94 |

| | | |
|----------------------|--|-----|
| Figure 4.2.6 | TEM images of the samples prepared with different reaction times and subsequently annealed at different temperatures for 6 h: (a) bright field image of R46-1075, (b) high-resolution image of R46-1075, (c) bright field image of R50-975 and (d) high-resolution image of R50-975. The insets of the high-resolution images show the Fast Fourier Transform (FFT) results | 95 |
| Figure 4.2.7 | EDS line profiles of (a) R46-1075 and (b) R50-975..... | 96 |
| Figure 4.2.8 | EDS analysis carried out on the samples by point- and area-mode: (a) points in R46-1075, (b) area in R46-1075, (c) points in R50-975 and (b) area in R50-975..... | 97 |
| Figure 4.2.9 | Elemental mapping by EDS analysis of R46-1075 (Red : Yttrium , Green : Aluminum) | 98 |
| Figure 4.2.10 | PL excitation and emission spectra of (a) R46-1075 and (b) R50-975 | 99 |
| Figure 4.2.11 | Photostability of R46-1075 under blue excitation at 455 nm. The inset showed the photostability of the commercial YAG:Ce..... | 100 |
| Figure 4.3.1 | SEM images of the γ 0.215 template and the samples prepared with different reaction times: (a) γ 0.215 template, (b) γ 0.215-1h, (c) γ 0.215-2h and (d) γ 0.215-3h | 105 |
| Figure 4.3.2 | XRD patterns of the samples prepared with different reaction times using γ 0.215 template and subsequently annealed at 1300 °C for 5 h: (a) γ 0.215-1h-1300:5h, (b) γ 0.215-2h-1300:5h and (c) γ 0.215-3h-1300:5h (* : α -Al ₂ O ₃ (JCPDS No. 46-1212), + : EuAlO ₃ (JCPDS No. 30-0012) and # : Ba _{0.79} Al _{10.9} O _{17.14} (JCPDS No. 77-1522))..... | 106 |
| Figure 4.3.3 | XRD patterns of the samples reacted for 2 h using γ 0.215 template and subsequently annealed at various temperature for 5 h: (a) γ 0.215-2h- | |

| | | |
|---------------------|--|-----|
| | 600:5h, (b) γ 0.215-2h-700:5h, (c) γ 0.215-2h-800:5h and (d) γ 0.215-2h-900:5h (^ : BaCO ₃ (JCPDS No. 45-1471)) | 107 |
| Figure 4.3.4 | SEM images of the samples prepared using γ -Al ₂ O ₃ templates with different concentration ratio of Al ₂ (SO ₄) ₃ •16H ₂ O to Al(NO ₃) ₃ •9H ₂ O : (a) γ 0.33 template, (b) γ 0.33-2h, (c) γ 0.215 template, (d) γ 0.215-2h, (e) γ 0.125 template and (f) γ 0.125-2h | 108 |
| Figure 4.3.5 | XRD patterns of the samples prepared using γ -Al ₂ O ₃ templates with different concentration ratio of Al ₂ (SO ₄) ₃ •16H ₂ O to Al(NO ₃) ₃ •9H ₂ O and subsequently annealed at 1300 °C for 5 h: (a) γ 0.33-2h-1300:5h, (b) γ 0.215-2h-1300:5h and (c) γ 0.125-2h-1300:5h (* : α -Al ₂ O ₃ (JCPDS No. 46-1212), + : EuAlO ₃ (JCPDS No. 30-0012) and # : Ba _{0.79} Al _{10.9} O _{17.14} (JCPDS No. 77-1522))..... | 109 |
| Figure 4.3.6 | SEM image of γ 0.215-3h-900:4h..... | 110 |
| Figure 4.3.7 | XRD pattern of γ 0.215-3h-900:4h | 111 |
| Figure 4.3.8 | PL spectra of the γ 0.215-3h-900:4h | 112 |

Chapter 1 Introduction

1.1 Current issues

1.1.1 Phosphors for white LEDs

Since the first development of ZnS-type phosphor, an important class of phosphors for television tube, in 1866, phosphors have been currently used in many displays and lighting devices.^{1,1} Among various application areas of phosphor, light-emitting diodes (LEDs) is particularly interest areas because of their high efficiency and environment-friendly characteristics.

Recently LEDs, particularly white LEDs, have attracted much attention as new and economically advantageous all solid state light sources. The development of LEDs has also stimulated research on phosphors used for white LEDs. In 1991, Nichia Corporation pioneered the development of blue LEDs based on InGaN. And, It was 1996 when a white LED composed of blue LED and yellow emitting $\text{Y}_3\text{Al}_5\text{O}_{12}:\text{Ce}^{3+}$ (YAG:Ce) was first commercialized. The combination of blue and yellow light gives the sensation of white color by the principle of complimentary colors.^{1,2} Since their introduction, this type of white LEDs, known as the blue-YAG white, has captured a substantial market because of their attractive properties such as compactness, light weight, and quick response.^{1,3} These advantages fit quite well to the rapidly growing demand for backlighting small-sized liquid crystal displays. In the past few years, high-power UV LEDs have been developed by a number of companies and institutions.^{1,4-1,7} This has stimulated the research and development of phosphors, which can be excited

by UV LEDs, emitting the three primary colors.^{1.8-1.11} White LEDs as well as devices emitting intermediate colors can be obtained with the proper admixture of these tricolor phosphors. The white LEDs based on UV LEDs are superior to blue-YAG white in some respects. Their high color rendering performance, uniformity in the emitted white color and wider chromaticity of backlight are some of the apparent advantages. However, such devices have not been marketed on a large scale, because of lifetime and efficiency considerations.^{1.12-1.14}

In blue-YAG white system, the overall conversion efficiency of the white LEDs is only 30% due to the backscattering loss of the emission from YAG:Ce particles.^{1.15} Multiple scattering of the emission from the micrometer-sized YAG:Ce particles leads to poor beam collimation, substantial backscattering of the emission into the semiconductor chip, and absorption losses in the phosphor itself. Since the scattering efficiency of particle depends on the diameter of particle to the sixth power,^{1.16} it is obvious that using particles with nanometer-size is an appropriate strategy for suppressing the scattering loss.^{1.17} In addition, particles of which diameter are smaller than 50 nm can be transparently dispersed in a matrix, showing the negligible scattering of visible light.^{1.18} Therefore, reducing the particle size to the nanometer scale would essentially eliminate the backscattering loss in the white LEDs. In the white LEDs based on UV LEDs with tricolor phosphor system, more kinds of phosphors are used than blue-YAG white system. Therefore, reducing the particle size to reduce the backscattering loss is more important in the white LEDs based on UV LEDs with tricolor phosphor system.

Moreover, the morphology of phosphor particle is one of the key parameters affecting the application of the phosphors. Phosphors with a perfect spherical shape and narrow size distribution are of great interest, as they enable the optical structure of

the phosphor layers to be optimized and offer bright luminescence performance.^{1,19} The ideal morphology can also allow dense phosphor layers to be formed through the close packing of the phosphor powders in order to prevent them from aging.^{1,20, 1.21}

Therefore, synthesis of the monodispersed and spherical nano phosphor is important in the white LEDs.

1.1.2 Synthesis of nano-sized phosphor

Nano-scale materials can exhibit new or enhanced structured, electronic, magnetic, and optical properties.^{1.22-1.24} These size-dependent properties coupled with the significant improvement in the spatial resolution of characterization and imaging methods during the last 20 years or so, have stimulated the development and study of nano-materials. Researchers are active worldwide developing new preparation methods for nano-particles and nano-structures to study their unique size-dependent properties and to apply them in functionally and technologically useful materials. A number of recent papers, patents, and general interest books provide a survey of the wide range of current research in nano-technology.^{1.25} Several recent reviews also provide more focused overviews of the size-dependent optical properties of metals, semiconductors, and insulators.^{1.26-1.29} This discussion specifically introduces and reviews the preparation, characterization, advantages, and disadvantages of using nano-structured materials in phosphor applications. Forming a luminescent phosphor particle at the nano-scale can change the structure, crystallinity, and intrinsic optical properties of the host, thereby affecting the characteristics and efficiencies of a phosphor material.^{1.30}

Among various phosphor host materials, aluminate phosphors have been extensively investigated, because of their high chemical stability and bright emission characteristics in the visible light region.^{1.31-1.33} Especially, rare-earth-doped aluminates serve as an important class of phosphors for fluorescent lamps, plasma display applications and phosphorescence. However, synthesis of the monodispersed spherical aluminate nanophosphors is very difficult due to the high calcination temperature of aluminate phosphors. The size and morphology of the phosphor particles are not homogeneous or it is hard to obtain a stand-alone particle due to necking or

agglomeration between particles occurring during the calcination process.

To solve these problems and synthesize the monodispersed spherical aluminate nanophosphors, we use a forced hydrolysis method. It was shown earlier that monodispersed spherical aluminum hydroxide particles can be prepared by the hydrolysis of aluminum salts containing sulfate ions in the absence and presence of urea.^{1.34-1.36} This method, which is based on the hydrolysis reaction, has the following advantages. First, it is suitable for synthesizing monodispersed particles, because the homogeneity of the solution is maintained throughout the reaction process. There have been many studies on the synthesis of monodispersed ceramic particles with various compositions by the forced hydrolysis method.^{1.37-1.41} Secondly, Y.-S. Her *et al.* proposed a continuous precipitation process using the forced hydrolysis method,^{1.36} therefore this method has several advantages for mass production.

1.2 Aim and objective

In this study, we synthesized the monodispersed and spherical Al_2O_3 nanoparticles with various compositions by the forced hydrolysis method and subsequent heat-treatment. Then, we synthesized ternary aluminate phosphor, YAG:Ce and $\text{BaAl}_2\text{O}_4:\text{Eu}^{2+}$, based on the synthesis condition of Al_2O_3 . There were two approaches that synthesized ternary aluminate phosphor :

- i) We synthesized monodispersed and size-tunable ternary aluminate nanophosphors by forced hydrolysis without template.
- ii) We used monodispersed and size-tunable $\gamma\text{-Al}_2\text{O}_3$ nanospheres as a template if one or more source was insoluble in water.

We synthesized various controlled sizes of monodispersed spherical aluminum hydrous oxide nanoparticles by changing the ratio of sulfate and nitrate ions by using the forced hydrolysis method at a low-temperature, $\sim 100^\circ\text{C}$ and transform aluminum hydrous oxide precursor to porous $\alpha\text{-Al}_2\text{O}_3$ nano particles by heat treatment. Various sizes of monodispersed spherical aluminum hydrous oxide nanoprecursors were synthesized by controlling the variables of the forced hydrolysis method. Phase-pure porous $\alpha\text{-Al}_2\text{O}_3$ nanospheres were also formed through a subsequent heat-treatment at 1100°C .

Based on the above condition that synthesizes monodispersed spherical aluminum hydrous oxide nanoparticles, we synthesized monodispersed spherical YAG:Ce nanoprecursors with various reaction times. The YAG:Ce nanoprecursor prepared with a reaction time of 46 min was transformed to phase pure and stand-alone YAG:Ce nanospheres through subsequent heat treatment at 1075°C and its luminescence characteristics were investigated, including excitation and emission spectra, quantum

efficiency and photostability.

Finally, we synthesized monodispersed $\text{BaAl}_2\text{O}_4:\text{Eu}^{2+}$ nanospheres by a forced hydrolysis using $\gamma\text{-Al}_2\text{O}_3$ as a template. The amount of Ba^{2+} ion coated on the surface of $\gamma\text{-Al}_2\text{O}_3$ template was increased as the reaction time was increased. As a result, the sample reacted for 3 h was transformed into BaAl_2O_4 by subsequent heat-treatment at 900 °C. Size-tunable $\text{BaAl}_2\text{O}_4:\text{Eu}^{2+}$ nanospheres were synthesized by changing the size of $\gamma\text{-Al}_2\text{O}_3$ template and their luminescence characteristics were investigated.

Chapter 2 Theoretical background

2.1 Application of phosphors for white light-emitting diodes

2.1.1 Light-emitting diode

A light-emitting diode (LED) is a semiconductor light source. Introduced as a practical electronic component in 1962, early LEDs emitted low-intensity red light, but modern versions are available across the visible, ultraviolet and infrared wavelengths, with very high brightness.^{2,1} In the late 1980s, key breakthroughs in GaN epitaxial growth and p-type doping ushered in the modern era of GaN-based optoelectronic devices. Building upon this foundation, in 1993 high brightness blue LEDs were demonstrated. Blue LEDs are based on the wide band gap semiconductors GaN^{2,2,2,3} (gallium nitride) and InGaN^{2,4-2,7} (indium gallium nitride). AlGaIn aluminum gallium nitride of varying AlN fraction can be used to manufacture the cladding and quantum well layers for ultraviolet LEDs, but these devices have not yet reached the level of efficiency and technological maturity of the InGaIn-GaN blue/green devices. With nitrides containing aluminum, most often AlGaIn and AlGaInN, even shorter wavelengths are achievable. Ultraviolet LEDs in a range of wavelengths are becoming available on the market. Near-UV emitters at wavelengths around 375–395 nm are already cheap and often encountered, for example, as black light lamp replacements for inspection of anti-counterfeiting UV watermarks in some documents and paper currencies. Shorter wavelength diodes, while substantially more expensive, are commercially available for wavelengths down to 247 nm. Recent research has shown that commercially available

UV LED (365 nm) is already effective disinfection and sterilization devices. Deep-UV wavelengths were obtained in laboratories using aluminum nitride (210 nm), boron nitride (215 nm) and diamond (235 nm).^{2,8,2,9}

LEDs are used as indicator lamps in many devices, and are increasingly used for lighting. LEDs present many advantages over incandescent light sources including lower energy consumption, longer lifetime, improved robustness, smaller size, faster switching, and greater durability and reliability. However, they are relatively expensive and require more precise current and heat management than traditional light sources. Current LED products for general lighting are more expensive to buy than fluorescent lamp sources of comparable output.^{2,10-2,12}

2.1.2 White light using LEDs (white LEDs)

Structure and features of white LEDs

Presently three kinds of white LEDs have been proposed and constructed, as follows :

- i) Phosphor-based white LEDs excited by blue-emitting LEDs: a yellow phosphor or two phosphors (red and green) are mounted on a blue LED.
 - ii) Phosphor-based white LEDs excited by UV or NUV-emitting LEDs : A combination of two or more phosphors, spanning the blue to red spectrum, is applied to a UV or violet LED (365 – 420 nm).
 - iii) Three LEDs of the primary colors are combined with each other.
- From among these, i) and ii) use phosphors.

Phosphor-based white LEDs

This method involves coating an blue-emitting LED with phosphor of different colors to produce white light, the resultant LEDs are called phosphor-based white LEDs. If several phosphor layers of distinct colors are applied, the emitted spectrum is broadened, effectively increasing the color rendering index (CRI) value of a given LED. Phosphor based LEDs have a lower efficiency than normal LEDs due to the heat loss from the Stokes shift and also other phosphor related degradation issues. However, the phosphor method is still the most popular technique for manufacturing high intensity white LEDs and the majority of high intensity white LEDs presently on the market are manufactured using phosphor light conversion.^{2,13,2,14}

Phosphor-based white LEDs excited by blue-emitting LEDs

The blue-emitting LED and YAG:Ce phosphor combined white LED system invented first and is still the principal device found in the market.^{2,15-2,17} The device structure of this system is schematically shown in Fig. 2.1.1 and with its emission spectrum shown in Fig. 2.1.2. The YAG:Ce phosphor absorbs the emission from a blue LED at 460 nm efficiently and converts it to a broad band yellow emission. The YAG:Ce phosphor has certain advantages as below :

- i) Partial substitution of Y with Gd and Al with Ga can shift the emission wavelength between 510 and 590 nm without decreasing efficiency noticeably. By using just a single compound of YAG:Ce, one can obtain white emission of almost any color temperature, except for the warm white equivalent to an incandescent lamp.
- ii) The YAG:Ce phosphor deteriorates only slightly even under severe conditions by virtue of the rigid garnet-type crystal structure.
- iii) The luminescence spectrum is composed of a band with a half width as wide 130 nm. This broad emission band results in a high color rendering index, which is well suited to light sources for general purpose illumination.
- iv) The Ce^{3+} luminescence in YAG has a lifetime as short as $10^{-7} - 10^{-8}$ s, which is advantageous for display applications. Such short persistence is due to 4f–5d transitions, which are parity– and spin–allowed.
- v) The manufacturing process is well established and the mass production process is safe and easy. The materials also have the advantage of low production costs, since it is made from inexpensive starting materials like alumina and yttria.

Phosphor-based white LEDs excited by UV or NUV-emitting LEDs^{2,18,2,19}

White LEDs can also be made by coating near ultraviolet (NUV) emitting LEDs with a mixture of red, green and blue emitting phosphors.^{2.20-2.23} This is a method analogous to the way fluorescent lamps work. White LEDs of this type convert all the emission from UV- or near UV-LEDs to visible light by using phosphors. This method is less efficient than the blue LED with YAG:Ce phosphor, as the Stokes shift is larger and more energy is therefore converted to heat, but yields light with better spectral characteristics, which render color better. We can design emission color with large flexibility using a wide selection and combination of phosphors, particularly white with high color rendering index and an expanded range of color in the chromaticity diagram for backlighting of liquid crystal displays. Moreover, due to the higher radiative output of the ultraviolet LEDs than of the blue ones, this approach offers comparable brightness. However, such devices have not been marketed on a large scale, because of lifetime and efficiency considerations.^{2.24-2.26}

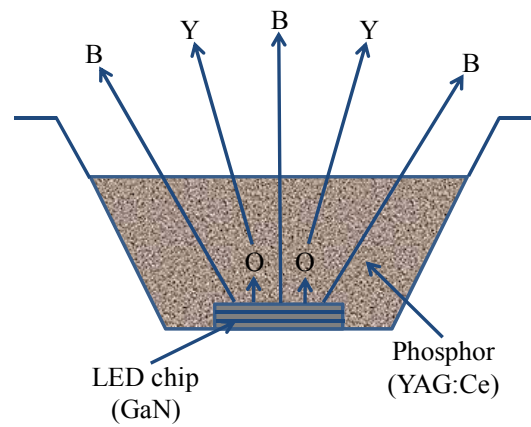


Fig. 2.1.1 The device structure of blue LED and YAG:Ce phosphor combined white LED system.

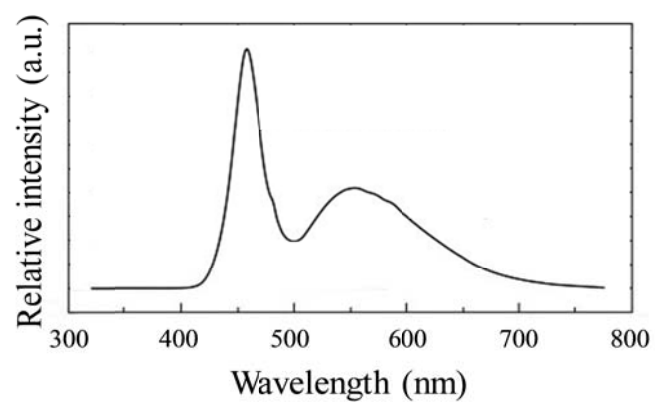


Fig. 2.1.2 Emission spectrum of blue LED and YAG:Ce phosphor combined white LED.

2.1.3 Advantages of spherical and nano-sized phosphors for white LEDs

Decrease of scattering loss^{2,27}

Rayleigh scattering is the elastic scattering of light or other electromagnetic radiation by particles much smaller than the wavelength of the light. The particles may be individual atoms or molecules. It can occur when light travels through transparent solids and liquids, but is most prominently seen in gases. Rayleigh scattering is a function of the electric polarizability of the particles.

The size of a scattering particle is parameterized by the ratio x of its characteristic dimension r and wavelength λ :

$$x = \frac{2\pi r}{\lambda}$$

Rayleigh scattering can be defined as scattering in the small size parameter regime $x \ll 1$. Scattering from larger spherical particles is explained by the Mie theory for an arbitrary size parameter x . For small x the Mie theory reduces to the Rayleigh approximation.

The amount of Rayleigh scattering that occurs for a beam of light depends upon the size of the particles and the wavelength of the light. The Rayleigh scattering intensity of particle, I_s , is determined by the following equation:

$$I_s = \frac{8\pi^4 N_m a^6}{\lambda^4 r^2} \left| \frac{m^2 - 1}{m^2 + 2} \right|^2 (1 + \cos^2 \theta) I_i$$

where I_i is the intensity of incident light, N_m is the refractive index of medium, a is the diameter of particle, m is N_p/N_m (where N_p means the refractive index of particle), λ is the wavelength of the incident light, r is the distance between viewing point and the

nanoparticle and θ is the scattering angle. Since the scattering efficiency of particle depends on the diameter of particle to the sixth power in above equation, it is obvious that using particles with nano-sized is an appropriate strategy for suppressing the scattering loss.

Packing of particles with maximum density^{2,28}

The basic idea of the argument is that if particles of infinitely small size are introduced into a bed of large pieces the small pieces will fill up the voids without changing the total volume. In practice it is found that introducing small pieces into the bed increases the total volume somewhat but the composition of maximum density is still given approximately by the proportion $1 / (1 + V)$ until the sizes of the two components begin to approach each other. Extending the argument to systems of more than two-component sizes, assume that there are several sizes in the system and that each component size fills exactly the voids of the next preceding size, causing no increase in volume of the bed as a whole and leaving no excess material. This is a purely hypothetical case and is used only as a starting-point. Such a system is roughly analogous to a telescope of many sections where each piece slides into the preceding one, or to the sets of hollow interfitting blocks of diminishing size which are used by children for building towers.

An equation will now be developed showing the relation between voids, size composition, and a number of component sizes for uniformly mixed beds of maximum possible density. Let Z be the proportion by absolute volume of the large size in a two-component bed of maximum density-that is, Z is the volume of large-sized material per unit volume of solid matter. Then

$$Z = \frac{1}{1 + V} \quad (2.1.1)$$

Equation 2.1.1 holds only for the case where the solid particles of the different sizes have the same shape so that the voids in the bed of the sized material are the same for each constituent size. In Equation 2.1.1, V is the fraction of voids in a bed of sized material, whereas Z is the actual absolute volume occupied by the larger particles in a two-component system of maximum density, when the actual absolute volume of both large and small particles is unity. Call the diameter of the large particles d_l . The amount of fine material of diameter d_s which will exactly fill the interstices of d_l is $1 - Z$, provided the small particles act as if they are infinitely small. Suppose that another set of infinitely small particles of diameter d_s can be introduced into the voids of the second component. A better way may be to consider momentarily that each component is of finite size but that it has the packing properties of the infinitely small size.

If such an arrangement is assumed, the total absolute volume of each component size will be given by a series of terms of decreasing magnitude, the first term being Z and the second $1 - Z$, as mentioned before. The numerical ratio between the second and first term is $(1 - Z) / Z$. This same factor persists throughout, for the same ratio of voids is left within each constituent size as it is added. Thus the series becomes a geometric progression and

Total absolute volume of solids =

$$Z + (1 - Z) + (1 - Z) \left(\frac{1 - Z}{Z} \right) + \frac{(1 - Z)^2}{Z} \left(\frac{1 - Z}{Z} \right)$$

Since, according to Equation 2.1.1, Z equals $1 / (1 + V)$, the quantity $(1 - Z) / Z$, which is the ratio between terms, is equal to V . Therefore, the equation may be written

$$\text{Total absolute volume of solids} = \frac{d_1 + d_2 + d_3 + d_4 + \dots}{1 + V} \quad (2.1.2)$$

The number of terms in the numerator equals the number of component sizes in the system. This equation applies only when the voids in a bed of the sized material are the same for each component size. Each term represents the absolute volume of the different component sizes in the mixture, the size being designated by the symbols d_1 , d_2 , etc., above each term. If all the solid pieces have the same density, $1 / (1 + V)$ may be considered the actual absolute volume of all the solid pieces of the largest size, d_1 , in a system of maximum density of two or more components. Then the absolute volume of the particles of the second size, d_2 , will be $V / (1 + V)$, of the third size, d_3 , $V^2 / (1 + V)$, etc., as was explained by Equation 2.1.2. As a result, some calculated values of maximum density of packing are arranged in Table 2.1.1.

Table 2.1.1 Packing density of mixed spheres of different size

| Weight Fraction of Spheres | | | | Packing Density(%) | |
|----------------------------|-------|-------|-------|--------------------|--------------|
| d_1 | d_2 | d_3 | d_4 | Calculated | Experimental |
| 1.00 | - | - | - | 60.5 | 58.0 |
| 0.726 | 0.274 | - | - | 84.8 | 80.0 |
| 0.647 | 0.244 | 0.109 | - | 95.2 | 89.8 |
| 0.607 | 0.230 | 0.102 | 0.061 | 97.5 | 95.1 |

2.2 Luminescence

2.2.1 Definition of phosphor^{2.29-2.32}

Materials that generate luminescence are called phosphors. Commercial phosphors are mostly inorganic compounds prepared as powders (with grain sizes usually in the order of 2-20 μm) or thin films. The phosphor materials contain one or more impurity ions or activators (A), typically present in 0.01-100 mol% concentrations. The actual emission is generated on these activator ions. Typical activators are rare earth- or transition-metal ions, ions undergoing s-p transitions (like Bi^{3+}), and molecular anions like the tungstate or vanadate groups. Sensitizers (S) are useful if the activator ions cannot be excited, *e.g.*, because of forbidden transitions. In such cases, the exciting energy is absorbed by the sensitizers and subsequently transferred to the activator ions. Common to all these moieties is the not completely filled electron shell in at least one state (ground state, excited state) involved.

To have any technical importance, a luminescent material must be easily excited by the appropriate excitation and must have high quantum efficiency, the ratio of the number of quanta absorbed to the number emitted. Nonradiative losses are commonly caused by interactions with lattice vibrations and what are known as killer impurities. Further, the activator must convert the energy absorbed to a useful frequency of visible light. A suitable phosphor must maintain well under the excitation mode and must be easily manufactured. The synthesis of efficient phosphors not only requires the best in high temperature chemistry, but also in precursor preparation and handling and purity of starting materials. Device manufacturing involves still other sciences, such as thin film technology and suspension chemistry.

2.2.2 Various type of luminescence

Luminescence is light that usually occurs at low temperatures, and is thus a form of cold body radiation. The followings are types of luminescence and applications. And typical efficiencies were shown in Table 2.2.1.^{2,33}

Photoluminescence^{2,32,2,34}

Photoluminescence (PL) is a process in which a substance absorbs photons and then re-radiates photons. Quantum mechanically, this can be described as an excitation to a higher energy state and then a return to a lower energy state accompanied by the emission of a photon. Light emission that persists after the cessation of excitation is called after-glow. Photoluminescence is divided into fluorescence and phosphorescence according to the duration time of the after-glow, and the difference of two kinds was explained briefly in Fig. 2.2.1. Fluorescence implies light emission during excitation. Therefore, fluorescence is the process in which the emission decay is ruled by the lifetime (< 10 ms) of the emitting state of a luminescence center, while the phosphorescence process is ruled by a quasistable state of a center or a trap.

Fluorescence^{2,35}

Fluorescence is the emission of electromagnetic radiation light by a substance that has absorbed radiation of a different wavelength. In most cases, absorption of light of a certain wavelength induces the emission of light with a longer wavelength (lower energy). The energy difference between the absorbed and emitted photons is due to thermal losses. Dissipation of vibration energy occurs on a much greater time scale

than fluorescent emission. The most striking examples of this phenomenon occur when the absorbed photon is in the ultraviolet region of the spectrum, and is thus invisible, and the emitted light is in the visible region.

Phosphorescence^{2,35}

Phosphorescence is a specific type of photoluminescence related to fluorescence. Unlike fluorescence, a phosphorescent material does not immediately re-emit the radiation it absorbs. The slower time scales of the re-emission are associated with forbidden energy state transitions in quantum mechanics. As these transitions occur less often in certain materials, absorbed radiation may be re-emitted at a lower intensity for up to several hours.

Electroluminescence^{2,36,2,37}

Electroluminescence (EL) is an optical phenomenon and electrical phenomenon in which a material emits light in response to an electric current passed through it, or to a strong electric field. Electroluminescence is the result of radiative recombination of electrons and holes in a material. The excited electrons release their energy as photons, light. Prior to recombination, electrons and holes are separated either as a result of doping of the material to form a p-n junction or through excitation by impact of high-energy electrons accelerated by a strong electric field.

Cathodoluminescence^{2,38}

Cathodoluminescence is an optical and electrical phenomenon whereby a beam of electrons is generated by an electron gun and then impacts on a luminescent material such as a phosphor, causing the material to emit visible light. The most common example is the screen of a television. Cathodoluminescence occurs because the impingement of a high energy electron beam onto a semiconductor will result in the promotion of electrons from the valence band into the conduction band, leaving behind a hole. When an electron and a hole recombine, it is possible for a photon to be emitted. The energy of the photon, and the probability that a photon and not a phonon will be emitted, depends on the material, its purity, and its defect state. In terms of band structure, classical semiconductors, insulators, ceramics, gemstones, minerals, and glasses can be treated the same way.

2.2.3 Material compositions of phosphor

Luminescent materials, also called phosphors, are mostly solid inorganic materials consisting of a host lattice, usually intentionally doped with impurities. The impurity concentrations generally are low in view of the fact that at higher concentrations the efficiency of the luminescence process usually decreases (concentration quenching). In addition, most of the phosphors have a white body color. Especially for fluorescent lamps, this is an essential feature to prevent absorption of visible light by the phosphors used. The absorption of energy, which is used to excite the luminescence, takes place by either the host lattice or by intentionally doped impurities. In most cases, the emission takes place on the impurity ions, which, when they also generate the desired emission, are called activator ions. When the activator ions show too weak absorption, a second kind of impurities can be added (sensitizer), which absorb the energy and subsequently transfer the energy to the activator.^{2.39-2.43} This process involves transport of energy through the luminescent materials. Quite frequently, the emission color can be adjusted by choosing the proper impurity ion, without changing the host lattice in which the impurity ions are incorporated. The electronic transitions and examples of impurities ions (activator) are shown in Table 2.2.2.^{2.44}

2.2.4 Configuration coordinate model

The configuration coordinate model is used to address the optical properties of a localized emitting center and its interaction with the host crystal lattice.^{2,45,2,46} The model describes the effect of neighboring atomic sites on a luminescent ion. If the crystal structure is orthorhombic, the activators have six neighboring ions. Local vibration modes of the lattice constitute a set of configuration coordinates. Usually the totally symmetric vibration mode (breathing mode) is used. In this mode, the configuration coordinate, Q represents the distance between activator and neighboring ions. This follows from the fact that the adiabatic potential of a diatomic molecule is a function of the inter-atomic distance. Potential curves representing the total energy (electron plus ion) of the luminescent molecule in ground and excited states as a function of the configuration coordinates are employed and these are shown in Fig. 2.2.3 and 2.2.4.^{2,47}

Fig. 2.2.4 illustrates a configuration coordinate diagram for a simplified two-level system. The equilibrium position of the excited state is shifted an amount Q_0 from the equilibrium position of the ground state located at zero. Vertical lines from A to B and from C to D represent light absorption and emission, respectively. The configuration coordinate model explains the energy discrepancy between absorption and emission, known as Stoke's law, shown in Fig. 2.2.5. That is, the absorption energy is higher, and therefore the emitted radiation is of longer wavelength. It also explains the relative widths of the absorption and emission bands. The classical description does not provide a complete explanation of the observed phenomenon.

A quantum mechanical description must be used to explain experimentally observed spectral shapes and non-radiative transition probabilities. Therefore, the energy state of

the activator can be described by a wave function Ψ which is dependent on both electronic and nuclear coordinates.

During absorption, the energy supplied in the transition is followed by system relaxation via phonon emission. Then emission of a photon can occur in the transition back to the ground state. Absorption and emission peaks are shifted relative to one another as shown in Fig. 2.2.5 (Stokes shift).^{2,48} Also, the width of the absorption and emission bands is temperature dependent. Electron-phonon interaction results in the broadening of the emission spectra.

2.2.5 Crystal field theory

Coulomb interaction between valence electrons of an ion and the host electrostatic field perturbs the energy level structure of the dopant ion, consequently splitting the free ion energy levels.^{2.49-2.52} Within the framework of group theory, the energy level splitting is shown to be due to a reduction of the rotational symmetry of a free ion. The ligand ions are considered point particles within a Coulomb field. The influence of ion inner electrons can be approximated as a central field given that transitions primarily involve the valence electrons. Using these approximations, the Hamiltonian for an ion in a crystal field is:

$$H = \sum_i \left(\frac{\vec{p}_i^2}{2m} + V(r_i) \right) + \sum_{i>j} \frac{e^2}{4\pi\epsilon_0 r_{ij}} + \sum_i \zeta(r_i) \vec{l}_i \cdot \vec{s}_i + \frac{1}{4\pi\epsilon_0} \sum_i \sum_j \frac{Z_k e^2}{|\vec{R}_k - \vec{r}_i|}$$

The first term on the right represents the energy of the valence electrons in an effective spherical potential $V(H_o)$. The second term is the interaction energy between valence electrons (H'). The third term gives the contribution of spin-orbit coupling (H_{so}). The last term, known as the crystal field Hamiltonian, accounts for the effective field of the host (H_c). For discussion, we write above equation and terms described successively as $H = H_0 + H' + H_{so} + H_c$. When solving for the energy eigenvalues, the crystal field Hamiltonian is solved most easily when expressed in terms of spherical harmonics.

For rare earth ions, the crystal field Hamiltonian is treated as a perturbation with eigenvectors taken as eigenstates of the above equation neglecting the last term. This is the weak crystal field approximation ($H' \gg H_c$). In this case, the crystal field energy is small in comparison to the configuration interaction and spin-orbit interaction. Spin-orbit interaction is initially neglected for the intermediate crystal field case ($H' > H_c$),

and electron configuration interaction modifies the eigenfunctions. When the crystal field is strong ($H' < H_c$), electrostatic interaction can be neglected and spin-orbit coupling is the most significant perturbation. Rare earth ions such as Eu^{2+} have a partially filled 4f shell requiring 14 electrons to completely fill it.^{2.53,2.54} The energy level structure in this rare earth ions is $1s^2 2s^2 2p^6 3s^2 3p^6 3d^{10} 4s^2 4p^6 5s^2 5p^6 4f^n$ ($n=1, \dots, 14$). $5s^2$ and $5p^6$ electrons partially shield the 4f electrons, resulting in mild energy level perturbations in contrast to the transition metal ions, whose outer 3d electrons are heavily affected by the ligand field. The low-lying excited states are optically active. In Eu^{2+} , one of the 4f electrons is transferred to a 5d orbital resulting in two split $4f^6 5d^1$ states. The five-fold degeneracy of the 5d levels is completely removed. A schematic representation of the crystal field splitting of the $4f^6 5d^1$ level is shown in Fig. 2.2.6.

2.2.6 Decay of luminescence

The decay process of the luminescence intensity $I(t)$ after the termination of excitation at $t = 0$ is generally represented by an exponential function of the elapsed time after the excitation.^{2.44,2.55-2.57}

$$I(t) = I_0 \exp\left(-\frac{t}{\tau}\right)$$

τ is the decay time constant of the emission. If one denotes the number of excited luminescence centers in a unit volume by n^* , and the radiative and non-radiative transition probabilities by W_R and W_{NR} , respectively, then the rate equation for n^* is:

$$\frac{dn^*}{dt} = -(W_R + W_{NR})n^*$$

and the solution of this equation is:

$$n^*(t) = n_0^* \exp[-(W_R + W_{NR})t]$$

n_0^* is the value at $t = 0$, that is, at the end-point of excitation or, in other words, at the start point of the after-glow.

Therefore, the lifetime of the center, which corresponds to the elapsed time for n^* to be decreased by the factor of e^{-1} of n_0^* , is $(W_R + W_{NR})^{-1}$. Since the emission intensity is proportional to n^* , the decay time of the after-glow in equation $I(t) = I_0 \exp(-\frac{t}{\tau})$ is equal to the lifetime of the center:

$$\tau = (W_R + W_{NR})^{-1}$$

and the luminescence efficiency of the center is given by:

$$\eta = \frac{W_R}{W_R + W_{NR}}$$

Table 2.2.1 Luminescence type, applications and typical efficiencies.

| Luminescence type | Typical application | Efficiency |
|---------------------|------------------------|------------|
| Blackbody radiation | Tungsten filament lamp | ~ 5 % |
| Photoluminescence | Fluorescent lamp | ~ 20 % |
| Cathodoluminescence | Television | ~ 10 % |
| Electroluminescence | Light emitting diode | 0.1 – 50 % |
| | Flat panel display | |

Table 2.2.2 The electronic transitions and examples of impurities ions (activator).

| Electronic transition | Example |
|--|---|
| $1s \Leftrightarrow 2p$ | F center |
| $ns^2 \Leftrightarrow nsnp$ | Tl ⁺ -type ions (Ga ⁺ , In ⁺ , Tl ⁺ , Ge ²⁺ , Sn ²⁺ , Ag ⁻ , Au ⁻ , etc) |
| $3d^{10} \Leftrightarrow 3d^9 4s$ | Ag ⁺ , Cu ⁺ and Au ⁺ |
| $3d^n \Leftrightarrow 3d^n, 4d^n \Leftrightarrow 4d^n$ | The first and second row transition metal ions (Cr ³⁺ , Mn ⁴⁺ , Mn ²⁺ , Fe ³⁺ , etc) |
| $4f^n \Leftrightarrow 4f^n, 5f^n \Leftrightarrow 5f^n$ | Rare-earth and actinide ions (Eu ³⁺ , Sm ³⁺ , Tb ³⁺ , Dy ³⁺ , etc) |
| $4f^n \Leftrightarrow 4f^{n-1} 5d$ | Ce ³⁺ , Pr ³⁺ , Sm ²⁺ , Eu ²⁺ , Tm ²⁺ and Yb ²⁺ |

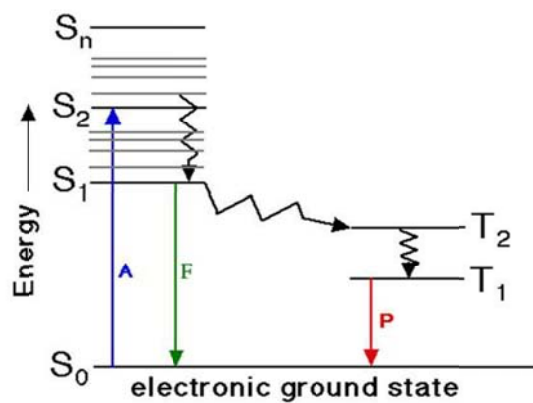


Fig. 2.2.1 Schematic descriptions about the difference between fluorescence and phosphorescence (A = Absorption, F = Fluorescence, P = Phosphorescence, S = Singlet state ($\uparrow\downarrow$), T = Triplet state ($\uparrow\uparrow$)).

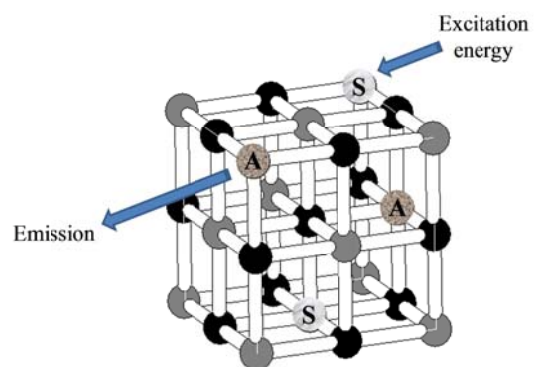


Fig. 2.2.2 Luminescent material containing activator (A) and sensitizer (S).

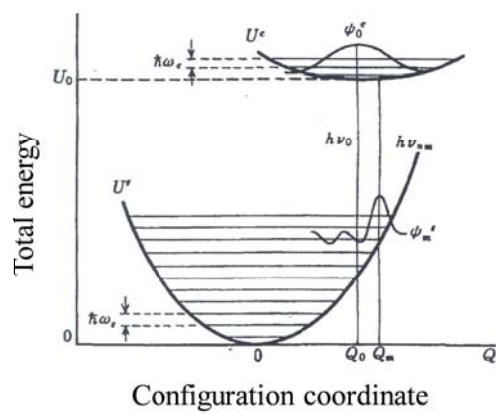


Fig. 2.2.3 Configuration coordinate model with discrete harmonic oscillator energy levels for a localized center.

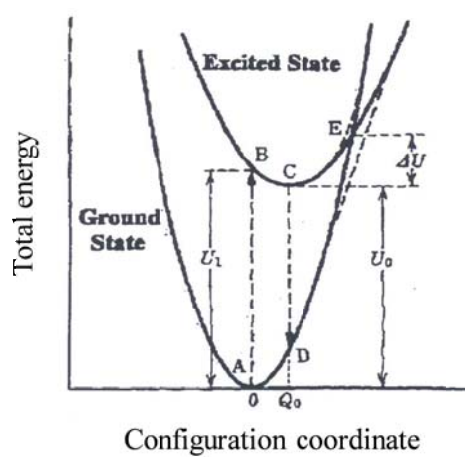


Fig. 2.2.4 Simplified configuration coordinate diagram for a two-level system.

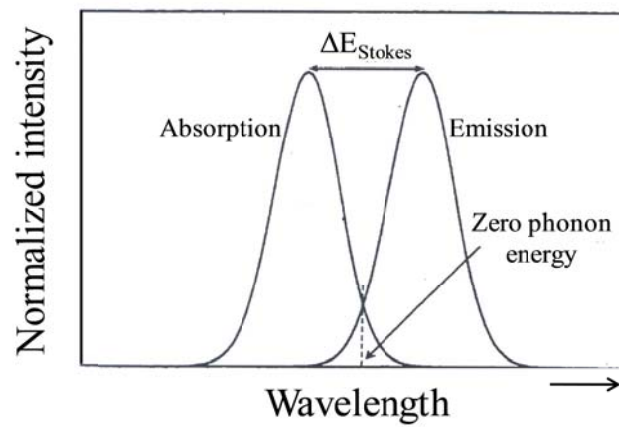


Fig. 2.2.5 Stokes shift in absorption and emission spectra for a two-level system.

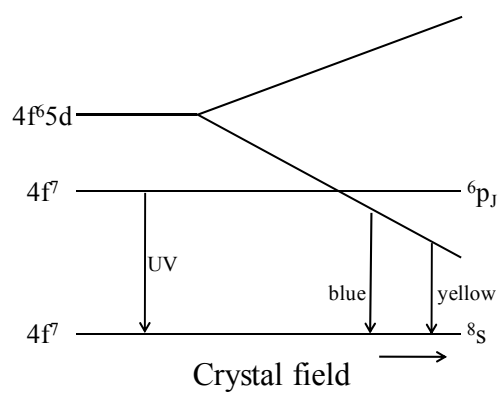


Fig. 2.2.6 Schematic depiction of energy level splitting of the $4f^6 5d^1$ level in Eu^{2+} by the crystal field.

2.3 Synthesis of monodispersed and nano-sized particles as building blocks^{2.58}

2.3.1 Mechanism of formation

The scheme in Fig. 2.3.1 shows the sequence of essential events in the precipitation process leading to the formation of colloidal particles, the chemical and physical properties of which depend in a sensitive manner on each step. Obviously, there are two major paths that may yield monodispersed particles. Originally, the widely accepted way to achieve the size uniformity was to follow the left-hand side of the scheme by which particles are formed through the attachment of solutes onto preferred nuclei. Accordingly, there should be a rapid burst of nuclei, which would be allowed to grow uniformly, as proposed by LaMer.^{2.59,2.60} While this kinetic explanation is appealing in principle, it is by no means as general as originally assumed to be.

In contrast, it has now been demonstrated in numerous cases that the formation of many, if not most of the colloids proceeds through a more complex process. The stages up to nanosized particles may be the same, but instead for the growth to continue by diffusion of constituent species onto these precursors, these singlets aggregate to yield coarser dispersions, which are in most cases of broad size distributions. However, under certain conditions the products may consist of rather uniform larger particles. It is to be expected that the latter will be obtained under considerable constraints with respect to the experimental conditions. For this reason, it is not surprising to note the paucity of such systems produced before the middle of the last century.

To explain the mechanism by which uniform spherical particles may be generated

by aggregation of nanosize subunits, the first question to be answered is how to explain the propensity of nanosize particles to aggregate rather than to continue to grow by diffusional transport. It is obvious that, in the course of the precipitation process conditions that kept these precursor singlets apart, must change to cause their loss of stability. In most of the studied inorganic systems, this partial stability is due to electrostatic repulsion. Thus, during the particle formation, the charge on the nanosized singlets must be either neutralized or shielded to eliminate repulsion. The former may take place, for example, if due to chemical changes in the reacting solution the pH is shifted towards the isoelectric point of the dispersed solids, rendering them unstable. In the second case, the ionic strength may increase sufficiently allowing for particles to aggregate.

The next task is to establish conditions under which such aggregation can lead to size selection, i.e., to colloids of narrow size distribution. There is extensive literature dealing with aggregation processes. Usually, models of coagulation and nucleation have assumed diffusional transport and considered the growth of particles and aggregates, either via microscopic nucleation processes^{2.61,2.62} or by particle-particle aggregation and aggregate-aggregate adhesion on encounters.^{2.63,2.64} Models of dilute systems typically produce size distributions that peak at small sizes, while larger aggregates normally result in size distributions that grow with time.

A different novel approach was developed by the author in collaboration with his colleagues V. Privman and D.V. Goia.^{2.65} The main finding has been that the growth of the final particles by aggregation of singlets must be coupled with the rate of their formation. Numerical calculations indicated that, if the concentration of singlets were constant, i.e., if they were continuously generated to compensate for their depletion due to aggregation, the resulting particles would be of broad size distribution peaked at

small diameters. However, if the process is carried out to allow for the concentration of primary particles to decrease with time, size selection can be achieved.

To formulate the model, it is assumed that the diffusion constant of singlets is larger than that of the aggregates so that the attachment prevails. The standard rate equation then reads

$$\frac{dN_s}{dt} = w_{s-1}N_{s-1} - w_sN_s \quad \text{for } s > 1 \quad 2.3.1$$

where $N_s(t)$ is the time-dependent density of secondary particles containing s primary particles.

In normal approaches to aggregation, the evolution of the population of singlets, which is not covered by Equation 2.3.1, is obtained by the conservation of matter

$$N_1(t) + \sum_{j=2}^{\infty} jN_j(t) = N_1(0) \quad 2.3.2$$

which assumes that, at $t = 0$, there are only singlets.

Equations 2.3.1 and 2.3.2 need to be modified to conform by introducing a term that accounts for the rate $\rho(t)$ at which primary particles are formed per unit volume. Consequently, the equation for $N(t)$ is modified by replacing Equation 2.3.2 with

$$N_1(t) = \int_0^t \rho(t')dt' - \sum_{j=2}^{\infty} jN_j(t) \quad 2.3.3$$

with initial values of $N_s(0) = 0$ for all $s = 1, 2, 3$ from classical nucleation theory.

An expression for $\rho(t)$ was developed which includes experimentally accessible parameters,

$$\rho(t) = \frac{32\pi^2 a^3 \sigma D c^2}{3kT \ln(c/c_0)} \exp \left\{ -\frac{256\pi^3 a^6 \sigma^3}{27(kT)^3 [\ln(c/c_0)]^2} \right\} \quad 2.3.4$$

where $c(t)$ is the concentration of solute species (atoms, ions), which serve as

monomers for primary particles nucleation, while c_0 is its equilibrium saturation concentration. Finally, σ is the effective surface tension of the singlets.^{2,63}

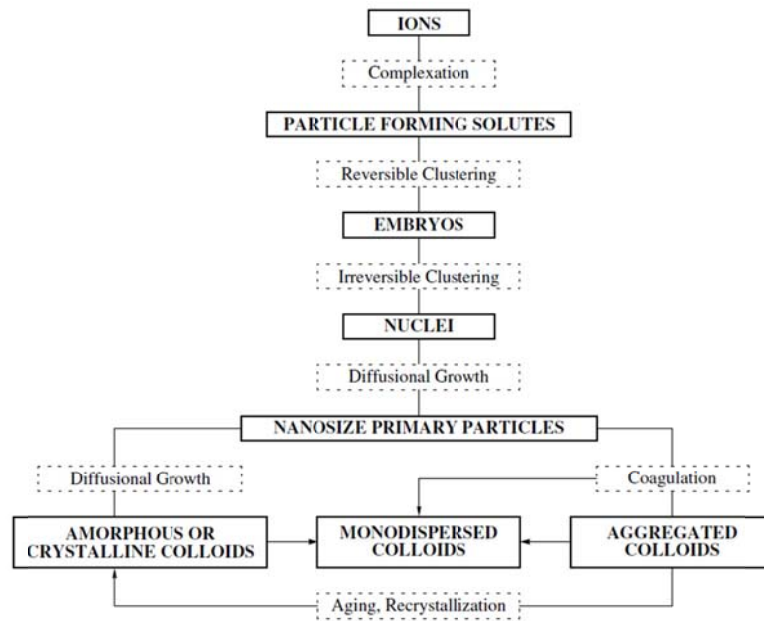


Fig. 2.3.1 Stages in the precipitation of colloid particles in homogeneous solutions.

2.4 Materials

2.4.1 Al_2O_3

Structure of Al_2O_3

Aluminium oxide is an amphoteric oxide with the chemical formula Al_2O_3 . It is commonly referred to as alumina (α -alumina), or corundum in its crystalline form, as well as many other names, reflecting its widespread occurrence in nature and industry. There is also a cubic γ -alumina with important technical applications.

The most common form of crystalline alumina is known as corundum. The oxygen ions nearly form a hexagonal close-packed structure with aluminium ions filling two-thirds of the octahedral interstices. Each Al^{3+} center is octahedral. In terms of its crystallography, corundum adopts a trigonal Bravais lattice with a space group of $R\bar{3}c$. The primitive cell contains two formula units of aluminium oxide. Alumina also exists in other phases, namely γ -, δ -, η -, θ -, and χ -aluminas.^{2.66} Each has a unique crystal structure and properties. The so-called β -alumina proved to be $\text{NaAl}_{11}\text{O}_{17}$.^{2.67}

2.4.2 $\text{Y}_3\text{Al}_5\text{O}_{12}:\text{Ce}^{3+}$

Structure of $\text{Y}_3\text{Al}_5\text{O}_{12}$

$\text{Y}_3\text{Al}_5\text{O}_{12}$ called YAG because of its garnet structure, belongs to the cubic space group O_h^{10} (Ia₃d) and contains eight formula units per unit cell.^{2.68,2.69} The crystal can be described by the formula $\text{C}_3\text{A}_2\text{D}_3\text{O}_{12}$ where the Y^{3+} ions sit in dodecahedral C sites and the Al^{3+} ions occupy both tetrahedral D sites and trigonally distorted octahedral A sites.^{2.68,2.70,2.71} In the YAG system, the Y^{3+} site occupied by Ce^{3+} has distorted cubic symmetry that can be described by a rhombic D_2 point group.^{2.72}

General luminescent properties of $\text{Y}_3\text{Al}_5\text{O}_{12}:\text{Ce}^{3+}$ phosphor

Three Ce^{3+} absorption bands appeared in the excitation spectrum with peaks at 220, 340 and 450 nm. The band at 220 nm was very weak because the upper 5d states of Ce^{3+} in YAG have energies within the conduction band of the host, so that the excitation in these levels results mainly in quenching.^{2.73} The 5d level of Ce^{3+} populated by the transition occurring at 340 nm is just below the YAG conduction band and will also be partially quenched at room temperature.^{2.73} The most intense band peak at 450 nm was associated with the $4f \rightarrow 5d$ ($^2\text{A}_{1g}$) transitions of Ce^{3+} .^{2.74} The emission band of the YAG:Ce was located between 500 and 700 nm and peaked at 560 nm.

2.4.3 BaAl₂O₄:Eu²⁺

Structure of BaAl₂O₄^{2.75-2.77}

BaAl₂O₄ belongs to the large family of stuffed tridymite structures which are derived from the structure of SiO₂ β tridymite. As Al³⁺ replaces Si⁴⁺ in the tetrahedra of SiO₂ tridymite, Ba will occupy sites in channels parallel to the c-axis. At room temperature, BaAl₂O₄ is hexagonal P6₃ and has a superstructure with unit cell parameters 2A, C, where A and C are the lattice parameters of hexagonal tridymite. Projection of BaAl₂O₄ along (001) crystal plane is composed of AlO₄ tetrahedra. Three pointing-up AlO₄ tetrahedra alternately connect three pointing-down AlO₄ tetrahedra by corner sharing to form a six-member ring. Six-member rings link to each other by a common oxygen of the pointing-up or -down tetrahedra to form the channels parallel to c-axis. These channels are further connected to form a 3-D framework through common AlO₄ tetrahedra.

General luminescent properties of BaAl₂O₄:Eu²⁺ phosphor

The excitation spectrum of BaAl₂O₄:Eu²⁺ is made up of three main peaks at 280, 340 and 400 nm, corresponding to the 4f⁷-4f⁶5d transitions of Eu²⁺, respectively,^{2.78-2.80} and the 340 nm peak is the strongest. As exciting with wavelengths 280, 340 and 400 nm, respectively, similar emission spectrum was always observed with a peak at ~498 nm due to the Eu²⁺ transition of 4f⁶5d-4f⁷, which shows no dependence of the emission spectra on the excitation wavelengths in BaAl₂O₄:Eu²⁺. In the structure of the BaAl₂O₄ compound, there are two different barium sites Ba(1) and Ba(2).^{2.75-2.77} Ba(1) and Ba(2)

are positioned on 6c and 2a and coordinated by nine oxygen ions with average Ba-O distances of 2.97 Å for Ba(1) and 2.89 Å for Ba(2), respectively.^{2.75} The emission band of BaAl₂O₄:Eu²⁺ is separated into two Gaussians with the maxima at about 495 and 530 nm, respectively (see Fig. 2.4.5). The splitting of 5d-excitation level of Eu²⁺ ion in solid-state compounds depends strongly on the strength of crystal field around Eu²⁺ ion. When the crystal environments are analogous, the Eu²⁺ center with shorter Eu²⁺-O²⁻ distance will give a longer emission. Therefore, the 495 nm emission peak is related to the Eu²⁺ ion on Ba(1) site, and the 530 nm emission is related to the Eu²⁺ ion on Ba(2) site. The emission intensity of 495 nm is about three times more intensive than that of 530 nm, the ratio roughly agrees with the content ratio between Ba(1) and Ba(2) sites in BaAl₂O₄.^{2.75-2.77}

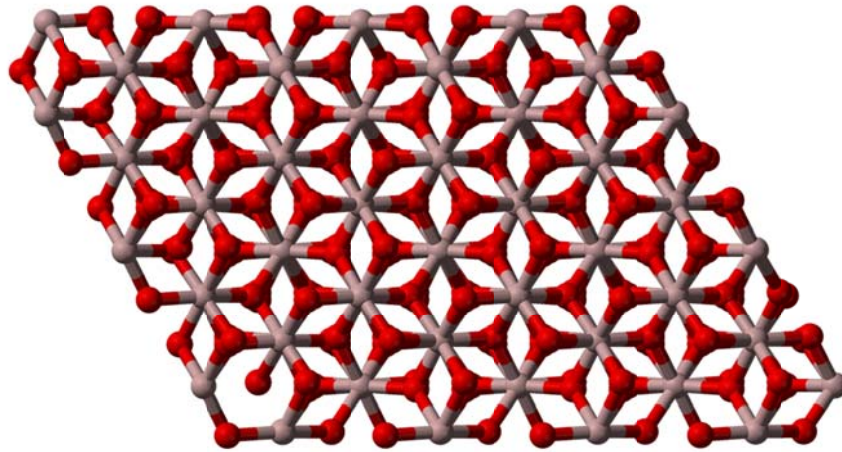


Fig. 2.4.1 Unit cell structure of α - Al_2O_3 .

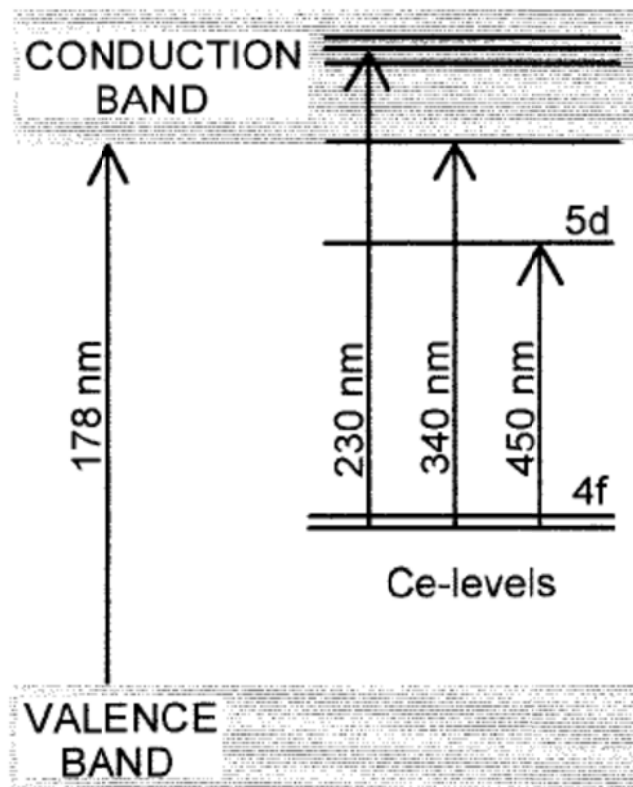


Fig. 2.4.2 Schematic diagram of the energy level and band structure of YAG:Ce single crystal.

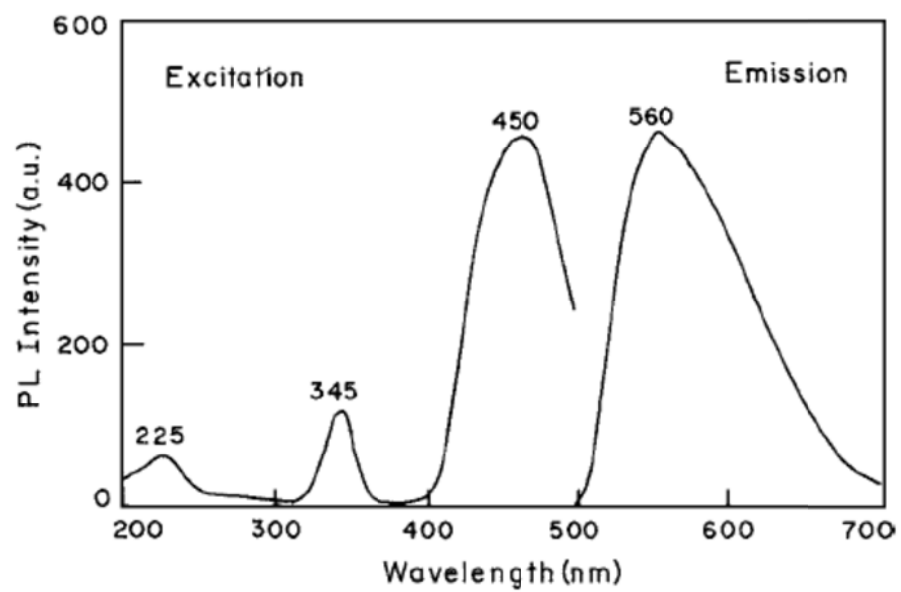


Fig. 2.4.3 Room-temperature excitation and emission spectra of YAG:Ce.

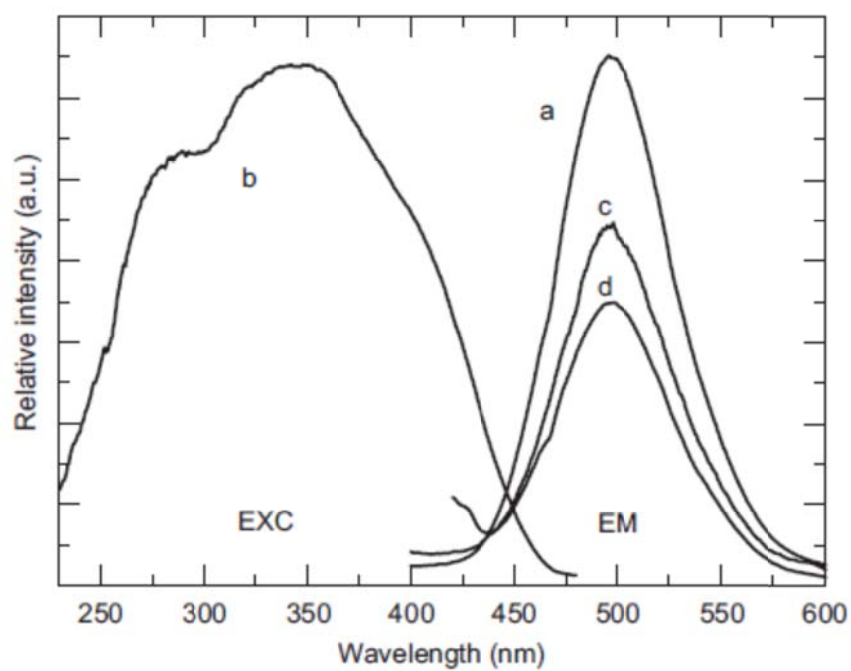


Fig. 2.4.4 Emission (a: λ_{exc} 340 nm, c: λ_{exc} 280 nm, d: λ_{exc} 400 nm) and excitation (b: λ_{em} 498 nm) spectra of BaAl₂O₄:Eu²⁺ phosphors.

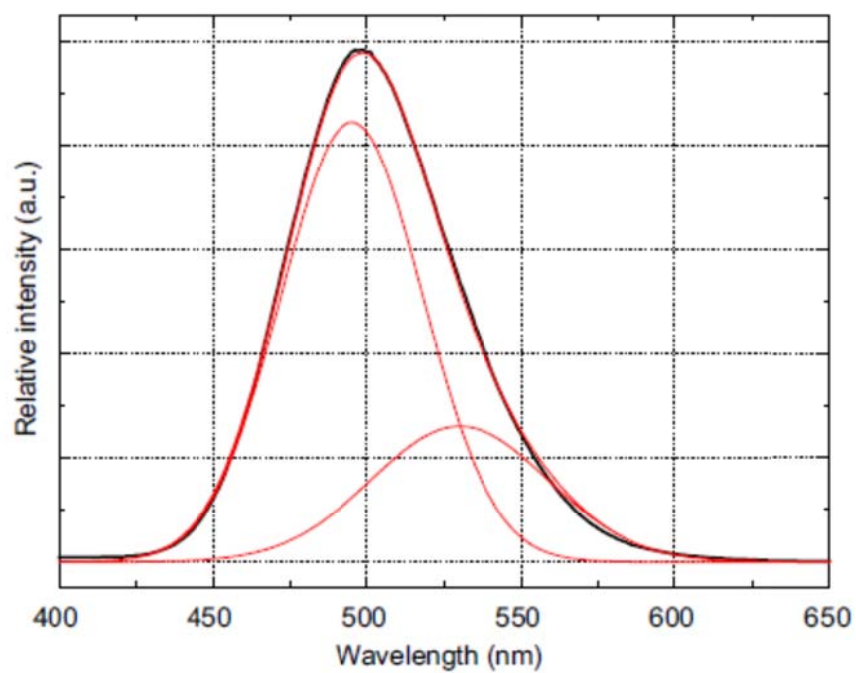


Fig. 2.4.5 Gaussian fit of the emission spectrum of BaAl₂O₄:Eu²⁺ excited at 340 nm at room temperature into two components. Black line is the experimental results and red line is the fitting results.

Chapter 3 Experimental Procedure

3.1 Synthesis

3.1.1 Size-controlled synthesis of monodispersed mesoporous α -alumina spheres

A 100 mL solution was prepared by dissolving reagent grade of $\text{Al}_2(\text{SO}_4)_3 \cdot 16\text{H}_2\text{O}$ (Fluka, 95%), $\text{Al}(\text{NO}_3)_3 \cdot 9\text{H}_2\text{O}$ (Sigma-Aldrich, 98%), and urea (Oriental Chemical Industry, extra pure) in deionized water. To synthesize various sizes of monodispersed spherical aluminum hydrous oxide nanoprecursors, the total concentration of Al^{3+} and urea were fixed at 0.01 M and 0.1 M, respectively, and the concentration ratio of $\text{Al}_2(\text{SO}_4)_3 \cdot 16\text{H}_2\text{O}$ to $\text{Al}(\text{NO}_3)_3 \cdot 9\text{H}_2\text{O}$ was changed. The reactant solutions were reacted in a 98 °C oil bath for 1 h and 30 min. After the reaction, the obtained suspensions were purified from the occluded SO_4^{2-} and NO_3^- by repeated washings with deionized water. The synthesized aluminum hydrous oxide precursors were calcined in air to transform them into $\alpha\text{-Al}_2\text{O}_3$ under various heat conditions.

3.1.2 Synthesis of monodispersed $\text{Y}_3\text{Al}_5\text{O}_{12}:\text{Ce}^{3+}$ nanosphere phosphor

A 100 mL solution was prepared by dissolving 1.1 mM of $\text{Al}_2(\text{SO}_4)_3 \cdot 16\text{H}_2\text{O}$ (Fluka, 95%), 7.722 mM of $\text{Y}(\text{NO}_3)_3 \cdot 6\text{H}_2\text{O}$ (High Purity Chemicals, 99.9%), 0.078 mM of $\text{Ce}(\text{NO}_3)_3 \cdot 6\text{H}_2\text{O}$ (High Purity Chemicals, 99.9%), and 0.1 M of urea (Oriental Chemical Industry, extra pure) in deionized water. The well-mixed solution was reacted in an oil bath at 97 °C for either 44, 46, 48, 50 or 52 min. After reaction, the obtained suspensions were purified from the occluded SO_4^{2-} and NO_3^- by repeated washings with deionized water. The synthesized precursors were annealed in air at various temperatures for 6 h to transform them into YAG:Ce. The obtained samples were denoted as R44, R46, R48, R50 and R52 before annealing and R44-T, R46-T, R48-T, R50-T and R52-T after annealing, respectively (where R+number and T meant reaction time and annealing temperature, respectively.).

3.1.3 Synthesis of monodispersed and size-tunable $\text{BaAl}_2\text{O}_4\text{:Eu}^{2+}$ nanosphere phosphor using $\gamma\text{-Al}_2\text{O}_3$ nanosphere as a template

$\gamma\text{-Al}_2\text{O}_3$ nanospheres were prepared by the method described in chapter 3.1.1. Aluminum hydrous oxide nanoprecursors were synthesized by changing the concentration ratio of $\text{Al}_2(\text{SO}_4)_3 \cdot 16\text{H}_2\text{O}$ to $\text{Al}(\text{NO}_3)_3 \cdot 9\text{H}_2\text{O}$ through a forced hydrolysis method. The reaction time of all conditions was 2 h and all synthesized aluminum hydrous oxide nanoprecursors calcined in air at 900 °C for 2 h to transform them into $\gamma\text{-Al}_2\text{O}_3$.

$\text{BaAl}_2\text{O}_4\text{:Eu}^{2+}$ nanosphere phosphor was synthesized by a forced hydrolysis method using the as-prepared $\gamma\text{-Al}_2\text{O}_3$ nanospheres as a template. A 100 mL solution was prepared by dissolving 0.0099 M of $\text{Ba}(\text{NO}_3)_2$ (Sigma-Aldrich, 99%), 0.0001 M of $\text{Eu}(\text{NO}_3)_3 \cdot x\text{H}_2\text{O}$ (High Purity Chemicals, 99.9%), 0.03 g of $\gamma\text{-Al}_2\text{O}_3$, and 0.1 M of urea (Oriental Chemical Industry, extra pure) in deionized water. The well-mixed solution was reacted in an oil bath at 80 °C for either 1, 2 or 3 h. After reaction, the obtained suspensions were purified from the occluded and NO_3^- by repeated washings with deionized water. The synthesized precursors were annealed in air at various temperatures for various hours to transform them into BaAl_2O_4 . The obtained samples were denoted as γ +number before second forced hydrolysis reaction, γ +number-R after second forced hydrolysis and γ +number-R-T:h after annealing, respectively (where γ +number, R, T and h meant the concentration ratio of $\text{Al}_2(\text{SO}_4)_3 \cdot 16\text{H}_2\text{O}$ to $\text{Al}(\text{NO}_3)_3 \cdot 9\text{H}_2\text{O}$ of $\gamma\text{-Al}_2\text{O}_3$ template, reaction time, annealing temperature and annealing time, respectively.).

3.2 Characterization

A simultaneous thermogravimetric and differential thermal analysis (TG/DTA, STA-1500, TA Instruments Inc.) was used for thermal analysis of the synthesized aluminum hydroxide to help determine and set the heat treatment condition. Powder X-ray diffraction (XRD, M18XHF-SRA, Mac Science Co.) was used for crystal phase identification. The morphology and the size of the synthesized particles were observed by field-emission scanning electron microscopy (FESEM, JSM-6330F, JEOL) and transmission electron microscopy (TEM, JEM-3000F, JEOL). The crystallinity of the prepared particles was determined by a selected area electron diffraction (SAED) coupled with TEM. Energy dispersive spectroscopy (EDS) analysis was performed by Tecnai F20 (Philips) to investigate the local chemical composition of the synthesized particles. The average size and distribution of the synthesized particles in the dispersed solution were evaluated by dynamic light scattering (DLS, DLS-7000, Otsuka Electronics). The suspension was prepared by dispersing the synthesized particles in ethanol without filtration. The result as a number distribution was used to determine the average size of the particles. Additionally, the specific surface areas and the pore size distributions of the products were examined using the Brunauer-Emmett-Teller and Barrett-Joyner-Halenda (BET/ BJH, model Belsorp-mini II, BEL Japan Inc.) method along with a nitrogen adsorption/desorption process. The photoluminescence (PL) spectra were taken on an LS-55 (PerkinElmer) fluorescence spectrometer equipped with a pulsed Xenon lamp as a light source (the power of the Xenon lamp equivalent to 20 kW for 8 μ s duration). The photostability of phosphors was measured by a read method of the LS-55 under blue excitation at 455 nm. The Quantum efficiency (QE) of the synthesized phosphor particles was analyzed using a PL QE

measurement system equipped with an integrating sphere (QE-1100, Otsuka Electronics). Inductively coupled plasma mass spectrometry (ICP-MS) was performed by a Varian 820-MS (Varian) to investigate chemical composition of samples.

Chapter 4 Synthesis of monodispersed and size-tunable aluminate by a forced hydrolysis

4.1 Size-controlled synthesis of monodispersed mesoporous α -alumina spheres

Synthesis of various sizes of monodispersed spherical aluminum hydrous oxide nanoprecursors by changing the concentration ratio of $Al_2(SO_4)_3 \cdot 16H_2O$ to $Al(NO_3)_3 \cdot 9H_2O$

For the initial preparation of aluminum hydrous oxide nanoprecursors, the concentration ratio of $Al_2(SO_4)_3 \cdot 16H_2O$ to $Al(NO_3)_3 \cdot 9H_2O$ (hereafter R) of reactant solutions are listed in Table 4.1.1. The typical FESEM images shown in Fig. 4.1.1 reveal that the prepared precursors consist of nanospheres with uniform diameters. More importantly, the size of these nanospheres systematically decreased as R of the reactant solution decreased. It has been reported that nucleation and growth processes were controlled by the slow hydrolysis of the urea present in the solution.^{4.1} The FESEM image in Fig. 4.1.2 further indicates that each aluminum hydrous oxide sphere consists of tiny nanoparticles whose average crystallite size is about 15 nm. Therefore, during the forced hydrolysis reaction in this study, it is believed that nuclei grow to nanosized primary particles, and then coagulate to form much larger final colloids in a process dominated by the irreversible capture of these primary particles.^{4.2-4.6}

Furthermore, V. Privman *et al.* described a kinetic model that explains the formation of dispersions with narrow size distributions in the above nucleation model.^{4.7}

According to V. Privman *et al.*, the size of the final synthesized particle in such a nucleation model is described by an equation, $\rho(t)$, which accounts for the formation rate of the primary particles by the diffusional capture of solutes per unit volume, and it includes experimentally accessible parameters, and it follows,

$$\rho(t) = \frac{32\pi^2 a^3 \sigma D c^2}{3kT \ln(c/c_0)} \exp \left\{ -\frac{256\pi^3 a^6 \sigma^3}{27(kT)^3 [\ln(c/c_0)]^2} \right\} \quad (4.1.1)$$

where a is the effective radius of the solute, D is the diffusion constant of the solute, and $c(t)$ is the concentration of the solute species (atoms, ions), which serve as monomers for primary particle nucleation, while c_0 is the equilibrium saturation concentration. Finally, σ is the effective surface tension of the primary particles, which is usually assumed to be comparable to the bulk surface tension.^{4,7} In this study, we used the same solute species (aluminum, sulfate, and nitrate ions) for all synthetic conditions and reacted the solutions during a constant time and at the same temperature.

The variables a and D were the same for all synthetic conditions because the variables are related to the solute species and the same solute species were used for all synthetic conditions. Also, t and T were also the same for all the synthetic conditions because the reaction time and temperature of the solutions were constant. Because the solute species and the synthesis method were the same, the composition of the primary particles was thought to be the same for all synthetic conditions, which means that the bulk type of the primary particles was also the same. σ is usually assumed to be comparable to the bulk surface tension,^{4,7} so σ was thought to be also almost the same for all tested conditions. Therefore, only the concentration of the solute species was changed as R values of the reactant solutions were changed. Y. Wei *et al.* reported that the particle size was altered as the concentration of the sulfate ion was changed, while the concentration of the cation was constant during the forced hydrolysis reaction.^{4,8} In

this study, the concentrations of the sulfate and nitrate ions changed as the ratio of sulfate and nitrate ions changed and this resulted in a change in particle size of the aluminum hydrous oxide.

In the previous study about the hydrolysis of aluminum nitrate with urea (NU-hydrolysis) and aluminum sulfate with urea (SU-hydrolysis), the most important point observed was that NU-hydrolysis resulted initially in a sudden formation of voluminous gelatinous precipitate, while SU-hydrolysis produced compact granular precipitate. For NU-hydrolysis, gelation occurred at a pH of about 6.5, while for SU-hydrolysis precipitate formation occurred at a pH of about 4.2. These pH values are found to be characteristic of the counter anion and not influenced by the reactant concentrations, unlike the kinetics of gelation or powder formation.^{4,9} Ramanathan *et al.* proposed the process of initial powder formation during NU-hydrolysis and SU-hydrolysis as follows.^{4,9} Urea decomposed into carbon dioxide and ammonia (yielding carbonate and hydroxide as ligands) in water at about 353 K and above. Since aqueous aluminum nitrate and sulphate solutions are acidic, carbon dioxide escaped the system. However, the hydroxide took part in the polymerization of the hydrolyzed aluminum bearing cationic species existing in solution and simultaneously increased the pH.

In the case of NU-hydrolysis, because of the poor coordinate bond strength of nitrate, it did not interfere in the reaction of hydroxide with the aluminium containing polymeric cation growing into the bigger and charged polymeric species via olation and oxolation involving Al-OH-Al and Al-O-Al bridges. With increasing pH, caused by the increased polymeric size and hydroxide ion concentration, gelation occurred at a pH of about 6.5. Due to widely spread and weak binding characteristics of the oxy- and hydroxy-bridges, the resultant precipitate (gel) was porous and voluminous. Prolonged refluxing at a higher pH crystallized into boehmite powders with elongated fibrillar

morphology. In the case of SU-hydrolysis due to the better coordinate bond strength of sulfate it bonded to the growing polymeric cation at a pH of about 4.2, terminating further polymerization and resulted in solute species of composition $\text{Al}_4(\text{OH})_{10}\text{SO}_4$ as reported by Brosset *et al.*^{4,10} Since this species is neutral, it formed strongly bound and compact primary particles which subsequently agglomerated resulting in granular precipitate. Moreover, the phase and morphology of the granular precipitates formed by SU-hydrolysis were amorphous and spherical, respectively and the microstructure of the granular precipitates was found to be agglomerates of individual spheres.^{4,9}

Interestingly, the result of SU-hydrolysis was agreed well with the result of this study in the phase, morphology and microstructure of the synthesized aluminum hydrous oxide. Therefore, it was thought that the synthesis of spherical aluminum hydrous oxide precursors was due to the presence of sulfate ions. To confirm the effect of sulfate ions, various size of monodispersed and spherical aluminum hydrous oxide precursors were prepared by the hydrolysis of aluminum salts containing sulfate and chloride ions in the presence of urea. Likewise the hydrolysis of aluminum sulfate and nitrate in the presence of urea, the total concentration of Al^{3+} and urea were fixed at 0.01 M and 0.1 M, respectively, and the concentration ratio of $\text{Al}_2(\text{SO}_4)_3 \cdot 16\text{H}_2\text{O}$ to $\text{AlCl}_3 \cdot 6\text{H}_2\text{O}$ (hereafter R_{Cl}) was changed. The reactant solutions were reacted in a 90 °C oil bath for 1 h and the result was compared with the result of the hydrolysis of aluminum sulfate and nitrate in the presence of urea prepared at the same condition. The typical FESEM images shown in Fig. 4.1.3 revealed that the average size of the synthesized precursors was similar when the value of R and R_{Cl} was equal (the average diameters of the synthesized precursors were 130 nm, 210 nm, 300 nm, and 385 nm, respectively, as shown in Fig. 4.1.4). Because there was no difference between using nitrate and chloride, we concluded that nitrate or chloride ions had no effect to the

average size of aluminum hydrous oxide precursor.

To investigate the relation between the change of precursor size and the concentration of sulfate ion, more forced hydrolysis reactions performed at 90 °C for 1 h with broad range of R listed in Table 4.1.2. In Fig. 4.1.5, the concentration of sulfate ions could be divided into three regions depending on the morphology and monodispersity of the synthesized aluminum hydrous oxide. Region I was that the concentration of sulfate ions was greater than 0.0105 M. In this region, the morphology and size distribution of the synthesized particles were not uniform. To synthesize monodispersed particles, the generation of solutes which eventually precipitate is controlled very carefully so that only one burst of nuclei occurs. The species contained in the particles must then continue to be formed at a rate which allows their removal by diffusion onto the existing particles so that no secondary nucleation may take place. Thus, the original nuclei grow uniformly, yielding monodispersed systems.^{4.11,4.12} In the mechanism of formation of monodispersed sulfur sol proposed by LaMer, if the initial concentrations are not dilute the rate of production of sulfur by the chemical reaction will become so rapid that the concentration of dissolved sulfur will continually exceed the concentration at which the rate of formation of nuclei ≈ 0 . As a result, non-uniform growth and a polydispersed sol is the final result in this case.^{4.12} Because the sulfate ion were abundant in this region, it was thought that the production rate of solute species of composition $\text{Al}_4(\text{OH})_{10}\text{SO}_4$ was too rapid to synthesize the monodispersed aluminum hydrous oxide. Region II was that the concentration of sulfate ions was between 0.009 M and 0.00375 M. In this region, uniform and spherical particles were synthesized. Moreover, the average diameter of the particles was decreased as the concentration of sulfate ions was decreased. Region III was that the concentration of sulfate ions was smaller than 0.0015 M. In this region, the morphology of the synthesized particles was

changed from sphere to rod shape. If there was no another counter anion without nitrate ion in the reactant solution, needle-like and fibrillar-like crystals were obtained after a hydrothermal reaction and a hydrolysis reaction, respectively.^{4,9,4.13} Because rod shape was similar to needle-like or fibrillar-like shape, it was thought that nitrate ion was more dominant than sulfate ion during the forced hydrolysis reaction in this region. These discussions were arranged in Fig. 4.1.6.

In Fig. 4.1.6, it was noteworthy that the relation between the average diameter of the synthesized particles and the concentration of sulfate ions was linear in the region II. During the homogeneous nucleation, the formation of solid results in a free energy change $\Delta G = G_2 - G_1$ where :

$$\Delta G = -V_S \Delta G_V + A_{SL} \gamma_{SL} \quad (4.1.2)$$

and

$$\Delta G_V = G_V^L - G_V^S \quad (4.1.3)$$

when γ_{SL} is the solid/liquid interfacial free energy. The excess free energy associated with the solid particle can be minimized by the correct choice of particle shape. If γ_{SL} is isotropic this is a sphere of radius r . Equation (4.1.2) then becomes

$$\Delta G_r = -\frac{4}{3}\pi r^3 \Delta G_V + 4\pi r^2 \gamma_{SL} \quad (4.1.4)$$

There is a certain radius, r^* , which is associated with a maximum excess free energy. If $r < r^*$ the system can lower its free energy by dissolution of the solid, whereas when $r > r^*$ the free energy of the system decreases if the solid grows. r^* is known as the critical nucleus size. Since $dG = 0$ when $r = r^*$ critical nucleus is effectively in equilibrium with the surrounding liquid. It can easily be shown that

$$r^* = \frac{2\gamma_{SL}}{\Delta G_V} \quad (4.1.5)$$

by differentiation of Equation (4.1.4).^{4.14}

ΔG_V was a constant if the composition of nuclei didn't change, therefore r^* was proportional to γ_{SL} . Therefore, it was thought that there was a linear relation between γ_{SL} and the concentration of sulfate ions in the region II. The average size of particles when the concentration of sulfate ions was 0.009 M deviated from the linear relation in the region II because it was thought that this experimental condition was through the boundary of region I and region II. A detailed study that investigates the relation between γ_{SL} and the concentration of sulfate ions during the forced hydrolysis reaction is currently underway.

Transformation of aluminum hydrous oxide precursor to porous α -Al₂O₃ by heat treatment

The thermal TG and DTA curves of the as-prepared aluminium hydrous oxide (sample a, R=0.33) is shown in Fig. 4.1.7. The gradual weight loss (~54.6 %) as the temperature reached ~900 °C corresponds to the removal of physisorbed water and the further release of water accompanying the phase transformation from aluminum hydrous oxide to Al₂O₃.^{4.15} It is thought that a major exothermic peak at ~870 °C in the DTA curve of Fig. 4.1.7 resulted from this phase transformation.

Fig. 4.1.8 shows XRD patterns of sample a annealed at various temperatures ranging from 900 °C to 1100 °C for 12 h. In Fig. 4.1.8(a), the as-prepared aluminum hydrous oxide spheres were amorphous. At 900 °C, crystalline γ -Al₂O₃ (JCPDS Card No. 50-0741) forms as the major phase. The γ -Al₂O₃ then changes to α -Al₂O₃ (JCPDS Card No. 46-1212) at temperatures higher than 1000 °C. There are several decomposition sequences of aluminum hydrous oxide to α -Al₂O₃, for example, boehmite (γ -AlOOH) \rightarrow γ -Al₂O₃ \rightarrow δ -Al₂O₃ \rightarrow θ -Al₂O₃ \rightarrow α -Al₂O₃.^{4.16} However, in this study, amorphous

aluminum hydrous oxide transformed to α -Al₂O₃ via only one metastable γ -Al₂O₃ phase.

Fig. 4.1.9 shows XRD patterns of the heat-treated samples with different R values that were fired at 1100 °C for 1 h. The XRD patterns of all the samples exhibited a rhombohedral α -Al₂O₃ phase. Moreover, the crystallinity of all samples was relatively good despite the short time of the heat treatment. Because of the good crystallinity, the synthesized α -Al₂O₃ nano particles are expected to maintain the excellent properties of bulk α -Al₂O₃.

Fig. 4.1.10 shows the typical FESEM images of the heat-treated samples with different values of R. The images clearly suggest that the original spherical morphology of aluminum hydrous oxide was preserved after the annealing process, and the corresponding diameters of each sample were 125, 195, 320, and 430 nm, respectively. Moreover, it is noteworthy that there was no necking between the α -Al₂O₃ nanoparticles, despite the precursor being fired at a relatively high temperature. Therefore, the synthesized α -Al₂O₃ nanoparticles would be expected to have good dispersion characteristics in suspension, and this advantage would be helpful when the synthesized α -Al₂O₃ nanoparticles are used in various applications.

The corresponding TEM image of sample a (R=0.33) annealed in air at 1100 °C for 1 h confirmed that the individual spheres had spherical and porous structures, as shown in Fig. 4.1.11(a). Likewise, in the FESEM image, there was no necking between the particles. The HRTEM image and selected area electron diffraction (SAED) patterns in Fig. 4.1.11(b) and (c) show that the sphere had good crystallinity despite its porous structure, which agreed well with the XRD pattern in Fig. 4.1.8(a).

The porous nature of the α -Al₂O₃ nanoparticles observed by FESEM and TEM were further elucidated by N₂ adsorption–desorption isotherms of sample a (R=0.33) before

and after heat treatment in air (Fig. 4.1.12). As described above, phase-pure γ -Al₂O₃ and α -Al₂O₃ were obtained after annealing at 900 °C and 1100 °C for 1 h, respectively. BET surface areas were estimated to be 25, 102, and 76 m²/g for as-prepared aluminum hydrous oxide, γ -Al₂O₃, and α -Al₂O₃, respectively. Although the as-prepared amorphous aluminum hydrous oxide had a relatively small surface area, the surface area of the crystalline γ -Al₂O₃ became much larger after calcination at 900 °C. During the calcination process, the as-prepared aluminum hydrous oxide are prone to decomposition. This oxidative decomposition is nearly complete around 900 °C, corresponding to a total weight loss of 54.6 %, as shown in Fig. 4.1.7. Thus, it can be understood that larger surface area of γ -Al₂O₃ is originated from volume contraction during thermal decomposition of aluminum hydrous oxide. A similar highly porous structure with large surface area has been also observed in Co₃O₄ nano-needles transformed from Co(OH)₂ accompanying large volume contraction and crystal reconstruction.^{4,17}

For α -Al₂O₃ obtained after further thermal annealing at 1100 °C, the corresponding surface area was slightly reduced, possibly due to the local shrinkage accompanying the pore elimination. Additionally, the clear hysteresis loop and the pore size distribution that was calculated using the BJH method (inset of Fig. 4.1.12) indicated the mesoporosity (2~20 nm) of both γ - and α -Al₂O₃. Thus, monodispersed porous Al₂O₃ nanospheres with a high surface area can be prepared using the thermal dehydration process of as-prepared aluminum hydrous oxide. These nanospheres can be used for a variety of catalysis, nanophosphors, separations, and promising environmental applications.^{4,18,4.19}

Table 4.1.1 R of reactant solution

| Sample | R | Total concentration of Al ³⁺ | Urea |
|--------|-------|---|------|
| A | 0.33 | 0.01M | 0.1M |
| B | 0.27 | 0.01M | 0.1M |
| C | 0.215 | 0.01M | 0.1M |
| D | 0.167 | 0.01M | 0.1M |

Table 4.1.2 The concentration of counter anion of additional reactant solution

| R | Concentration of $\text{Al}_2(\text{SO}_4)_3 \cdot 16\text{H}_2\text{O}$ | Concentration of $\text{Al}(\text{NO}_3)_3 \cdot 9\text{H}_2\text{O}$ | Urea |
|----------|---|--|-------|
| ∞ | 0.005 M | 0 M | 0.1 M |
| 4.5 | 0.0045 M | 0.001 M | 0.1 M |
| 2 | 0.004 M | 0.002 M | 0.1 M |
| 1.17 | 0.0035 M | 0.003 M | 0.1 M |
| 0.75 | 0.003 M | 0.004 M | 0.1 M |
| 0.5 | 0.0025 M | 0.005 M | 0.1 M |
| 0.33 | 0.002 M | 0.006 M | 0.1 M |
| 0.27 | 0.00175 M | 0.0065 M | 0.1 M |
| 0.215 | 0.0015 M | 0.007 M | 0.1 M |
| 0.167 | 0.00125 M | 0.0075 M | 0.1 M |
| 0.056 | 0.0005 M | 0.009 M | 0.1 M |

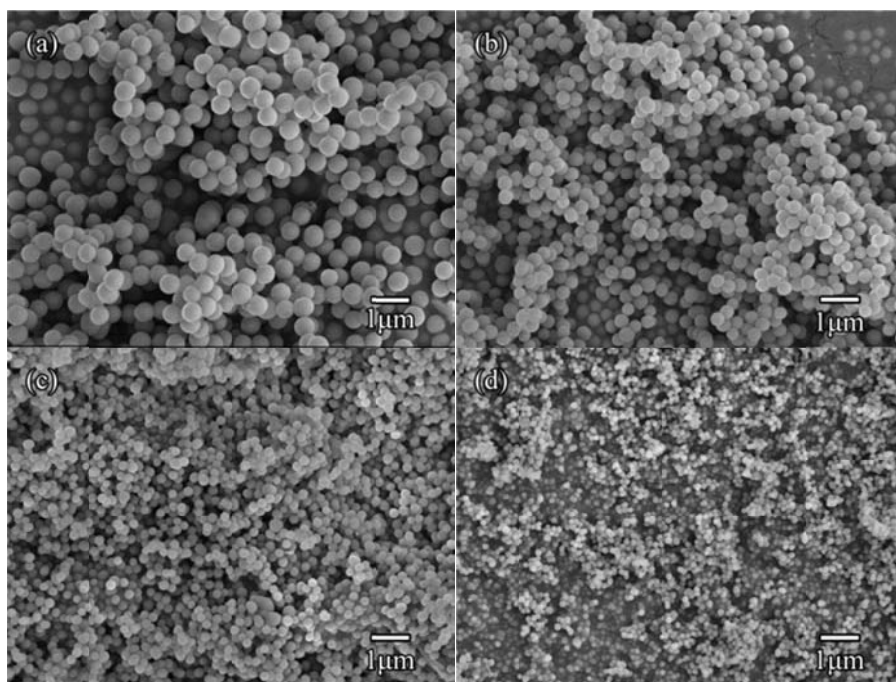


Fig. 4.1.1 FESEM images of the aluminum hydroxide precursors prepared with different values of R : (a) 0.33, (b) 0.27, (c) 0.215, and (d) 0.167.

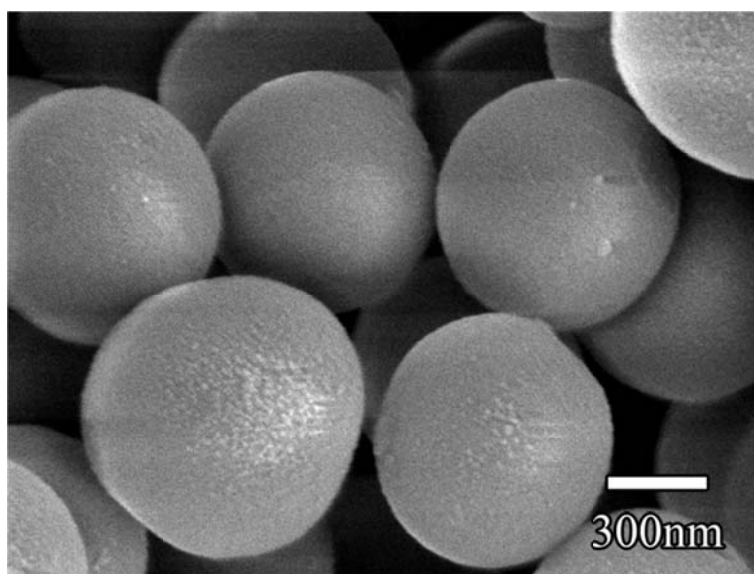


Fig. 4.1.2 Magnified FESEM image of the as-prepared aluminum hydroxide precursor ($R=0.75$).

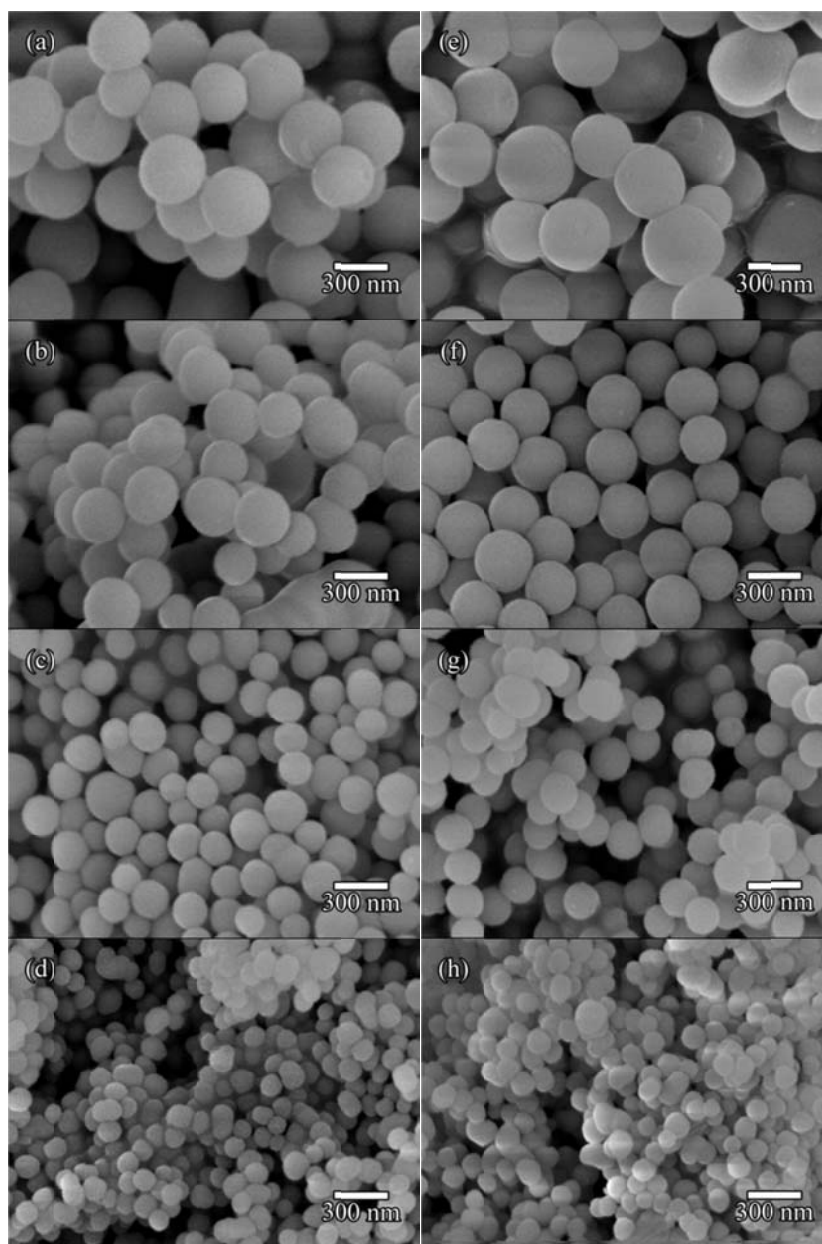


Fig. 4.1.3 FESEM images of the aluminum hydrous oxide precursors prepared at 90 °C for 1 h : (a) $R = 0.33$, (b) $R = 0.27$, (c) $R = 0.215$, (d) $R = 0.167$, (e) $R_{Cl} = 0.33$, (f) $R_{Cl} = 0.27$, (g) $R_{Cl} = 0.215$ and (h) $R_{Cl} = 0.167$.

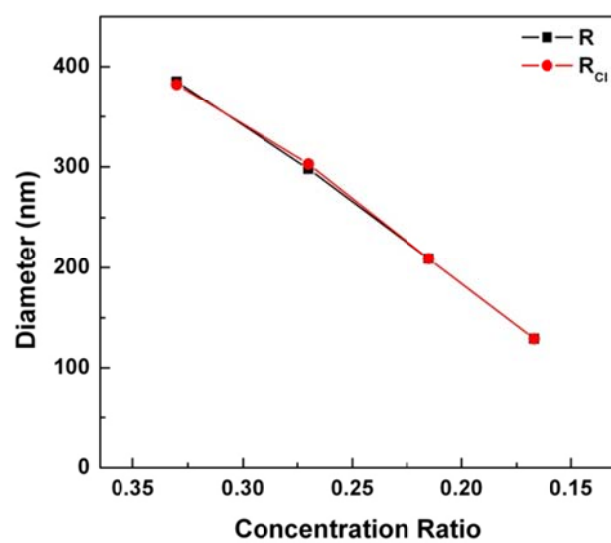


Fig. 4.1.4 The average size of the synthesized aluminum hydrous oxide precursors prepared by the different value of R and R_{Cl} .

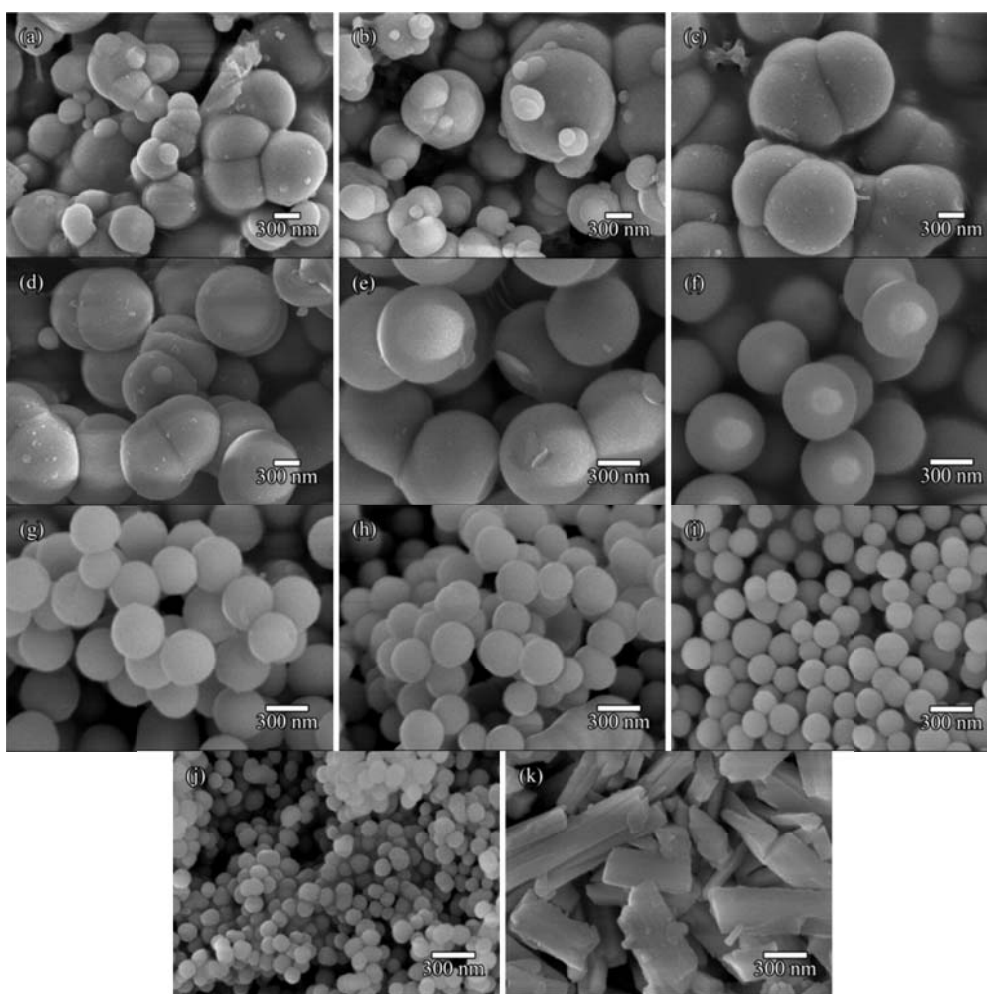


Fig. 4.1.5 FESEM images of the aluminum hydroxide precursors prepared at 90 °C for 1 h with different concentration of $[\text{SO}_4^{2-}]$: (a) 0.015 M, (b) 0.0135 M, (c) 0.012 M, (d) 0.0105 M, (e) 0.009 M, (f) 0.0075 M, (g) 0.006 M, (h) 0.00525 M, (i) 0.0045 M, (j) 0.00375 M, and (k) 0.0015 M.

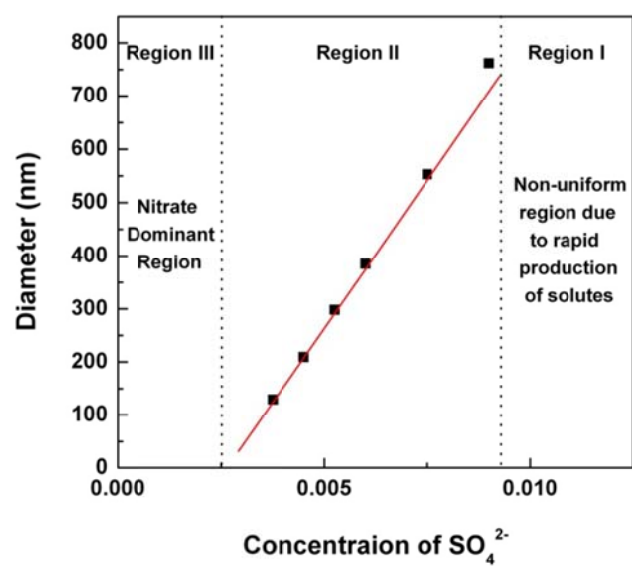


Fig. 4.1.6 The relation between the morphology and size distribution of the synthesized particles and the concentration of sulfate ions.

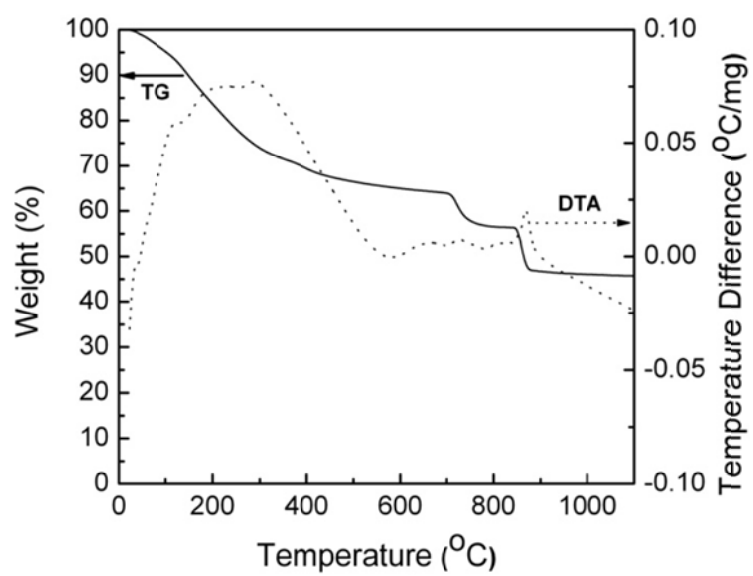


Fig. 4.1.7 TG/DTA curves of sample a (R=0.33).

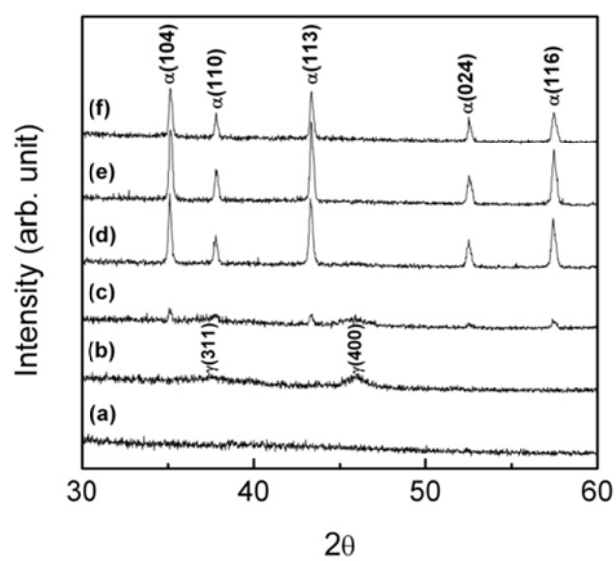


Fig. 4.1.8 XRD patterns of sample a ($R=0.33$) annealed at different temperatures for 12 h : (a) as-prepared, (b) 900 °C, (c) 950 °C, (d) 1000 °C, (e) 1050 °C, and (f) 1100 °C.

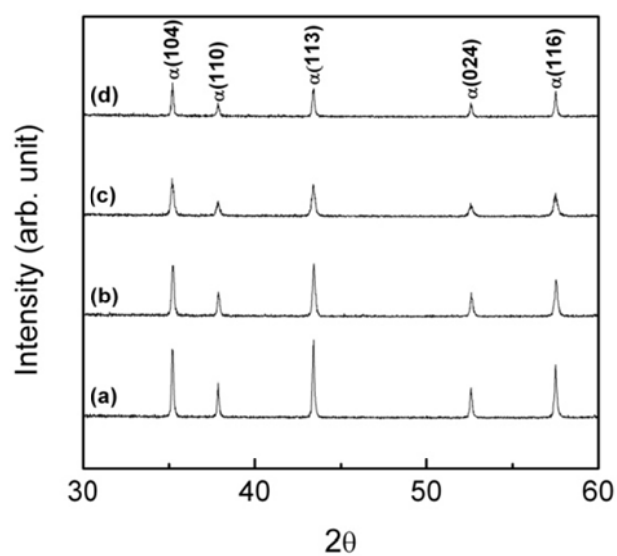


Fig. 4.1.9 XRD patterns of the samples prepared with different values of R and subsequently annealed at 1100°C for 1 h : (a) 0.33, (b) 0.27, (c) 0.215, and (d) 0.167.

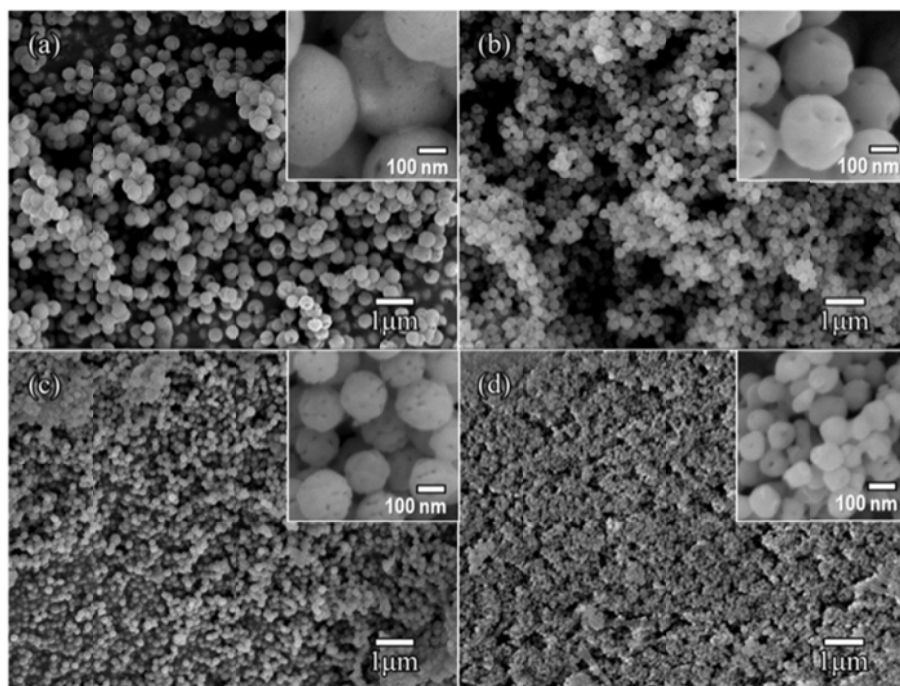


Fig. 4.1.10 FESEM images of the samples prepared with different values of R and subsequently annealed at 1100 °C for 1 h : (a) 0.33, (b) 0.27, (c) 0.215, and (d) 0.167.

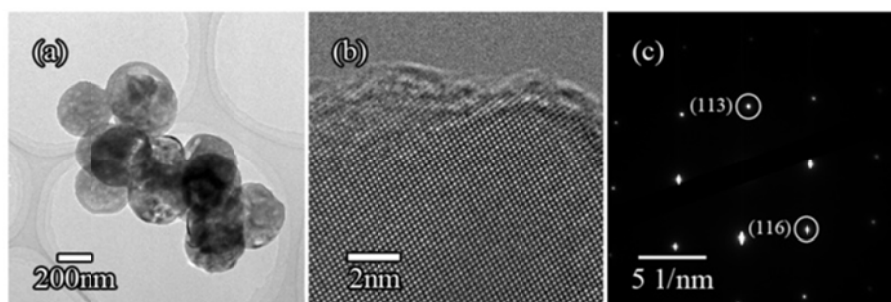


Fig. 4.1.11 TEM images of sample a ($R=0.33$) annealed in air at 1100 °C for 1 h. (a) bright-field image, (b) high-resolution image, and (c) the SAED pattern.

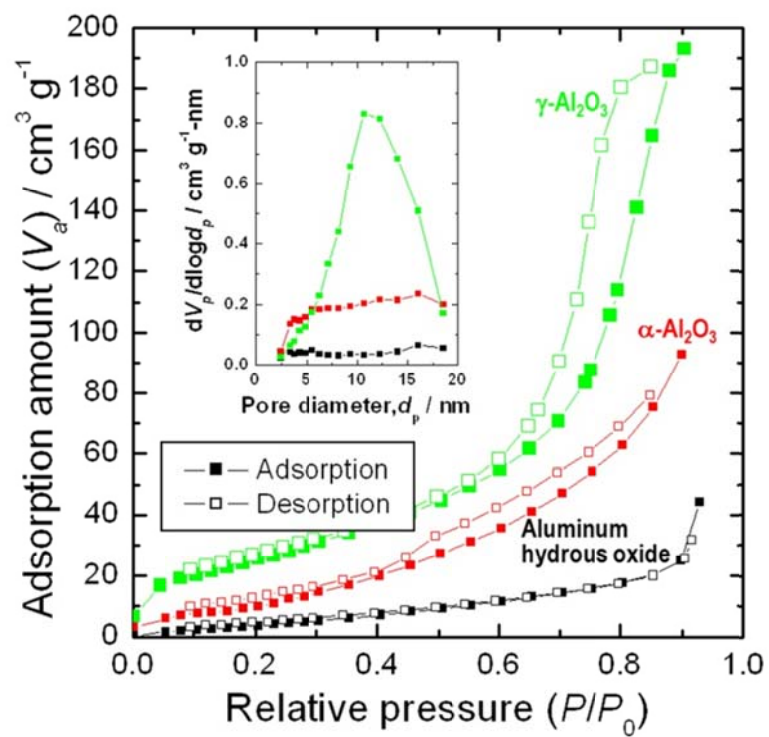


Fig. 4.1.12 Nitrogen adsorption–desorption isotherms along with the corresponding pore size distributions (inset) of sample a ($R=0.33$) before and after heat treatment in air.

4.2 Synthesis of monodispersed $\text{Y}_3\text{Al}_5\text{O}_{12}:\text{Ce}^{3+}$ nanosphere phosphor

Faint precipitates were observed in the reacted solution after 42 min of reaction. The precursors were prepared by additional reaction for 2, 4, 6, 8 and 10 min after the precipitates were observed. The typical FESEM images shown in Fig. 4.2.1 revealed that all precursors prepared with different reaction times consisted of uniformly sized nanospheres. In a previous report about the precipitation of aluminum and yttrium salts in the presence of urea, the dispersions were acidic during the early stages of the solid-phase formation and the positively charged generated particles were readily destabilized by the sulfate ion. The generated sols were stable without stabilizing agent at $\text{pH} < 6.0$ and monodispersed spherical precursors were formed only over the final pH of the reacted solution range from 4.5-5.9. The completion of the reaction after a certain time caused the saturation of particle size.^{4,20} In Fig. 4.2.1, the size of the precursors was not noticeably affected by the reaction time. Because the reaction time of the samples did not vary significantly, we considered that all of the experimental sample reaction times were close to the time at which the size of the precursors became saturated.

All the precursors had an amorphous phase. In order to transform these amorphous precursors to crystalline YAG:Ce, each precursor was annealed in air at various temperatures ranging from 900 °C to 1125 °C for 6 h. As shown in Fig. 4.2.2, several byproducts such as $\text{Y}_4\text{Al}_2\text{O}_9$, YAlO_3 , and $\alpha\text{-Al}_2\text{O}_3$ were formed before the complete formation of YAG phase. More importantly, the calcination temperatures of the precursors were systematically decreased with increasing reaction time. Fig. 4.2.3 shows XRD patterns of the samples annealed at the temperature at which each sample was transformed to phase-pure YAG. In Fig. 4.2.3, all samples were transformed to

phase pure YAG (JCPDS Card No. 33-0040) except R44-1125, in which YAlO_3 (JCPDS Card No. 74-1334) and $\alpha\text{-Al}_2\text{O}_3$ (JCPDS Card No. 46-1212) were still observed as secondary phases.

Fig. 4.2.4 shows the typical FESEM images of the YAG powders calcined at the preset temperatures indicated in Fig. 4.2.3. The growth of individual particles was negligible but necking tended to occur between the particles and this tendency was significantly increased with increasing reaction time. Interestingly, extremely severe necking occurred between the particles in R52-975 after annealing even at the lowest temperature of 975 °C, as shown in Fig. 4.2.4(f). On the contrary, there was negligible necking between the particles in R46-1075 with phase-pure YAG structure (Fig. 4.2.4(b)). Moreover, the original spherical morphology and mean particle size of the as-prepared precursor was preserved after the annealing process. The particle size distribution evaluated by the DLS method showed that the average diameters and standard deviation of the synthesized YAG:Ce were 32.4 nm and ± 8.8 nm, respectively, after annealing, as shown in Fig. 4.2.4(c). Therefore, monodispersed and stand-alone YAG:Ce nanospheres were synthesized successfully.

To elucidate the tendency of necking between particles, all samples prepared with different reaction times were subsequently annealed at a high temperature of 1300 °C for 6 h and their XRD patterns are shown in Fig. 4.2.5. The major second phase was $\alpha\text{-Al}_2\text{O}_3$, except a CeO_2 phase that was induced by doping when the reaction time for the formation of precursor was less than 50 min. The ratio of secondary phase $\alpha\text{-Al}_2\text{O}_3$ (integrated intensity at 43.39°) to major phase YAG (integrated intensity at 33.35°) was decreased as the reaction time was increased to 50 min, indicating that the quantity ratio of yttrium to aluminum was increased with increasing reaction time. Hsu *et al.* reported that the composition of precursors prepared by precipitated aluminum and

yttrium salts with urea was greatly disproportionate in favor of aluminum with respect to the original ratio, in solution, of $[Al^{3+}] / [Y^{3+}] = 3$; at the early stages of precipitation this ratio in precipitated precursor was as high as 500.^{4,20} In the hydrolysis compounds of mixed composition, the ratio of the metal content of precipitated solids depends on the hydrolysis and solute complexation properties of the cations, which are affected by the pH, anions, temperature, and aging time. Generally, in aqueous solutions, small and highly charged cations are more reactive and therefore precipitate firstly.^{4,21-4,23} In this study, the aluminum ions were considerably smaller than the yttrium ions, despite the same charge, and were preferentially hydrolyzed. Therefore, the samples that reacted insufficiently to satisfy the stoichiometric ratio of YAG (in this study R44, R46 and R48) had an excess of aluminum over the stoichiometric ratio of YAG. In Fig. 4.2.3, R44-1125 contained $\alpha-Al_2O_3$ but R46-1075 and R48-1025 did not. Therefore, the excess aluminum oxide was expected to form an amorphous phase in R46-1075 and R48-1025.

TEM analysis was conducted to investigate the relationship between necking and excess aluminum, the presence of which appeared to inhibit necking. The corresponding TEM images of R46-1075 and R50-975 are shown in Fig. 4.2.6. In Fig. 4.2.6(a), the morphology and average size of R46-1075 were a spherical shape with a smooth surface and diameter of around 65 nm, respectively. Similarly, the FESEM image did not exhibit any significant necking between the particles, indicating that stand-alone YAG:Ce nanospheres were synthesized successfully. However, Fig. 4.2.6(c) showed severe necking between the particles in the R50-975 sample. The interior of each particle in both samples exhibited a highly crystalline YAG structure, as shown in the HRTEM images and corresponding FFT patterns (Fig. 4.2.6(b) and (d)). More importantly, R46-1075 exhibited an amorphous surface layer with a thickness of a few

nanometers while R50-975 had relatively good surface crystallinity, as shown in Fig. 4.2.6(b) and 4.2.6(d), respectively. These results revealed the presence of an amorphous aluminum oxide layer on the surface of R46-1075.

Various modes of EDS analysis were conducted to clarify the existence of the amorphous aluminum oxide layer. Fig. 4.2.7 showed the results of line-mode EDS analysis of R46-1075 and R50-975. The results clearly showed the different distribution of aluminium and yttrium between R46-1075 and R50-975. While aluminum and yttrium coexisted from the surface to the interior of the particles in R50-975, only aluminum was detected on the surface of R46-1075 and the yttrium content increased towards the center. The presence of excess aluminum on the surface of R46-1075 was confirmed by further EDS analysis. Point- and area-mode EDS analyses were carried out at the point marked in Fig. 4.2.8(a) and 4.2.8(c) and in the area marked in Fig. 4.2.8(b) and (d), respectively, and the results were shown in Table 4.2.1. Similar to the line-mode EDS analysis, the results of point-mode EDS analysis revealed a uniform composition ratio of aluminum and yttrium throughout the R50-975 particles, but an excess of aluminum on the surface in R46-1075. The composition ratio of aluminum and yttrium at the center of R46-1075 ($Y : Al = 3 : 5.17$) was almost the same as the stoichiometric ratio of YAG, which implied that the core-shell structure with a YAG core and amorphous aluminum oxide layer shell formed after the annealing of R46-1075. Moreover, elemental mapping by EDS analysis also indicated the formation of core/shell particles in R46-1075, as presented in Fig. 4.2.9. These results suggested that the amorphous aluminum oxide layer on the surface of the particles in R46-1075 powders prevented the growth of YAG:Ce by acting as a barrier to prevent spontaneous self-organization of adjacent particles. As a result, monodispersed and stand-alone YAG:Ce nanospheres were synthesized successfully.

The excitation and emission spectra of R46-1075 and R50-975, measured on the luminescence spectrometer, were similar. Three Ce^{3+} absorption bands appeared in the excitation spectrum with peaks at 220, 340 and 455 nm. The band at 220 nm was very weak because the upper 5d states of Ce^{3+} in YAG have energies within the conduction band of the host, so that the excitation in these levels results mainly in quenching.^{4.24} The 5d level of Ce^{3+} populated by the transition occurring at 340 nm is just below the YAG conduction band and will also be partially quenched at room temperature.^{4.24} The most intense band peak at 450 nm was associated with the $4f \rightarrow 5d$ ($^2A_{1g}$) transitions of Ce^{3+} .^{4.25} The emission band of the synthesized YAG:Ce was located between 500 and 700 nm and peaked at 536 nm. The maximum emission intensity of R46-1075 was 2.5 times higher than that of R50-975. Generally, the emission intensity of a phosphor is mainly affected by two kinds of factor: intrinsic (doping concentration, crystallization degree and crystal structure, etc.) and extrinsic (morphology, size and surface property, etc.).^{4.26-4.31} FESEM and TEM analyses showed that both R46-1075 and R50-975 particles had a smooth surface but the latter were larger than the former due to necking. However, because the excitation and emission bands of phosphor are strengthened with increasing particle size, mainly due to the reduction of surface area^{4.29}, the extrinsic factors in R46-1075 and R50-975 were considered negligible. Furthermore, the intrinsic factors such as crystal structure, stress/strain in the YAG lattice, and degree of crystallization were not critical factors in the difference between R46-1075 and R50-975, as shown in the XRD analysis (Fig. 4.2.3). Since the Ce^{3+} concentration could not be measured due to the small concentrations in our EDS analysis, we performed another quantitative analysis by using ICP-MS to investigate the molar ratio of Ce to (Y + Ce) ($R_{[\text{Ce}]/[\text{Y}+\text{Ce}]}$) and the results were shown in table 4.2.2. The $R_{[\text{Ce}]/[\text{Y}+\text{Ce}]}$ of R46-1075 and R50-975 was 0.031 and 0.044, respectively. In the previous studies, the

highest QE of YAG:Ce nano particles was obtained at a Ce^{3+} concentration of 1%.^{4.32,4.33} Therefore, it was thought that the difference in the maximum emission intensity was attributed to the concentration quenching effect of the Ce^{3+} ion.

Table 4.2.3 lists the absorption, external quantum and QE of YAG commercial powder and R46-1075 excited at 450 nm. Generally, the QE of a luminescent material is defined as the ratio of the number of photons emitted to the number of photons absorbed.^{4.34} On this basis, the QE of YAG commercial powder and R46-1075 was 96.62% and 33.74%, respectively. The value of R46-1075 was smaller than the previously reported QE of 60%; however, the emission intensity of R46-1075 had decreased by only 13% after 18 h of irradiation time, as shown in Fig. 4.2.11. In the previous study, the emission intensity of the YAG:Ce nanophosphor was decreased by 40% after 10 min of irradiation time.^{4.35} Therefore, it was thought that the photostability of R46-1075 was relatively good. The low photostability of the YAG:Ce nanoparticles was due to the photo-oxidation reaction of Ce^{3+} to Ce^{4+} .^{4.36} In the previous studies, the photoluminescence intensity of YAG:Ce phosphor coated with Al_2O_3 decreased slightly, however, the maintenance of the coated phosphor, such as thermal stability and resistance on light decay, was increased due to the surface modification of the YAG:Ce phosphor by Al_2O_3 coating.^{4.37,4.38} In addition, a passivating alumina layer on the YAG surface could prevent diffusion of Ce^{3+} to the surface or oxidation of Ce^{3+} which resulted in the increased QE of YAG:Ce nano phosphor.^{4.33} Therefore, the photostability of R46-1075 was increased as the amorphous aluminum oxide layer on the surface reduced the content of Ce^{3+} ions near the surface of the particles and Ce^{3+} ions were less sensitive to oxidation processes. More research about the optimum concentration of Ce^{3+} , optimum thickness of the amorphous aluminum oxide layer and heat treatment condition (temperature, atmosphere and time,

etc.) is needed to increase the QE of the YAG:Ce nanospheres with an amorphous aluminum oxide layer.

Table 4.2.1 The result of point- and area-mode EDS analysis of R46-1075 and R50-975.

| Name | Y (Wt.%) | Al (Wt.%) | Y (At.%) | Al (At.%) |
|--------|----------|-----------|----------|-----------|
| Point1 | 61.000 | 38.999 | 32.189 | 67.810 |
| Point2 | 65.641 | 34.358 | 36.700 | 63.299 |
| Point3 | 72.031 | 27.968 | 43.871 | 56.128 |
| Point4 | 70.788 | 29.212 | 42.377 | 57.622 |
| Area1 | 59.808 | 40.191 | 31.110 | 68.889 |
| Area2 | 66.699 | 33.300 | 37.805 | 62.194 |

Table 4.2.2 The result of ICP-MS analysis of R46-1075 and R50-975.

| Sample | Yttrium (mg/L) | Cerium (mg/L) | $R_{[Ce]/[Y+Ce]}$ |
|----------|----------------|---------------|-------------------|
| R46-1075 | 11.34 | 0.57 | 0.031 |
| R50-975 | 10.47 | 0.75 | 0.044 |

Table 4.2.3 QE of the Commercial/R46-1075 YAG excited at 450 nm.

| Sample | Absorbed Quantum (%) | External Quantum (%) | QE (%) |
|------------|----------------------|----------------------|--------|
| Commercial | 89.56 | 86.53 | 96.62 |
| R46-1075 | 51.90 | 17.51 | 33.74 |

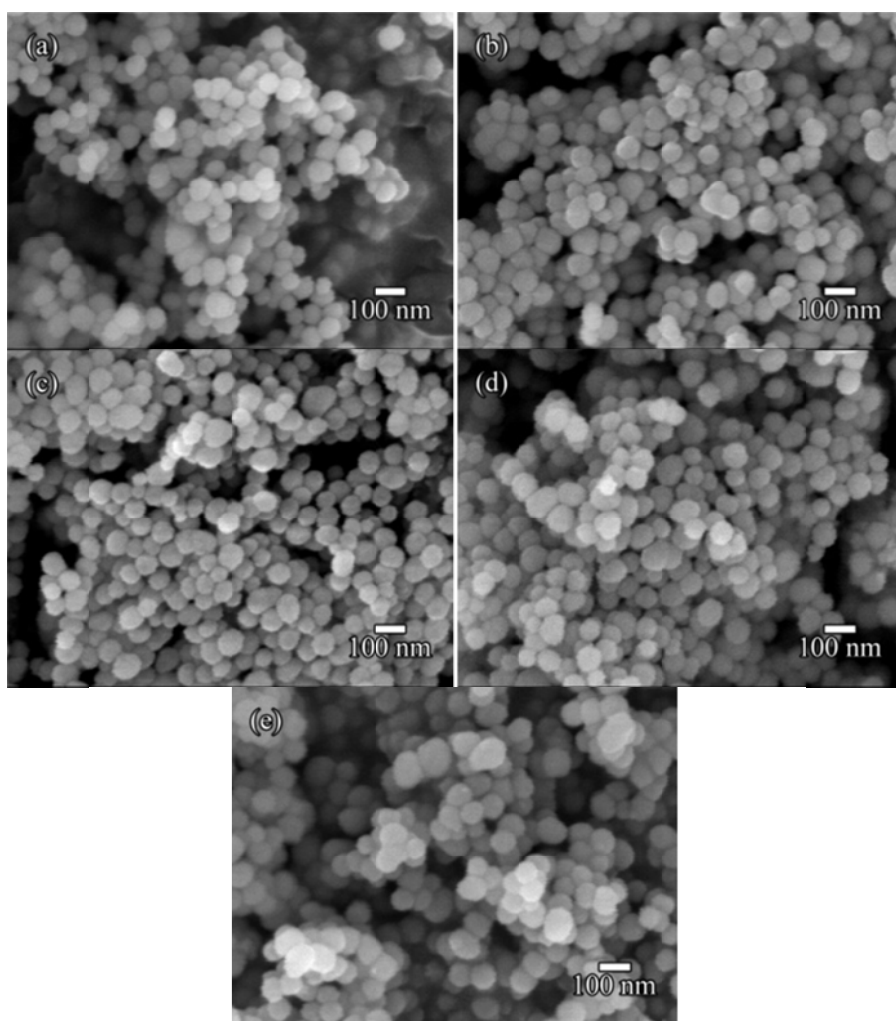


Fig. 4.2.1 SEM images of the precursors prepared with different reaction times: (a) R44, (b) R46, (c) R48, (d) R50 and (e) R52.

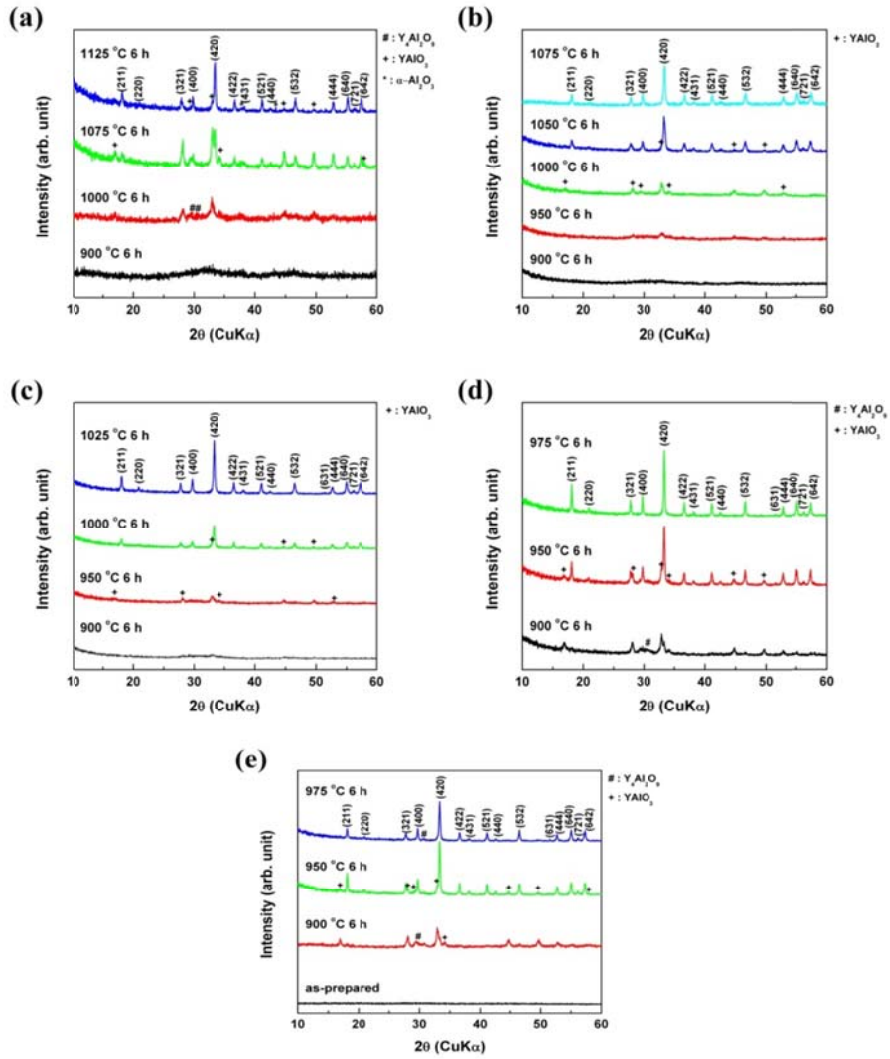


Fig.s 4.2.2 Phase evolutions of samples after subsequent heat-treatment : (a) R44, (b) R46, (c) R48, (d) R50 and (e) R52.

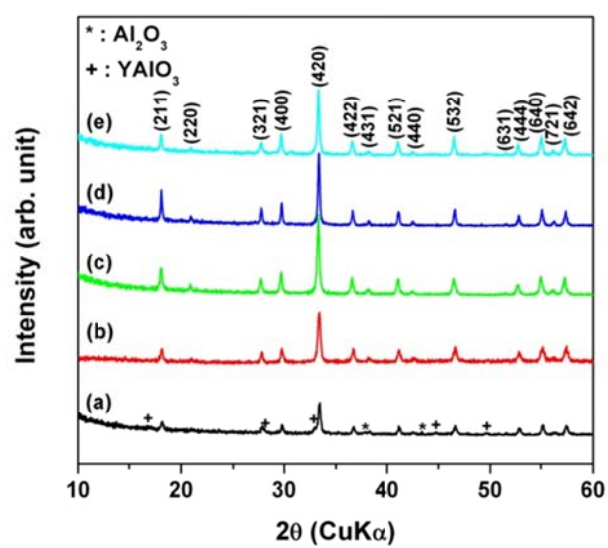


Fig. 4.2.3 XRD patterns of the samples prepared with different reaction times and subsequently annealed at different temperatures for 6 h: (a) R44-1125, (b) R46-1075, (c) R48-1025, (d) R50-975 and (e) R52-975.

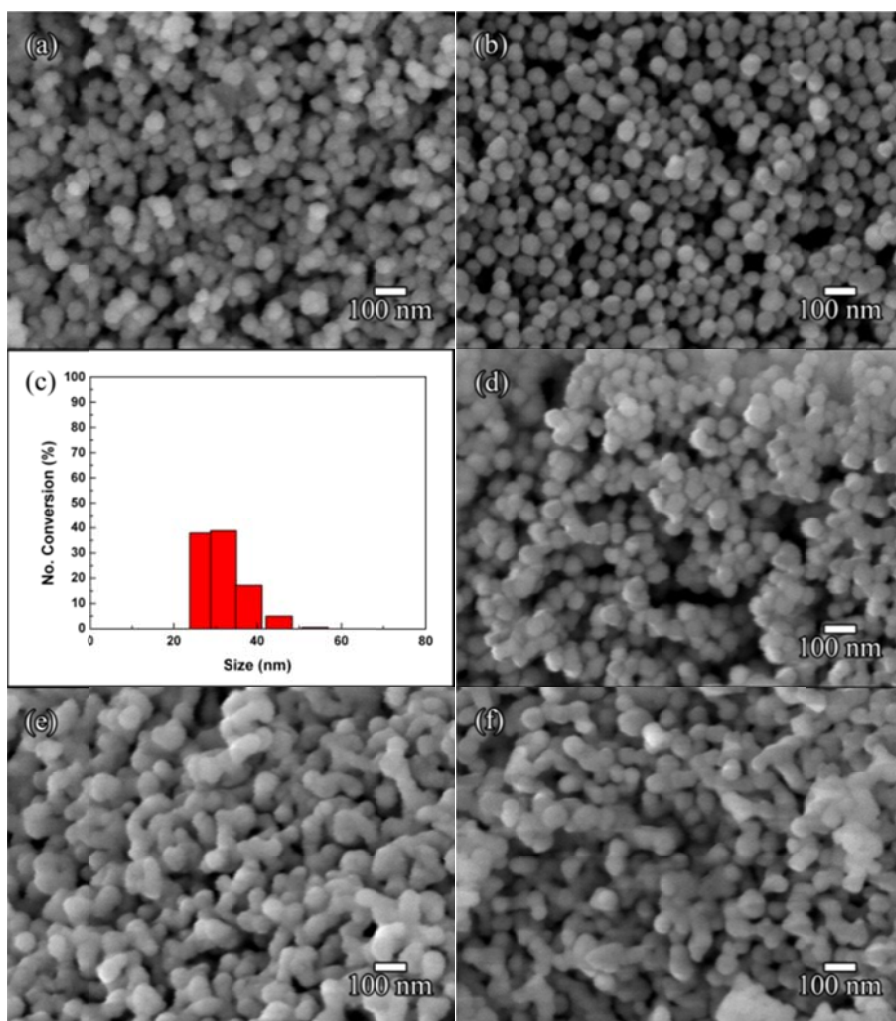


Fig. 4.2.4 SEM images of the samples prepared with different reaction times and subsequently annealed at different temperatures for 6 h: (a) R44-1125, (b) R46-1075, (c) size distribution of R46-1075, (d) R48-1025, (e) R50-975 and (f) R52-975.

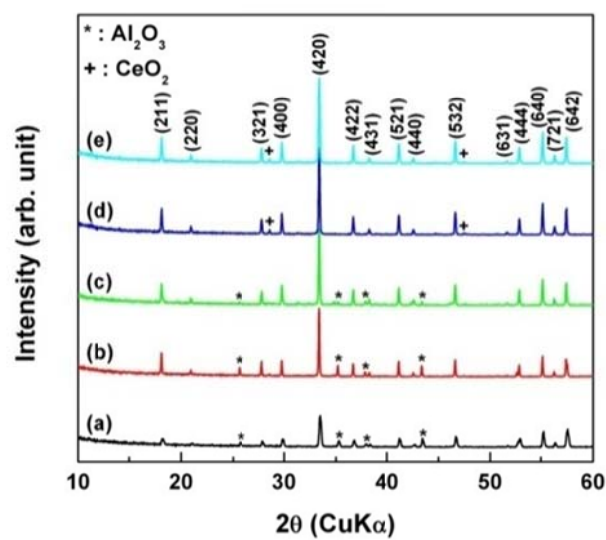


Fig. 4.2.5 XRD patterns of the samples prepared with different reaction times and subsequently annealed at 1300 °C for 6 h: (a) R44-1300, (b) R46-1300, (c) R48-1300, (d) R50-1300 and (e) R52-1300.

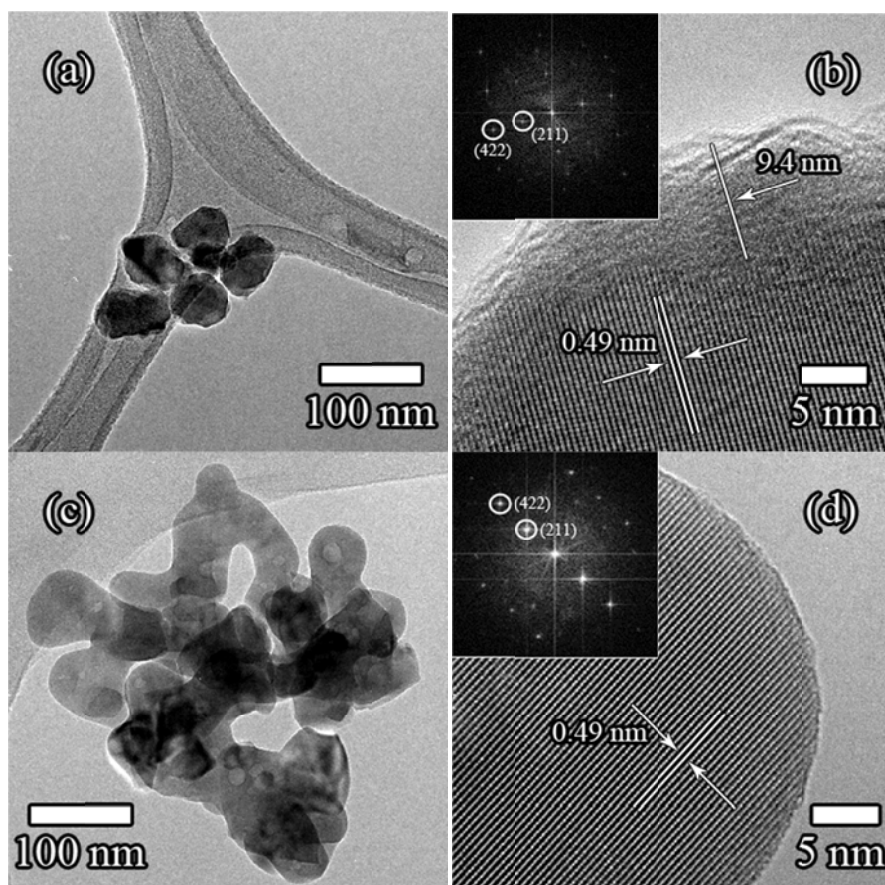


Fig 4.2.6 TEM images of the samples prepared with different reaction times and subsequently annealed at different temperatures for 6 h: (a) bright field image of R46-1075, (b) high-resolution image of R46-1075, (c) bright field image of R50-975 and (d) high-resolution image of R50-975. The insets of the high-resolution images show the Fast Fourier Transform (FFT) results.

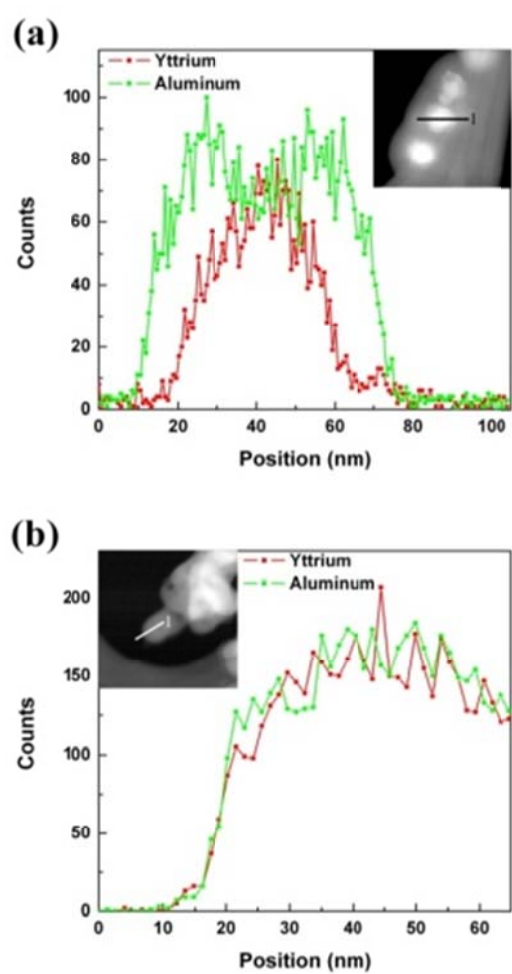


Fig 4.2.7 EDS line profiles of (a) R46-1075 and (b) R50-975.

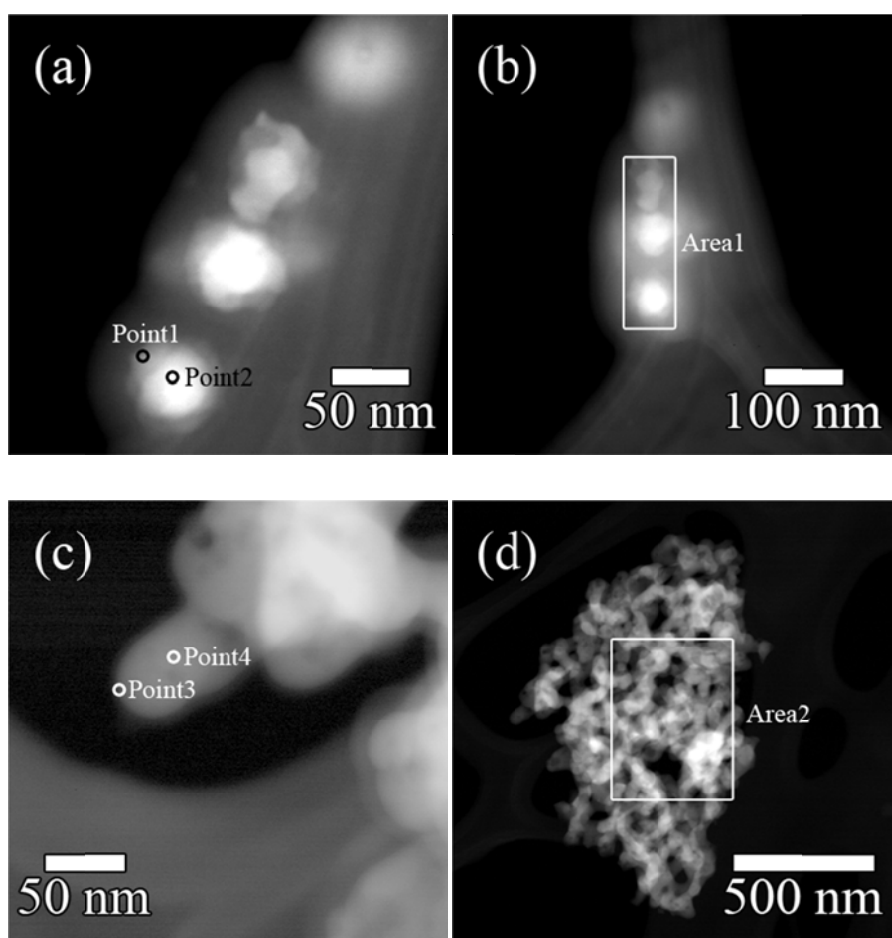


Fig. 4.2.8 EDS analysis carried out on the samples by point- and area-mode: (a) points in R46-1075, (b) area in R46-1075, (c) points in R50-975 and (b) area in R50-975.

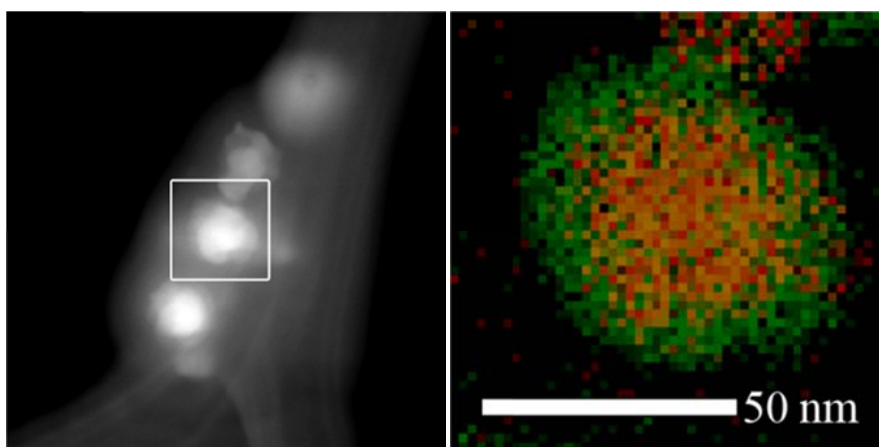


Fig. 4.2.9 Elemental mapping by EDS analysis of R46-1075 (Red : Yttrium , Green : Aluminum).

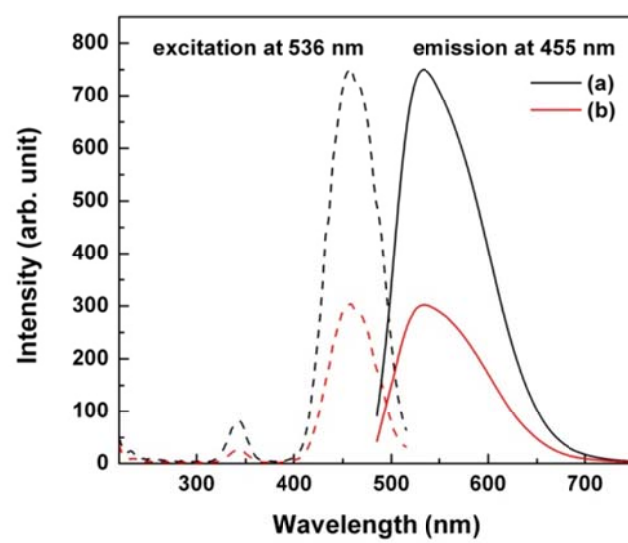


Fig. 4.2.10 PL excitation and emission spectra of (a) R46-1075 and (b) R50-975.

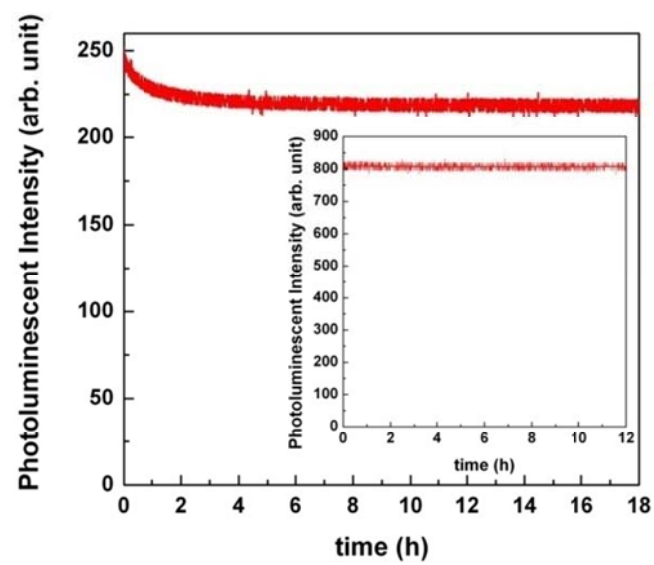


Fig. 4.2.11 Photostability of R46-1075 under blue excitation at 455 nm. The inset showed the photostability of the commercial YAG:Ce.

4.3 Synthesis of monodispersed and size-tunable BaAl₂O₄:Eu²⁺ nanosphere using γ -Al₂O₃ nanosphere as a template

Effect of reaction time on the amount of Ba²⁺ ions hydrolyzed on the γ -Al₂O₃ template

To investigate the effect of reaction time on the amount of Ba²⁺ ions hydrolyzed on the γ -Al₂O₃ template, samples were prepared by changing the reaction time using the γ -Al₂O₃ nanospheres synthesized with the concentration ratio of Al₂(SO₄)₃•16H₂O to Al(NO₃)₃•9H₂O of 0.215 as a template. The typical FESEM images shown in Fig. 4.3.1 revealed that the monodispersity and morphology of all samples prepared with different reaction times were preserved after reaction.

To elucidate the tendency of the amount of Ba²⁺ ion hydrolyzed on the γ -Al₂O₃ template, all samples prepared with different reaction times were subsequently annealed at a high temperature of 1300 °C for 5 h and their XRD patterns were shown in Fig. 4.3.2. As a reaction time was increased, the major second phase, except EuAlO₃ phase (JCPDS Card No. 30-0012) that was induced by doping and oxidizing atmosphere during heat-treatment, was changed from α -Al₂O₃ phase (JCPDS Card No. 46-1212) to Ba_{0.79}Al_{10.9}O_{17.14} phase (JCPDS Card No. 77-1522) and there was no major second phase except EuAlO₃ phase after reaction for 3 h. In the hydrolysis compounds of mixed composition, the ratio of the metal content of precipitated solids depends on the hydrolysis and solute complexation properties of the cations, which are affected by the pH, anions, temperature, and aging time. Generally, in aqueous solutions, small and highly charged cations are more reactive and therefore precipitate firstly.^{4.21-4.23} In this study, the Eu³⁺ ions were considerably smaller and highly charged than the Ba²⁺ ions.

Therefore the Eu^{3+} ions were hydrolyzed firstly in the initial stage of a forced hydrolysis reaction and the amount of the Ba^{2+} ions hydrolyzed on the $\gamma\text{-Al}_2\text{O}_3$ template was increased as the reaction time was increased. As a result, $\gamma\text{0.215-1h-1300:5h}$ and $\gamma\text{0.215-2h-1300:5h}$ had the major second phase of $\alpha\text{-Al}_2\text{O}_3$ that didn't contain the Ba^{2+} ions and $\text{Ba}_{0.79}\text{Al}_{10.9}\text{O}_{17.14}$ phase that contain insufficient amount of the Ba^{2+} ions than the stoichiometric ratio of BaAl_2O_4 , respectively.

Fig. 4.3.3 showed XRD patterns of $\gamma\text{0.215-3h}$ annealed at various temperatures ranging from 600 °C to 900 °C for 5 h. At 700 °C, crystalline BaCO_3 (JCPDS Card No. 45-1471) forms as the major phase. The BaCO_3 then transformed into BaAl_2O_4 (JCPDS Card No. 17-0306) at temperatures higher than 800 °C.

Effect of the size of template on the amount of Ba^{2+} ions hydrolyzed on the $\gamma\text{-Al}_2\text{O}_3$ template

To investigate the effect of the size of template on the amount of Ba^{2+} ions hydrolyzed on the $\gamma\text{-Al}_2\text{O}_3$ template, we synthesized the various sizes of $\gamma\text{-Al}_2\text{O}_3$ templates by changing the concentration ratio of $\text{Al}_2(\text{SO}_4)_3 \cdot 16\text{H}_2\text{O}$ to $\text{Al}(\text{NO}_3)_3 \cdot 9\text{H}_2\text{O}$. Then, precursors were synthesized by a forced hydrolysis reaction for 2 h using the different sizes of $\gamma\text{-Al}_2\text{O}_3$ nanospheres as a template. The typical FESEM images shown in Fig. 4.3.4 revealed that the monodispersity and morphology of all samples prepared using different sizes of templates were preserved after reaction and the corresponding diameters of each sample were 90, 180, and 350 nm, respectively.

XRD patterns of the samples synthesized using the different sizes of templates and annealed at a high temperature of 1300 °C for 5 h were shown in Fig. 4.3.5. The amount of Ba^{2+} ions on the template showed the clear tendency. The second phase of

γ 0.33-2h using largest γ -Al₂O₃ template was only Ba_{0.79}Al_{10.9}O_{17.14} phase except EuAlO₃ phase. As the size of γ -Al₂O₃ template was decreased, another second phase of α -Al₂O₃ phase appeared and the ratio of secondary phase α -Al₂O₃ (integrated intensity at 43.39°) to major phase BaAl₂O₄ (integrated intensity at 28.31°) was increased while Ba_{0.79}Al_{10.9}O_{17.14} phase still existed. This tendency meant that the amount of Ba²⁺ ions hydrolyzed on the γ -Al₂O₃ template was reduced as the size of the γ -Al₂O₃ template was decreased, because the amount of γ -Al₂O₃ template was fixed as 0.03 g for all experimental conditions. A detailed study that investigates the reason of above tendency is currently underway.

Photoluminescence property of the synthesized BaAl₂O₄:Eu²⁺ nanospheres

Based on the heat-treatment result of γ 0.215-3h, γ 0.215-3h was annealed in a forming gas (95 % Ar + 5 % H₂) at 900 °C for 4 h to reduce Eu³⁺ to Eu²⁺ and preserve the monodispersity and morphology of the synthesized particles. Fig. 4.3.6 showed the typical FESEM image of the γ 0.215-3h powders annealed at 900 °C for 4 h. The image clearly suggested that the original spherical morphology and monodispersity of the precursors were preserved after the annealing process, and the corresponding diameter was about 190 nm that didn't change much even after heat-treatment.

Fig. 4.3.7 showed XRD pattern of the γ 0.215-3h-900:4h and γ 0.215-3h-900:4h was transformed to phase pure BaAl₂O₄ (JCPDS Card No. 17-0306). There was no EuAlO₃ phase peak due to the reduced atmosphere during the heat-treatment.

Fig. 4.3.8 showed the PL spectra of the γ 0.215-3h-900:4h nanospheres at room temperature. The excitation and emission spectra of the γ 0.215-3h-900:4h were similar to those reported in the literature,^{4,39} *i.e.*, the maximum wavelengths of the excitation

and emission were approximately 345 nm and 495 nm, respectively. The single and symmetric emission peak was observed, which corresponds to only one Ba^{2+} site preferentially occupied by Eu^{2+} ions in the BaAl_2O_4 structure and the straightforward $4f^6 5d^1 \rightarrow 4f^7$ transition of Eu^{2+} ion.^{4,40}

In this study, monodispersed and spherical $\text{BaAl}_2\text{O}_4:\text{Eu}^{2+}$ nano phosphors were synthesized successfully. Moreover, we could control the size of the $\text{BaAl}_2\text{O}_4:\text{Eu}^{2+}$ nanospheres by changing the size of the $\gamma\text{-Al}_2\text{O}_3$ template.

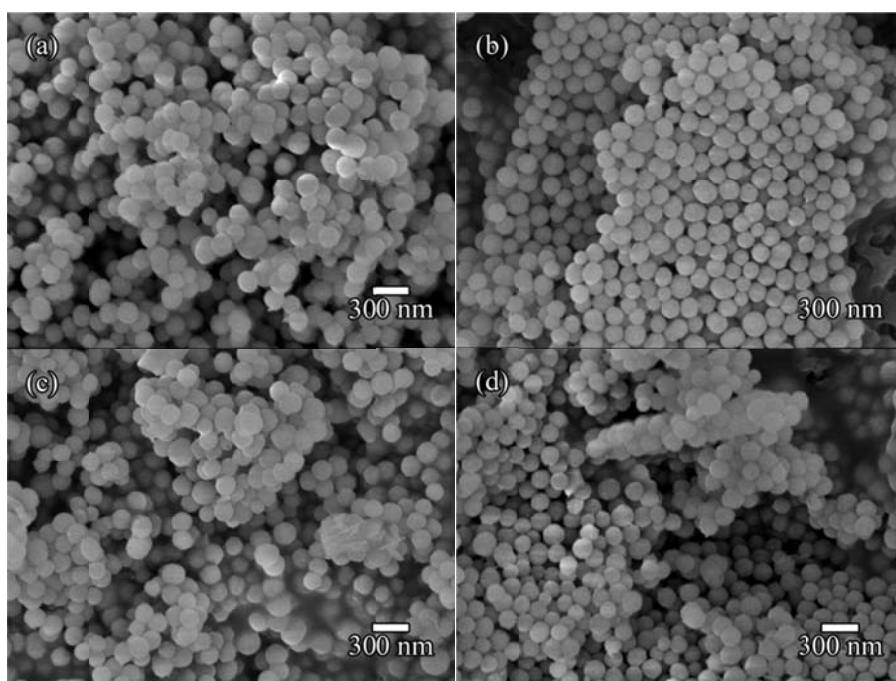


Fig. 4.3.1 SEM images of the $\gamma 0.215$ template and the samples prepared with different reaction times: (a) $\gamma 0.215$ template, (b) $\gamma 0.215$ -1h, (c) $\gamma 0.215$ -2h and (d) $\gamma 0.215$ -3h.

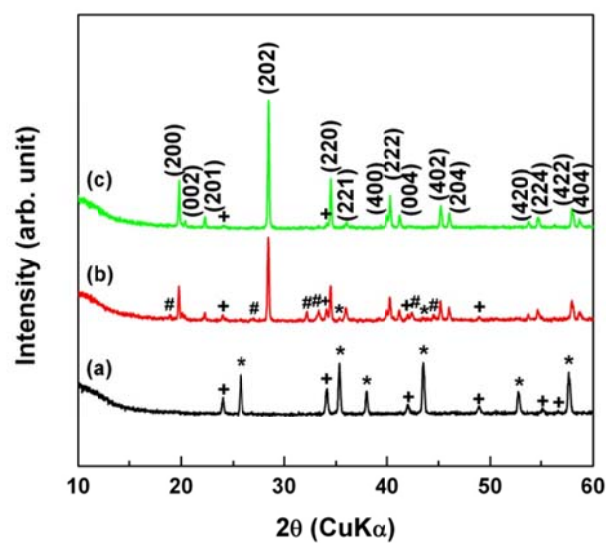


Fig. 4.3.2 XRD patterns of the samples prepared with different reaction times using γ -0.215 template and subsequently annealed at 1300 °C for 5 h: (a) γ -0.215-1h-1300:5h, (b) γ -0.215-2h-1300:5h and (c) γ -0.215-3h-1300:5h (* : α - Al_2O_3 (JCPDS No. 46-1212), + : EuAlO_3 (JCPDS No. 30-0012) and # : $\text{Ba}_{0.79}\text{Al}_{10.9}\text{O}_{17.14}$ (JCPDS No. 77-1522)).

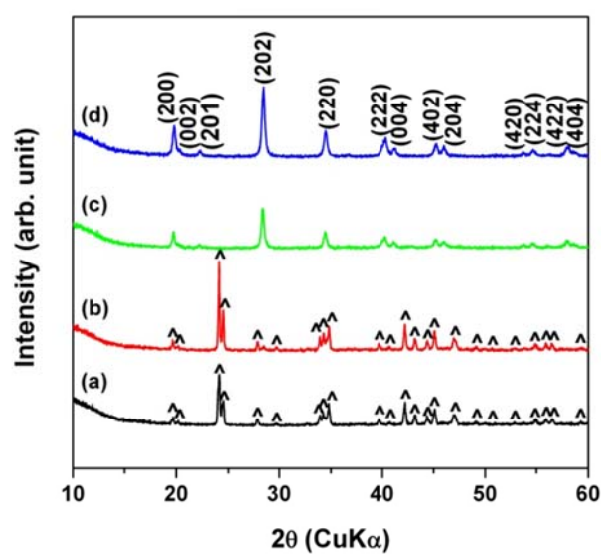


Fig. 4.3.3 XRD patterns of the samples reacted for 2 h using γ 0.215 template and subsequently annealed at various temperature for 5 h: (a) γ 0.215-2h-600:5h, (b) γ 0.215-2h-700:5h, (c) γ 0.215-2h-800:5h and (d) γ 0.215-2h-900:5h (\wedge : BaCO₃ (JCPDS No. 45-1471)).

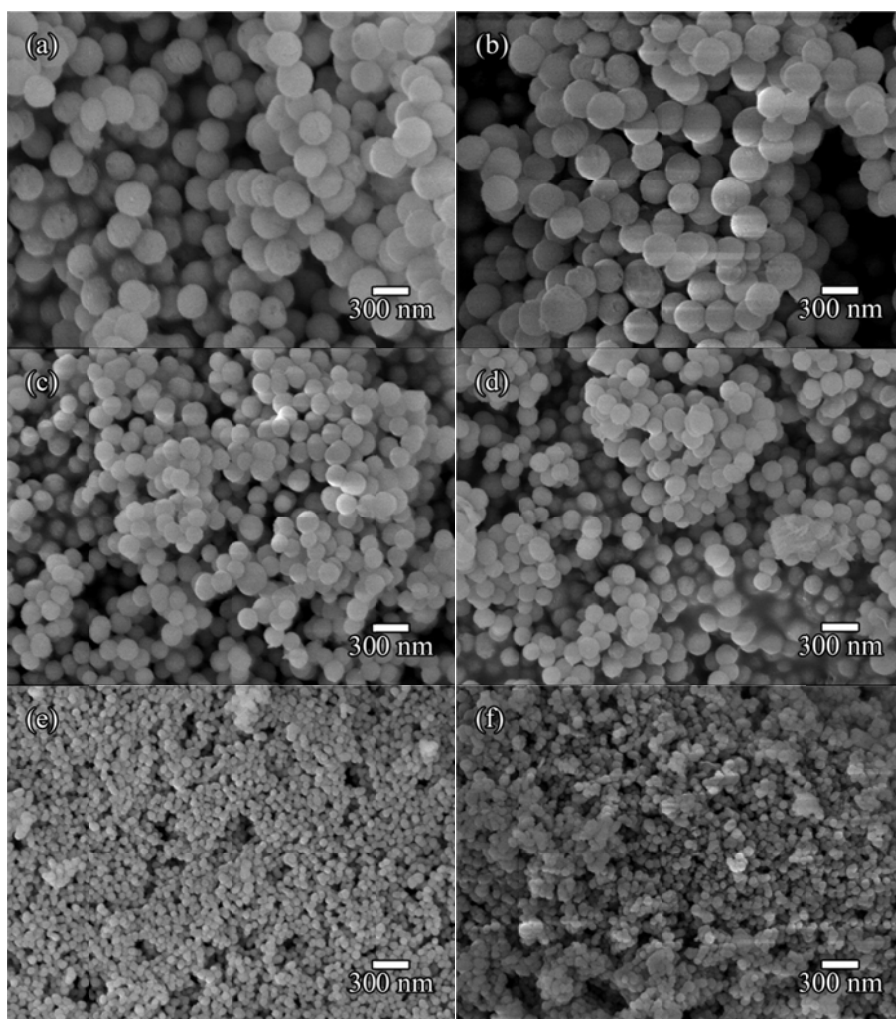


Fig. 4.3.4 SEM images of the samples prepared using γ - Al_2O_3 templates with different concentration ratio of $\text{Al}_2(\text{SO}_4)_3 \cdot 16\text{H}_2\text{O}$ to $\text{Al}(\text{NO}_3)_3 \cdot 9\text{H}_2\text{O}$: (a) $\gamma 0.33$ template, (b) $\gamma 0.33$ -2h, (c) $\gamma 0.215$ template, (d) $\gamma 0.215$ -2h, (e) $\gamma 0.125$ template and (f) $\gamma 0.125$ -2h.

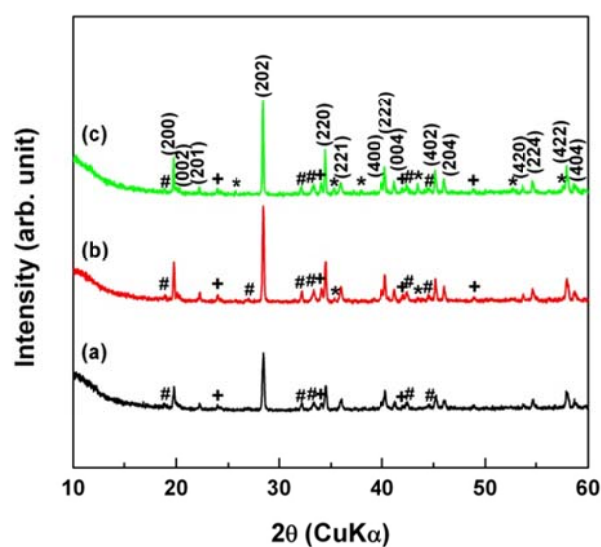


Fig. 4.3.5 XRD patterns of the samples prepared using γ -Al₂O₃ templates with different concentration ratio of Al₂(SO₄)₃•16H₂O to Al(NO₃)₃•9H₂O and subsequently annealed at 1300 °C for 5 h: (a) γ 0.33-2h-1300:5h, (b) γ 0.215-2h-1300:5h and (c) γ 0.125-2h-1300:5h (* : α -Al₂O₃ (JCPDS No. 46-1212), + : EuAlO₃ (JCPDS No. 30-0012) and # : Ba_{0.79}Al_{10.9}O_{17.14} (JCPDS No. 77-1522)).

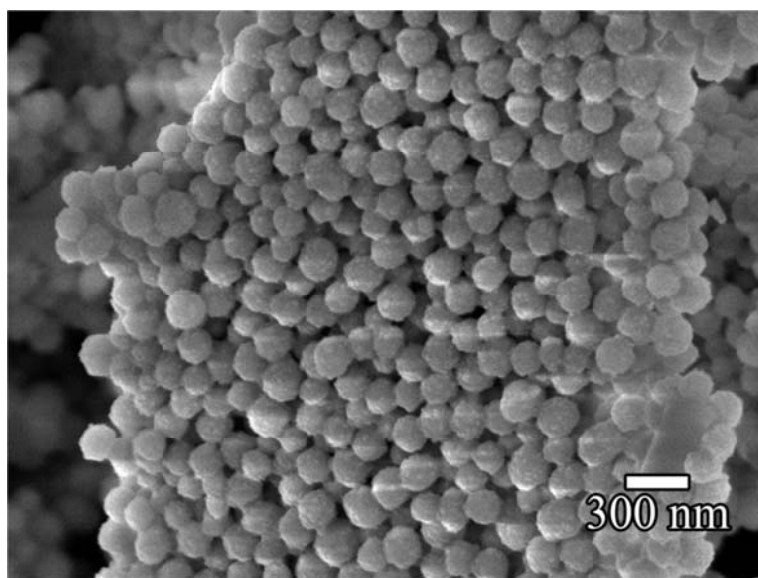


Fig. 4.3.6 SEM image of γ 0.215-3h-900:4h.

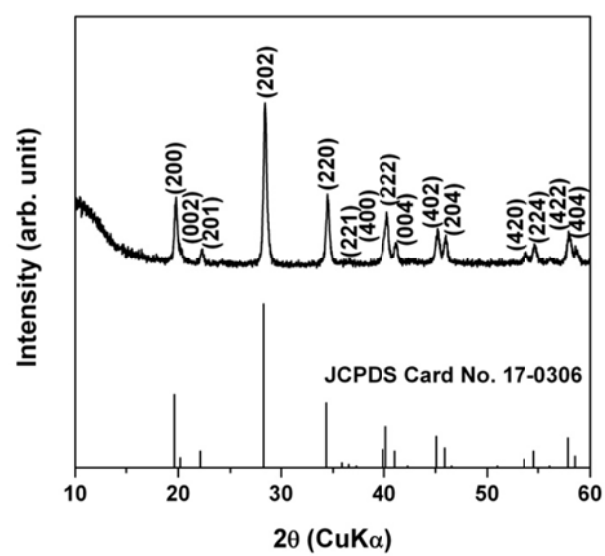


Fig. 4.3.7 XRD pattern of γ 0.215-3h-900:4h.

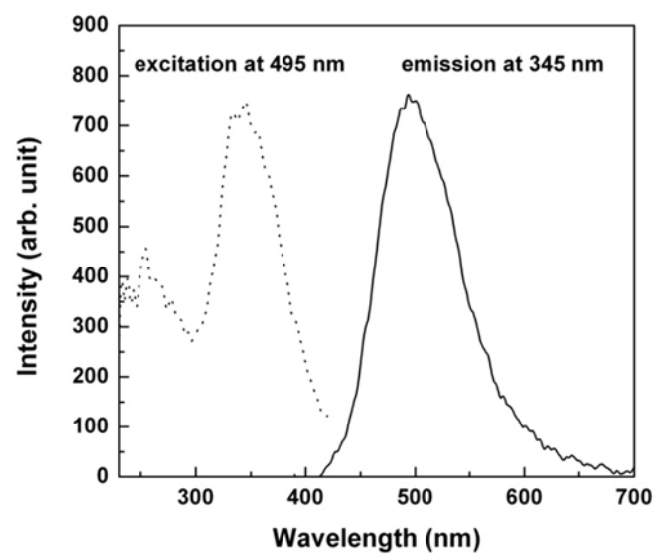


Fig. 4.3.8 PL spectra of the γ 0.215-3h-900:4h.

Chapter 5 Summary and Conclusion

We successfully synthesized monodispersed and size-tunable secondary and ternary aluminate nanospheres using a thermal annealing of amorphous precursors prepared by the facile and reproducible forced hydrolysis method.

In the synthesis of Al_2O_3 , the sizes of the monodispersed spherical aluminum hydrous oxide nanoprecursor were easily changed by controlling the ratio of sulfate to nitrate ions. As R decreased, the size of the prepared aluminum hydrous oxide precursor decreased. Phase-pure γ - and α - Al_2O_3 nanospheres with tunable sizes were obtained after annealing at 900 and 1100 °C for 1 h, respectively, preserving the original spherical shape. Furthermore, these crystalline Al_2O_3 nanospheres had large surface areas even after high temperature annealing and they exhibited a mesoporous nature due to dehydration.

In the synthesis of YAG:Ce nanophosphor, as the reaction time was increased, the ratio of yttrium to aluminum approached the stoichiometric ratio of YAG. The samples that reacted insufficiently to satisfy the stoichiometric ratio of YAG had an excess of aluminum, which formed an amorphous aluminum oxide layer on the surface of particles during subsequent heat treatment. Moreover, TEM/EDS analysis revealed that this amorphous aluminum oxide layer played an important role in preventing necking between the particles. As a result, stand-alone YAG: Ce^{3+} nanospheres with an amorphous aluminum oxide layer shell were synthesized while maintaining monodispersity with an average particle diameter of about 33 nm. These nanospheres had a dense structure and smooth surface with relatively good crystallinity after annealing at 1075 °C. They showed a single broadband emission peak at 536 nm with a luminescence QE of 33% and relatively good photostability.

Monodispersed $\text{BaAl}_2\text{O}_4:\text{Eu}^{2+}$ nanospheres were synthesized by a two-step forced hydrolysis method. The amount of Ba^{2+} ions hydrolyzed on the $\gamma\text{-Al}_2\text{O}_3$ template was increased as the reaction time was increased. Moreover, the size of the $\text{BaAl}_2\text{O}_4:\text{Eu}^{2+}$ nanospheres was controlled by changing the size of the $\gamma\text{-Al}_2\text{O}_3$ template. The amount of Ba^{2+} ions hydrolyzed on the $\gamma\text{-Al}_2\text{O}_3$ template showed a clear tendency that the amount of Ba^{2+} ions increased as the size of the $\gamma\text{-Al}_2\text{O}_3$ template was increased due to the increasing of the surface area. As a result, the precursor reacted for 3 h using $\gamma\text{-Al}_2\text{O}_3$ as a template and subsequently annealed at 900 °C for 4 h transformed into phase pure BaAl_2O_4 . The PL spectra of the synthesized $\text{BaAl}_2\text{O}_4:\text{Eu}^{2+}$ nano phosphor was similar to those of bulk $\text{BaAl}_2\text{O}_4:\text{Eu}^{2+}$, *i. e.*, the maximum wavelengths of the excitation and emission were approximately 345 nm and 495 nm, respectively.

References

- [1.1] Yen, W. M.; Shionoya, S.; Yamamoto, H. *Phosphor Handbook*; CRC Press: Boca Raton, FL, 2007.
- [1.2] Bando, K.; Sakano, K.; Noguti, Y.; Shimizu, Y. *J. Light Vis. Environ.* **1998**, 22, 2.
- [1.3] Narukawa, Y.; Nagahama, S.; Tamaki, H.; Mukai, T. *Jpn. J. Appl. Phys.* **2005**, 74, 1423.
- [1.4] Mukai, T.; Morita, D.; Nakamura, Shuji. *J. Cryst. Growth* **1998**, 189-190, 778.
- [1.5] Iwaya, M.; Terao, S.; Sano, T.; Ukai, T.; Nakamura, R.; Kamiyama, S.; Amano, H.; Akasaki, I. *J. Cryst. Growth* **2002**, 237-239, 951.
- [1.6] Nagamatsu, K.; Okada, N.; Sugimura, H.; Tsuzuki, H.; Mori, F.; Iida, K.; Bando, A.; Iwaya, M.; Kamiyama, S.; Amano, H.; Akasaki, I. *J. Cryst. Growth* **2008**, 310, 2326.
- [1.7] Grandusky, J. R.; Smart, J. A.; Mendrick, M. C.; Schowalter, L. J.; Chen, K. X.; Schubert, E. F. *J. Cryst. Growth* **2009**, 311, 2864.
- [1.8] Setlur, A. A.; Comanzo, H. A.; Srivasta, A. M.; Beers, W. W. *J. Electrochem. Soc.* **2005**, 152, H205.
- [1.9] Wang, X.; Wang, J.; Shi, J.; Su, Q.; Gong, M. *Mater. Res. Bull.* **2007**, 42, 1669.
- [1.10] Li, P.; Yang, Z.; Pang, L.; Wang, Z.; Guo, Q. *J. Rare Earths.* **2008**, 26, 44.
- [1.11] Zhao, X.; Wang, X.; Chen, B.; Meng, Q.; Di, W.; Ren, G.; Yang, Y. *J. Alloys Compd.* **2007**, 433, 352.
- [1.12] Hu, Y. S.; Zhuang, W. D.; Ye, H. Q.; Wang, D. H.; Zhang, S. S.; Huang, X. W. *J. Alloys Compd.* **2005**, 390, 226.
- [1.13] Park, J. K.; Lim, M. A.; Kim, C. H. Park, H. D. *Appl. Phys. Lett.* **2004**, 82, 683.

- [1.14] Park, J. S.; Choi, K. J.; Park, S. H.; Kim, C. H.; Kim, H. *J. Electrochem. Soc.* **2005**, *152*, H121.
- [1.15] Yamada, K.; Imai, Y.; Ishii, K. *J. Illum. Engng. Inst. Jpn.* **2002**, *86*, 308.
- [1.16] Bohren, C. F.; Huffman, D. R. *Absorption and Scattering of Light by Small Particles*; Wiley: New York, 1983, p. 132.
- [1.17] Matakai, H.; Yamaki, S.; Fukui, T. *Jpn. J. Appl. Phys.* **2004**, *43*, 5819.
- [1.18] Saito, M. *Bull. Jpn. Soc. Print. Sci. Technol.* **1999**, *36*, 50.
- [1.19] Tan, S. Y.; Yang, P. P.; Niu, N.; Gai, S. L.; Wang, J.; Jing, X. Y.; Lin, J. *J. Alloys Compd.* **2009**, *490*, 684.
- [1.20] Li, J. G.; Sun, X. D.; Ishigaki, T. *J. Phys. Chem. C* **2008**, *112*, 11707.
- [1.21] Wang, J.; Xu, Y. H.; Hojamberdiev, M. *J. Alloys Compd.* **2009**, *481*, 896.
- [1.22] Suryanarayana, C. *Inter. Mater. Rev.* **1995**, *40*, 41.
- [1.23] Komarneni, S. *J. Mater. Chem.* **1992**, *2*, 1219.
- [1.24] Gleiter, H. *Prog. Mater. Sci.* **1989**, *33*, 223.
- [1.25] Ratner, M. A.; Ratner, D. *Nanotechnology: A Gentle Introduction to the Next Big Idea*; Prentice Hall: Upper Saddle River, NJ, 2003.
- [1.26] Hao, E.; Schatz, G. C.; Hupp, J. T. *J. Fluoresc.* **2004**, *14*, 331.
- [1.27] Murphy, C. J.; Sau, T. K.; Gole, A. M.; Orendorff, C. J.; Gao, J.; Gou, L.; Hunyadi, S. E.; Li, T. *J. Phys. Chem. B* **2005**, *109*, 13857.
- [1.28] Murphy, C. J.; Coffey, J. L. *Appl. Spec.* **2002**, *56*, 16A.
- [1.29] Bunzli, J. C. G.; Piguet, C. *Chem. Soc. Rev.* **2005**, *34*, 1048.
- [1.30] Abrams, B. L.; Holloway, P. H. *Chem. Rev.* **2004**, *104*, 5783.
- [1.31] Yokota, K.; Zhang, S. X.; Kimura, K.; Sakamoto, A. *J. Lumin.* **2001**, *92*, 223.
- [1.32] Ravichandran, D.; Roy, R.; White, W. B.; Erdei, S. *J. Mater. Res.* **1997**, *12*, 819.
- [1.33] Ellens, A.; Zwaschka, F.; Kummer, F.; Meijerink, A.; Raukas, M.; Mishra, K. *J.*

Lumin. **2001**, 93, 147.

[1.34] Brace, R.; Matijević, E. *J. Inorg. Nucl. Chem.* **1973**, 35, 3691.

[1.35] Willard, H. H.; Tang, N. K. *J. Am. Chem. Soc.* **1937**, 59, 1190.

[1.36] Her, Y.-S.; Lee, S.-H.; Matijević, E. *J. Mater. Res.* **1996**, 11, 156.

[1.37] Musi, S.; Krehula, S.; Popovi, S. *Mater. Lett.* **2004**, 58, 2640.

[1.38] Wei, Y.; Wu, R.; Zhang, Y. *Mater. Lett.* **1999**, 41, 101.

[1.39] Marković, J. P.; Milonjić, S. K. *J. Serb. Chem. Soc.* **2006**, 71, 613.

[1.40] Chen, Y.; Ring, T. A. *J. Dispersion Sci. Technol.* **1998**, 19, 229.

[1.41] Hanh, N.; Quy, O. K.; Thuy, N. P.; Tung, L. D.; Spinu, L. *Physica B: Condensed Matter* **2003**, 327, 382.

[2.1] Schubert, E. F. *Light-Emitting Diodes*; Cambridge University Press, 2003.

[2.2] Akasaki, I.; Amano, H.; Kito, M.; Hiramatsu, K. *J. Lumin.* **1991**, 48-49, 666.

[2.3] Huang, H.-W.; Kao, C. C.; Chu, J. T.; Kuo, H. C.; Wang, S. C.; Yu, C. C.; Lin, C. F. *Mater. Sci. Eng., B* **2004**, 113, 19.

[2.4] Tsai, H.-C. *Microelectron. J.* **2005**, 36, 712.

[2.5] Mo, C.; Fang, W.; Pu, Y.; Liu, H.; Jiang, F. *J. Cryst. Growth* **2005**, 285, 312.

[2.6] Suihkonen, S.; Svensk, O.; Lang, T.; Lipsanen, H.; Odnoblyudov, M. A.; Bougrov, V. E. *J. Cryst. Growth* **2007**, 298, 740.

[2.7] Yu, H. J.; Park, K.; Chung, W.; Kim, J.; Kim, S. H. *Synthetic Met.* **2009**, 159, 2474.

[2.8] Nakamura, S.; Mukai, T.; Iwasa, N. US Patent Granted Numbed 5578839, 1996.

[2.9] Mori, M.; Hamamoto, A.; Takahashi, A.; Nakano, M.; Wakikawa, N.; Tachibana, S.; Ikehara, T.; Nakaya, Y.; Akutagawa, M.; Kinnouchi, Y. *Med. Biol. Eng. Comput.* **2007**, 45, 1237.

[2.10] Nakamura, S.; Fasol, G. *The Blue Laser Diode*; Springer: Berlin, 1997.

- [2.11] Zukauskas, A.; Shur, M. S.; Caska, R. *Introduction to Solid-state Lighting*; John Wiley & Sons: New York, 2002.
- [2.12] Sze, S. M. *Semiconductor Devices: Physics and Technology*; John Wiley & Sons: New York, 2002.
- [2.13] Uheda, K.; Takizawa, H.; Endo, T.; Yamane, H.; Shimada, M.; Wang, C.-M.; Mitomo, M. *J. Lumin* **2000**, 87-89, 967.
- [2.14] Hoppe, H. A.; Lutz, H.; Morys, P.; Schnick, W.; Seilmeier, A. *J. Phys. Chem. Solids* **2000**, 61, 2001.
- [2.15] Narendran, N.; Gu, Y.; Freyssonier, J. P.; Yu, H.; Deng, L. *J. Cryst. Growth* **2004**, 268, 449.
- [2.16] Yum, J.-H.; Kim, S.-S.; Sung, Y.-E. *Colloid. Surface A* **2004**, 251, 203.
- [2.17] Yang, Z.; Li, X.; Yang, Y.; Li, X. *J. Lumin.* **2007**, 122-123, 707.
- [2.18] Thornton, W. A. *J. Opt. Soc. Amer.* **1971**, 61, 1155.
- [2.19] Koedam, M.; Opstelten, J. J. *Lighting Res. Technol.* **1971**, 3, 205.
- [2.20] Kim, T.; Kang, S. *J. Lumin.* **2007**, 122-123, 964.
- [2.21] Jung, K. Y.; Kim, J. H.; Kang, Y. C. *J. Lumin.* **2009**, 129, 615.
- [2.22] Cao, F.; Tian, Y.; Chen, Y.; Xiao, L.; Wu, Q. *J. Lumin* **2009**, 129, 585.
- [2.23] Zhang, X.; Wang, X.; Huang, J.; Shi, J.; Gong, M. *Opt. Mater.* **2009**, 32, 75.
- [2.24] Hu, Y. S.; Zhuang, W. D.; Ye, H. Q.; Wang, D. H.; Zhang, S. S.; Huang, X. W. *J. Alloys Compd.* **2005**, 390, 226.
- [2.25] Park, J. K.; Lim, M. A.; Kim, C. H. Park, H. D. *Appl. Phys. Lett.* **2004**, 82, 683.
- [2.26] Park, J. S.; Choi, K. J.; Park, S. H.; Kim, C. H.; Kim, H. *J. Electrochem. Soc.* **2005**, 152, H121.
- [2.27] Bohren, C. F.; Huffman, D. R. *Absorption and Scattering of Light by Small Particles*; Wiley: New York, 1983, p. 132.

- [2.28] Furnas, C. C. *Ind. Eng. Chem.* **1931**, 23, 1052.
- [2.29] Ronda, C.; Srivastava, A. *Electrochemical Society Interface* **2006**, 15, 55.
- [2.30] Verstegen, J. M. P. J. *J. Electrochem. Soc.* **1974**, 121, 1623.
- [2.31] Blasse, G.; Grabmaier, B. C. *Luminescent Materials*; Springer-Verlag: Berlin, 1994.
- [2.32] Rond, C. R. *Luminescent Materials: From Theory to Applications*; WILEY-VCH GmbH & Co. KGaA: Weinheim, 2008.
- [2.33] Kitai, A. *Luminescent Materials and Applications*; John Wiley & Sons: Chichester, 2008.
- [2.34] Ropp, R. C. *Luminescence and the Solid State*; Elsevier: Amsterdam, 2004.
- [2.35] Gorobets, B. S.; Rogojine, A. A. *Luminescent Spectra of Minerals*; All-Russia Institute of Mineral Resources: Moscow, 2002
- [2.36] Ono, Y. A. *Electroluminescent Displays*; World Scientific: Singapore, 1995.
- [2.37] Ivey, H. F. *Electroluminescence and Related Effects*; Academic: New York, 1963.
- [2.38] Yacobi, B. G.; Holt, D. B. *Cathodoluminescence Microscopy of Inorganic Solids*; Plenum Press: New York, 1990.
- [2.39] Hordijk, W.; Blasse, G. *J. Lumin.* **1973**, 6, 137.
- [2.40] de Hair, J. T. W. *J. Lumin.* **1979**, 18-19, 797.
- [2.41] de Vries, A. J.; Blasse, G.; Pet, R. J. *Mater. Res. Bull.* **1987**, 22, 1141.
- [2.42] Stevels, A. L. N.; van der Dose De Bye, J. A. W. *J. Lumin.* **1979**, 18-19, 809.
- [2.43] Laversenne, L.; Kairouani, S.; Guyot, C.; Goutaudier, C.; Boulon, G.; Cohen-Adad, M. T. *Opt. Mater.* **2002**, 19, 59.
- [2.44] Yen, W. M.; Shionoya, S.; Yamamoto, H. *Phosphor Handbook*; CRC Press: Boca Raton, FL, 2007.
- [2.45] Curie, D. *Luminescence in Crystals*; John Wiley & Sons: London, 2008.

- [2.46] Di Bartolo, B. *Optical Interactions in Solids*; John Wiley & Sons: New York, 1968.
- [2.47] Manigault, P. A. Ph.D. Thesis, Georgia Institute of Technology, 2001.
- [2.48] Jones, T. Ph.D. Thesis, Georgia Institute of Technology, 1999.
- [2.49] Blasse, G. *Handbook on the Physics and Chemistry of Rare Earths*; North-Holland Pub.: Amsterdam, 1979.
- [2.50] Grigorov, L. S.; Kynev, K. *J. Mol. Struct.* **1984**, *115*, 115.
- [2.51] Antic-Fidancev, E.; Holsa, J.; Lastusaari, M. *J. Alloys Compd.* **2002**, *341*, 82.
- [2.52] Koubaa, T.; Dammak, M.; Kammoun, M.; Jadwisieniczak, W. M.; Lozykowski, H. J. *J. Alloys Compd.* **2010**, *496*, 56.
- [2.53] Van Uitert, L. G. *J. Lumin.* **1984**, *29*, 1.
- [2.54] Blasse, G.; Wanmaker, W. L.; Tervrugt, J. W.; Bril, A. *Philips Res. Rept.* **1968**, *23*, 189.
- [2.55] Dai, Q.; Song, H.; Wang, M.; Bai, X.; Dong, B.; Qin, R.; Qu, X.; Zhang, H. *J. Phys. Chem. C* **2008**, *112*, 19399.
- [2.56] Gan, J.; Huang, Y.; Shi, L.; Qiao, X.; Seo, H. *J. Mater. Lett.* **2009**, *63*, 2160.
- [2.57] Sharma, S. K.; Pitale, S. S.; Malik, M. M.; GunduRao, T. K.; Chawla, S.; Qureshi, M. S.; Dubey, R. N. *J. Lumin.* **2010**, *130*, 240.
- [2.58] Matijević, E. *Colloid J.* **2007**, *69*, 29.
- [2.59] LaMer, V. K. *Ind. Eng. Chem.* **1952**, *44*, 1270.
- [2.60] LaMer, V. K.; Dinegar, R. *J. Amer. Chem. Soc.* **1950**, *72*, 4847.
- [2.61] Dirksen, J. A.; King, T. A. *Chem. Eng. Sci.* **1991**, *46*, 2389.
- [2.62] Stocks, G. M.; Gonis, A. *Alloy Phase Stability*; Kluwer Academic: Boston, 1989.
- [2.63] Bail, R. C.; Julien, R. *J. Physique Lett.* **1984**, *45*, 103.

- [2.64] Sander, L. M. *Multiple Scattering of Waves in Random Media and Random Rough Surfaces*; The Pennsylvania State Univ., 1985, p. 51.
- [2.65] Privman, V.; Goia, D. V.; Park, J.; Matijevic, E. *J. Colloid Interface Sci.* **1999**, 213, 36.
- [2.66] Paglia, G. *Determination of the Structure of γ -Alumina using Empirical and First Principles Calculations Combined with Supporting Experiments*; Curtin University of Technology, 2004.
- [2.67] Wiberg, E.; Holleman, A. F. *Inorganic Chemistry*; Academic Press: Berlin; New York, 2001.
- [2.68] Geller, S. Z. *Kristallogr.* **1967**, 125, 1.
- [2.69] Hyde, B. G.; Anderson, S. *Inorganic Crystal Structures*; Wiley: New York, 1989.
- [2.70] Warshaw, I.; Roy, R. *J. Am. Ceram. Soc.* **1959**, 42, 434.
- [2.71] Nie, W.; Boulon, G.; Monteil, A. *J. Phys. (Paris)* **1989**, 50, 3309.
- [2.72] Robbins, D. J. *J. Electrochem. Soc.* **1979**, 126, 1550.
- [2.73] Zych, E.; Brecher, C.; Glodo, J. *J. Phys.: Condens. Mat.* **2000**, 12, 1947.
- [2.74] Lu, C.-H.; Hong, H.; Jagannathan, R. *J. Mater. Chem.* **2002**, 12, 2525.
- [2.75] Hörkner, V. W.; Müller-Buschbaum, H. *Z. Anorg. Allg. Chem.* **1979**, 451, 40.
- [2.76] Huang, S.; Von Der Mühl, R.; Ravez, J.; Chaminade, J.; Hagenmüller, P.; Couzi, M. *J. Solid State Chem.* **1994**, 109, 97.
- [2.77] Rodehorst, U.; Carpenter, M.; Marion, S.; Henderson, C. *Mineral. Magn.* **2003**, 67, 989.
- [2.78] Poort, S. H. M.; Blokpoel, W. P.; Blasse, G. *Chem. Mater.* **1995**, 7, 1547.
- [2.79] Nag, A.; Kutty, T. R. N. *J. Mater. Chem.* **2004**, 14, 1598.
- [2.80] You, H.; Nogami, M. *J. Phys. Chem. B* **2005**, 109, 13980.

- [4.1] Zaiser, E. M.; La Mer, V. K. *J. Colloid Interface Sci.* **1948**, 3, 571.
- [4.2] Matijević, E.; Scheiner, P. *J. Colloid Interface Sci.* **1978**, 63, 509.
- [4.3] Matijević, E.; Murphy-Wilhelmy, D. *J. Colloid Interface Sci.* **1982**, 86, 476.
- [4.4] Hsu, U. P.; Rönquist, L.; Matijević, E. *Langmuir* **1988**, 4, 31.
- [4.5] Ocană, M.; Serna, C. J.; Matijević, E. *Colloid Polymer Sci.* **1995**, 273, 681.
- [4.6] Bailey, J. K.; Brinker, C. J.; McCartney, M. L. *J. Colloid Interface Sci.* **1993**, 157, 1.
- [4.7] Privman, V.; Goia, D. V.; Park, J.; Matijević, E. *J. Colloid Interface Sci.* **1999**, 213, 36.
- [4.8] Wei, Y.; Wu, R.; Zhang, Y. *Materials Letters* **1999**, 41, 101.
- [4.9] Ramanathan, S.; Roy, S. K.; Bhat, R.; Upadhyaya, D. D.; Biswas, A. R. *Ceram. Int.* **1997**, 23, 45.
- [4.10] Brosset, C.; Biedermann, G.; Sillen, L. G. *Acta Chem. Scand.* **1954**, 8, 1917.
- [4.11] LaMer, V. K.; Dinegar, R. *J. Am. Chem. Soc.* **1950**, 72, 4847.
- [4.12] LaMer, V. K. *Ind. Eng. Chem.* **1952**, 44, 1270.
- [4.13] Cai, W.; Yu, J.; Mann, S. *Microporous Mesoporous Mater.* **2009**, 122, 42.
- [4.14] Porter, D. A.; Easterling, K. E. *Phase Transformation in Metals and Alloys*; Nelson Thornes Ltd.: Cheltenham, **2001**, 186-188.
- [4.15] Yue, M. B.; Xue, T.; Jiao, W. Q.; Wang, Y. M.; He, M.-Y. *Solid State Sciences* **2011**, 13, 409.
- [4.16] Wefers, K.; Misra, C. *Oxides and Hydroxides of aluminium*; Alcoa Technical Paper No. 19: Alcoa Laboratories, 1987.
- [4.17] Lou, X. W.; Deng, D.; Lee, J. Y.; Archer, L. A. *J. Mater. Chem.* **2008**, 18, 4397.
- [4.18] Cai, W.; Yu, J.; Cheng, B.; Su, B. L.; Jaroniec, M. *J. Phys. Chem. C* **2009**, 113, 14739.

- [4.19] Bai, P.; Wu, P.; Yan, Z.; Zhao, X. S. *J. Mater. Chem.* **2009**, 19, 1554.
- [4.20] Hsu, W. P.; Wang, G.; Matijevic, E. *Colloid Surface* **1991**, 61, 255.
- [4.21] Brace, R.; Matijevic, E. *J. Inorg. Nucl. Chem.* **1973**, 35, 3691.
- [4.22] Matijevic, E.; Janauer, G. E.; Kerker, M. J. *Colloid Interf. Sci.* **1964**, 19, 333.
- [4.23] Matijevic, E. *J. Colloid Interf. Sci.* **1973**, 43, 217.
- [4.24] Zych, E.; Brecher, C.; Glodo, J. *J. Phys.: Condens. Mat.* **2000**, 12, 1947.
- [4.25] Lu, C.-H.; Hong, H.; Jagannathan, R. *J. Mater. Chem.* **2002**, 12, 2525.
- [4.26] Li, G.; Cao, Q.; Li, Z.; Huang, Y. *J. Rare Earth* **2008**, 26, 792.
- [4.27] Hirayama, M.; Sonoyama, N.; Yamada, A.; Kanno, R. *J. Solid State Chem.* **2009**, 182, 730.
- [4.28] He, X.; Li, W.; Zhou, Q. *Mater. Sci. Eng. B* **2006**, 134, 59.
- [4.29] Zhu, Q.; Li, J.-G.; Li, X.; Sun, X.; Sakka, Y. *Sci. Technol. Adv. Mater.* **2011**, 12, 1.
- [4.30] Chung, M. S.; Jeon, M. J.; Lee, S. C.; Kang, B. K.; Kim, H. J.; Yang, S. S.; Kim, J. S.; Ahn, Y. J. *Displays* **2007**, 28, 68.
- [4.31] Jung, K. Y.; Lee, C. H.; Kang, Y. C. *Mater. Lett.* **2005**, 59, 2451.
- [4.32] Kasuya, R.; Isobe, T.; Kuma, H. *J. Alloys Compd.* **2006**, 408, 820.
- [4.33] Nyman, M.; Shea-Rohwer, L. E.; Martin, J. E.; Provencio, P. *Chem. Mater.* **2009**, 21, 1536.
- [4.34] Rohwer, L. S.; Martin, J. E. *J. Lumin.* **2005**, 115, 77.
- [4.35] Revaux, A.; Dantelle, G.; George, N.; Seshadri, R.; Gacoina, T.; Boilota, J.-P. *Nanoscale* **2011**, 3, 2015.
- [4.36] Kamiyama, Y.; Hiroshima, T.; Isobe, T.; Koizuka, T.; Takashima, S. *J. Electrochem. Soc.* **2010**, 157, J149.

- [4.37] Li, Y. X.; Min, Y. L.; Zhou, X. Z.; You, X. Z. *Chin. J. Inorg. Chem.* **2003**, 19, 1169.
- [4.38] Chen, L.; Li, X.; Feng, W.; Tao, C.; Li, W. *Asian J. Chem.* **2011**, 23, 4694.
- [4.39] Palilla, F. C.; Levine, A. K.; Tomkus, M. R. *J. Electrochem. Soc.* **1968**, 115, 642.
- [4.40] Rodrigues, L. C. V.; Stefani, R.; Brito, H. F.; Felinto, M. C. F. C.; Hölsä, J.; Lastusaari, M.; Laamanen, T.; Malkamäki, M. *J. Solid State Chem.* **2010**, 183, 2365.

초 록

형광체는 발광다이오드, 플라즈마 디스플레이 패널, 음극선관 등에 다양하게 응용되는 광학 물질로써, 특히 최근의 조명용 발광다이오드 등에서의 응용으로 그 관심이 매우 높아지고 있다. 형광체에 대한 연구는 크게 새로운 조성의 형광체 개발과 나노미터 크기의 형광체 합성, 형광체 발광 특성의 조절, 발광 메커니즘 연구 등에 그 초점을 맞추어서 진행되고 있다. 청색 LED 와 노랑색 형광체 ($\text{Y}_3\text{Al}_5\text{O}_{12}:\text{Ce}^{3+}$) 를 이용하여 백색광을 만드는 상용화된 백색 LED 시스템에서 백색 LED 의 최종 광전변환 효율은 마이크로미터 크기의 $\text{Y}_3\text{Al}_5\text{O}_{12}:\text{Ce}^{3+}$ 형광체에서 일어나는 후방산란에 의한 손실 때문에 30%에 불과하다. 후방산란에 의한 손실은 입자 직경의 6 제곱에 비례하므로 형광체 입자의 크기를 나노미터 크기로 합성하는 것은 후방산란에 의한 손실을 최소화하여 백색 LED 의 광전변환 효율을 증가시키는데 중요한 역할을 한다. 또한 단분산된 구형의 형광체는 이러한 형광체를 적층하였을 때, 광학적인 구조를 최적화하여 적층된 형광체의 효율을 높일 수 있기 때문에 많은 관심을 받고 있다. 그러므로 단분산된 구형의 형광체를 나노미터크기로 합성하는 연구가 백색 LED 분야에서 주된 화두로 떠오르고 있다.

본 연구에서는 강제가수분해법을 이용하여 다양한 크기를 갖는 단분산된 구형의 Al_2O_3 나노입자를 합성하고 그 합성조건을 이용하여 3 성분계 알루미늄이트 형광체, 그 중에서도 $\text{Y}_3\text{Al}_5\text{O}_{12}:\text{Ce}^{3+}$ 와 $\text{BaAl}_2\text{O}_4:\text{Eu}^{2+}$ 형광체를 합성하고 그 특성을 평가하였다.

먼저 강제가수분해법의 변수를 조절하여 다양한 크기를 갖는 단분산된 구형의 수산화 알루미늄 전구체를 합성하였다. 수산화 알루미늄 전구체를 합성하는데 원료 물질로 사용한 질산 알루미늄과 황산 알루미늄의 비율을 조절하여 수산화 알루미늄 전구체의 크기를 조절하였다. 비정질 수산화 알루미늄 전구체는 900 °C 와 1100 °C 에서 각각 순수한 γ -Al₂O₃ 와 α -Al₂O₃ 로 상합성되었으며 열처리 후에도 나노 입자의 단분산성 및 구형의 모양은 유지되었다. 이 때, 합성된 γ -Al₂O₃ 와 α -Al₂O₃ 는 모두 다공성구조를 가지며 비표면적은 각각 102 m²/g 과 76 m²/g 임을 Brunauer-Emmett-Teller (BET)법을 이용하여 확인하였다. 결과적으로 수산화 알루미늄 전구체의 크기에 따라 125 nm, 195 nm, 320 nm, 430 nm 의 크기를 갖는 단분산된 구형의 Al₂O₃ 다공성 나노 입자를 합성할 수 있었다.

다음으로 템플릿을 사용하지 않고 강제가수분해법을 이용하여 단분산된 구형의 Y₃Al₅O₁₂:Ce³⁺ 나노 형광체를 합성하였다. 강제가수분해법을 이용하여 합성된 단분산된 구형의 비정질 전구체는 1075 °C 열처리를 통해 순수한 Y₃Al₅O₁₂ 로 상합성되었으며 합성된 Y₃Al₅O₁₂:Ce³⁺ 나노 형광체의 단분산성과 모양은 잘 유지되었다. 비교적 높은 상합성 온도에도 불구하고 나노 형광체의 단분산성과 모양이 유지되는 이유는 Y : Al = 3 : 5 의 비를 초과하여 존재하는 과량의 Al³⁺ 이온이 열처리 과정 중에 표면에 비정질 산화 알루미늄 층을 형성하여 나노 입자간에 발생할 수 있는 Necking 현상을 막아줬기 때문으로 생각된다. 결과적으로 평균 입자 크기가 33 nm 인 단분산된 구형의 Core-shell 구조를 갖는

$\text{Y}_3\text{Al}_5\text{O}_{12}:\text{Ce}^{3+}$ 나노 형광체를 합성할 수 있었으며 합성된 형광체 나노 입자의 형광 특성은 33 %의 발광 효율과 나노 입자임에도 상대적으로 우수한 광안정성을 보이는 것으로 분석되었다.

마지막으로 단분산된 구형의 $\gamma\text{-Al}_2\text{O}_3$ 템플릿을 이용하여 단분산된 구형의 $\text{BaAl}_2\text{O}_4:\text{Eu}^{2+}$ 형광체를 합성하였다. 강제가수분해법의 반응시간에 따라 $\gamma\text{-Al}_2\text{O}_3$ 템플릿에 코팅되는 Ba^{2+} 이온의 양이 증가되었으며 3 시간 반응시킨 시료의 경우 800 °C 를 통해 순수한 BaAl_2O_4 을 합성할 수 있었다. 또한 $\gamma\text{-Al}_2\text{O}_3$ 템플릿의 크기를 조절하여 $\text{BaAl}_2\text{O}_4:\text{Eu}^{2+}$ 형광체의 크기를 조절하였으며, 합성된 나노 형광체의 여기 및 방출 파장은 각각 350 nm 와 499 nm 로 분석되었다.

이 연구에서는 다양한 크기를 갖는 단분산된 구형의 Al_2O_3 및 3 성분계 알루미늄네이트 형광체의 나노 합성 및 발광 특성을 분석하는 것에 주안점을 두었으며 이를 통해서 형광 특성이 뛰어난 나노미터 크기의 알루미늄네이트 계열 형광체 합성에 있어서 당면한 문제점을 해결하는 가능성을 제시해 줄 수 있을 것이다.

주요어: 단분산, 크기 조절, 나노, 알루미늄네이트, 강제가수분해법, 형광체

학 번: 2006-23046